12-2013

High Energy Synchrotron X-ray Study of Fatigue Damage in Amorphous and Polycrystalline Engineering Alloys

Chih-Pin Chuang
University of Tennessee - Knoxville, cchuang@utk.edu

To the Graduate Council:

I am submitting herewith a dissertation written by Chih-Pin Chuang entitled "High Energy Synchrotron X-ray Study of Fatigue Damage in Amorphous and Polycrystalline Engineering Alloys." I have examined the final electronic copy of this dissertation for form and content and recommend that it be accepted in partial fulfillment of the requirements for the degree of Doctor of Philosophy, with a major in Materials Science and Engineering.

Peter K. Liaw, Major Professor

We have read this dissertation and recommend its acceptance:

John D. Landes, Yanfei Gao, Wojciech Dmowski

Accepted for the Council:
Carolyn R. Hodges

Vice Provost and Dean of the Graduate School

(Original signatures are on file with official student records.)

High Energy Synchrotron X-ray Study of Fatigue Damage in Amorphous and Polycrystalline Engineering Alloys

A Dissertation Presented for the
Doctor of Philosophy
Degree
The University of Tennessee, Knoxville

Chih-Pin Chuang

December 2013

DEDICATION

This dissertation is dedicated to my wife, Paihua Tsao, my two lovely daughter, Allison and Charlotte, my parents, Yuan-Yung Chuang and Hseu-hua Hsu, my father in law, Hui Tsao, my mother in law, Mrs. Long-ying Liang and the rest of my family, for their love, encouragement, and support.

ACKNOWLEDGEMENTS

I would like to thank Prof. Peter K. Liaw for his advices, assistance, and guidance during my graduate studies. He provides a constrain-free environment for me to fully develop my potential. The way he conducts the research have taught me a great deal about how to be successful in academia. Moreover, I would like extend thanks to my committee members Profs. Yanfei Gao, Prof. John D. Landes, and Prof. Wojciech Dwmoski, at the University of Tennessee for their time and insightful advices.

This research would not have been possible without the help of many people from the University of Tennessee at Knoxville, TN, Advanced Photon Source (APS), Argonne National Laboratory at Lemont, IL, GE global research center at Niskayuna, NY, and Beihang University in China. I would like to thank Prof. Wojciech Dmowski and Prof. Takeshi Egami for bringing me into the world of amorphous alloys and pair-distribution function analyses. The works with Prof. Dmowski constitute the major part of present research, his help and suggestions are something I can never forget. I want to thank Douglas E Fielden, Larry Allen Smith, and Danny F Hackworth in the machine shop for their timely work and suggestions for machining my specimens. The lunch meeting with them were among the best therapeutic sessions I had to help me got through the difficulties. I am also thankful for the services provided by William Frank Holiway, Randall D Stooksbury, Carla Lawrence, and Susan D Seymour of the University of Tennessee. Their help make my life easier at UT. The suggestions and help from Dr. Yang Ren of 11-ID and Dr. Jon Almer of 1-ID in APS are greatly appreciated. My synchrotron x-ray experiments wouldn't had been so successful without their help and support. I would also like to thank Dr. R Li, Dr. Lu Huang and Dr. Tao Zhang from Baihang University who kindly provide the BMG samples for part of my research. In addition, I am also indebted to Dr. Yan Gao, Dr. Liang Jiang of GE research center, the research project from them opened my eye with regard to how the cutting edge research can connect to the real world applications. Here, I'd like to convey my special thanks to Dr. Yan Gao for his valuable guidance and mentoring. The way he does the research and his philosophy toward the balance of life and work have a significant impact on me. I consider knowing him the best gift I had received during my graduate

studies. I appreciate Prof. Tao Yan of Ohio University for his help on the statistical analysis, and Mr. Chou Pu, who works for Prof. Yanfei Gao, for his help on computer simulation.

Many thanks also goes to all of my team members, the past and the current, at the University of Tennessee. Those include Dr. Cang Fan and Dr. Dongchun Qia, who taught me how to use arc-melter, Dr. Gongyao Wang, who helped me to conduct mechanical tests, Dr. Brandice Green, who showed me the electrochemical experiments, Dr. Li Li, Dr. E-wen Huang, Dr. Feng Jiang, Dr. Zhengke Teng, Dr. Shenyan Huang, Dr. Matthew Freels, Mr. Wei Wu, Mr. Zhinan An, Mr. Wei Guo, Mr. Xie Xie, Mr. Qingming Feng, Mr. Haolin Jia, Mr. Zhi Tang, Mr. Bilin Chen, Mr. Zhiqian Sun, Mr. Louis J. Santodonato, Mr. Micheal A Hemphill, and Ms. Haoyan Diao, who share the same memory with me working in Prof. Liaw's research group.

I would like to acknowledge the financial support from the National Science Foundation (NSF), the International Materials Institutes (IMI) Program, under DMR-0231320. The Use of the Advanced Photon Source, an Office of Science User Facility operated for the U.S. Department of Energy (DOE) Office of Science by Argonne National Laboratory, was supported by the U.S. DOE under Contract No. DE-AC02-06CH11357.

Last but not the least, I want to thank my wife, Phoebe Tsao, for her endless patient, and my whole family who support me in many different ways before and during my graduate studies.

ABSTRACT

The dissertation summarizes a series of studies on the fatigue damage of both amorphous and crystalline engineering alloys. The attention focuses on the utilization of synchrotron x-ray scattering related techniques for advanced material characterizations. In the first part of the research, critical issues regarding the mechanical response and structural evolution of Bulk-Metallic Glasses (BMGs) in the elastic region are addressed. The effects of cyclic-loading on the microstructures of an amorphous alloy are investigated, aiming to provide better mechanistic understandings of fatigue damage in BMGs. The second part of the research focuses on the characterization method based on two-dimensional X-ray diffraction to better predict the fatigue life of Ni-based superalloys.

Bulk-amorphous metallic alloys are a new class of materials that exhibit superior material properties. X-ray pair-distribution function (PDF) analysis is used to study the deformation of BMGs on the microscopic scale in the elastic region. The results show that the deformation behavior of BMGs is fundamentally visco-elastic.

The effect of "fatigue" on the fatigue behavior and atomic structure of Zr-based BMGs has been investigated. Fatigue experiments on the failed-by-fatigue samples indicate that the remnants generally have similar or longer fatigue life than the as-cast samples. Meanwhile, the pair-distribution-function (PDF) analysis of the as-cast and post-fatigue samples showed very small changes of local atomic structures. These observations suggest that the fatigue life of the 6-mm in-diameter Zr-based BMG is dominated by the number of pre-existing crack-initiation sites in the sample

For the study of fatigue damage in Ni-based superalloys, the correlation between the microstructure, from the x-ray diffraction point of view, and fatigue life is established. The development of residual strain/stress, can be measured accurately by in-situ two-dimensional (2D) x-ray diffraction. The size of the compressive strain zone ahead of a notch tip increases with fatigue life and is most sensitive during the initial cycles and final stage. However, the estimation of fatigue damage is qualitative, not quantitative. Finally, the strain variation possibly caused by the intergranuler stresses is large at the beginning of the fatigue life, but decrease with increasing fatigue cycles, which indicates more and more grains were plastically deformed.

TABLE OF CONTENTS

LIST OF TABLES

LIST OF FIGURES

1 CHAPTER I

INTRODUCTION

Fatigue, defined as “progressive and localized structural damage that occur when a material is subjected to cyclic loading”, has long been recognized as one of the major causes for the catastrophic damage in components or even entire systems. It is estimated that 90% of all metallic failures are attributed to the metal fatigue. The first public record of fatigue failure can be traced back as early as 150 years ago. In 1843, Rankine wrote “... The unexpected fracture of originally good railway axles, after running for several years, without any appearance of unsoundness, must be caused by a gradual deterioration in the course of working….” Until today, despite the intensive research and studies for over a century, this problem still torment today’s scientists and engineers.

The progression of fatigue damage can be broadly classified into the following stages:[1] (a) sub-structural changes, which cause the nucleation of permanent damage, (b) the formation of microscopic cracks, (c) the growth and coalescence of microscopic flaws (short cracks) to form ‘dominant’ cracks, which may eventually lead to catastrophic failure, (d) stable propagation of the dominant macro-cracks, and (e) structural instability or complete fracture. Since Forsyth[2] first showed that the fatigue damage start with the slip-induced surface roughening during cyclic loading, Wood[3] proposed mechanisms to describe the origin of fatigue cracks. He believed that the repeated cyclic straining of the material leaded to different amounts of net slip on different glide planes, and the irreversibility of shear displacements resulted in the ‘roughening’ of the material surface.

It is well known now that fatigue cracks initiate from the bands of localized deformation known as slip bands.

There are numerous studies of the initiation and propagation of fatigue cracks in the past century. Well-developed fracture mechanics have been shown to be successful to predict the propagation of fatigue cracks. Recent studies had been focused on the initiation stage of fatigue process because of the complicated nature of the crack formation mechanisms. It is found that the formation of a crack is very sensitive to the micro-structure where it is nucleated. The optical microscopy (OM), scanning-electron microscopy (SEM), and transmission electron microscopy (TEM) techniques had been used to explore the microstructural evolution along the slip bands. More recently, techniques were developed, especially scanning tunneling microscopy (STM) and atomic force microscopy (AFM), to measure the surface displacement due to fatigue, on the order of 20 nm.[4-8] However, most of the techniques are destructive and require special specimen preparation procedure, and the information obtained are localized. In the current research, we aimed to develop a non-destructive characterization technique utilizing synchrotron X-ray to study the fatigue damage of both amorphous and crystalline alloys.

2 CHAPTER II

LITERATURE REVIEW

2.1 Bulk metallic glasses

Bulk-metallic glasses (BMGs) are a revolutionary new class of engineering materials with potential applications ranging from automotive and aerospace structures to biomedical devices and sporting goods. Metallic glasses are materials with constituent atoms being packed together in a somewhat random fashion, similar to that of a liquid. Owing to the lack of long rang order crystal structures, BMGs exhibit many impressive properties different from their crystalline counterparts, including extremely high tensile yield strengths (~ 1 - 2 GPa typically, up to 5 GPa for newly developed Co-based BMGs [9]) which is twice those of stainless steels and titanium alloys, and large elastic deflections, ~ 2% elastic strain [10], which is much higher than those of crystalline metallic alloys (less than 1%). Combined with low density (3 ~ 6 g/cm3) relative to traditional metallic alloys, they have high strength-to-weight ratios. These unique properties make BMGs having great potentials to replace some conventional crystalline materials used in the energy industry.

2.1.1 Deformation behavior of BMGs

Since BMGs are amorphous and lack of crystal defects, such as dislocations and grain boundaries, which are critical for the deformation of crystalline materials. The fatigue behavior of BMGs must be very different from traditional crystalline alloys. In order to study the deformation of BMGs under cyclic loading conditions, it is very important to first

understand how BMGs deformed plastically under monotonic stresses and the corresponding theory for the deformation.

BMG can deform either inhomogeneous or homogeneous depending on the deformation conditions such as temperature and strain rate. The homogeneous deformation usually occurs at temperatures close to glass transition temperature (T_g), and the deformation of BMG can even exhibit super-plasticity in the super-cooled liquid region ($T_g < T < T_x$). The "homogeneous deformation" means the whole part of the sample participate in the deformation. The shape and size of the deforming sample change simultaneously, and the deformation is uniform at macroscopic scale. No shear localization can be observed. Since BMGs are meta-stable materials, most of the applications are in room temperature or lower. Therefore, current research only focuses on the deformation behavior at room temperature. A more detail discussion of the homogeneous deformation of BMGs at higher temperature can be found in Schuh et al. [11].

On the other hand, when the deformation of BMGs at temperatures way below its glass transition temperature, metallic glasses deformed in highly inhomogeneous manners [12, 13]. The deformation highly localized into shear bands, which initiate and propagate rapidly across the sample. Owing to its lack of the work-hardening ability, once the shear band initiates, it will move across the whole sample and result in the macroscopic fracture. Although large amount of plastic deformation occurred in shear bands, a band is 10 ~ 20 nm in width, the overall plastic deformation of the sample is generally very low (0 ~ 2 %). The fracture surface shows a typical vein pattern (Figure 2-1 Fracture surface of Cu-based BMG fractured in compression. The vein pattern results from the lowered viscosity in the

band.). The vein pattern on the fracture surface of a failed compression sample is the same as that produced by pulling apart two glass slides with a thin layer of Vaseline between them. The same feature can also be found on the fracture surface of the specimens in the tension test [10, 14]. The viscosity of the material in the shear bands has dropped several orders of magnitudes. Few models had been proposed to explain the characteristic deformation behaviors, such as the formation of free volume [15, 16], the local adiabatic heating [17], shear-transformation-zone (STZ) theory [18] … etc. However, the well accepted mechanism for this viscosity drop is still not clear.

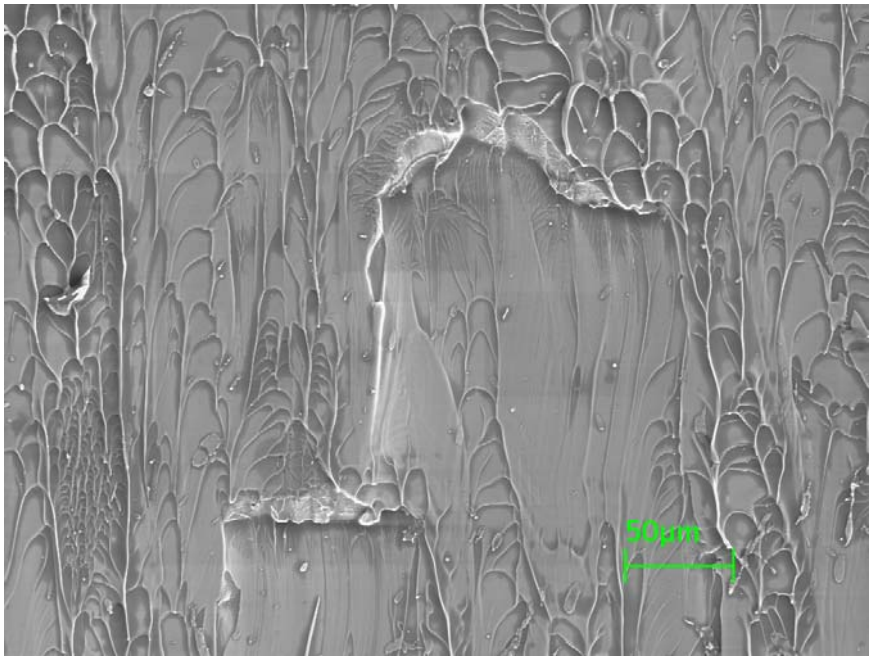

Figure 2-1 Fracture surface of Cu-based BMG fractured in compression. The vein pattern results from the lowered viscosity in the band.

2.1.2 Deformation mechanism of BMGs

Despite the great amount of efforts had been made to understand the mechanisms governing the deformation behavior of amorphous alloys, the theory in explaining the plastic deformation of metallic materials in a glassy state, like the dislocation theory in their crystalline counterparts, remains absence. The development of such theory is quite difficult because the atomic arrangement in amorphous alloys remains mysterious at present. Without the precise description of the atomic arrangement, the establishment of theory for deformation of amorphous alloys is far from certain. The most widely applied model used to explain the deformation of metallic glasses is the Free-Volume Model proposed by pioneers, M. Turnbull, M. Cohen, and F. Spaepen et. al. [16, 18-21], in early 70s. The idea of free-volume goes back long time, and has been known that volume is a very good index for measurement of the viscosity of a liquid. The theory proposed that an atom is trapped in the "cage" of neighboring atoms, with a lot of small space (free volume) υ, in-between the atoms. The probability distribution of such a free volume can be described by

$$p(\upsilon) = \frac{\gamma}{\upsilon_f} exp(-\frac{\gamma.\upsilon}{\upsilon_f}) \qquad (2\text{-}1)$$

where γ is a geometrical constant, and υ_f is the total free-volume, which depends linearly on the temperature above the glass-transition temperature T_g [18]. Since an atom is confined in the "cage", it cannot jump out of its original position unless the surrounding free volume, υ^*, is large enough for it to make a successful jump. The magnitude of υ^* is about 80% of the atomic volume. Thus, the deformations of amorphous material can be

described by the redistribution of the free volumes. However, there are different thoughts [22] arguing that whether it can be used on the atomistic basis.

2.1.3 Deformation study of BMGs by high energy synchrotron X-ray

It is clear that all matters are made of atoms, and the properties of matter depend on which atoms are used and how they are bonded together. The structure of materials can be categorized as (1) atomic structure, which includes features that cannot be seen, such as the types of bonding between the atoms, and the way the atoms are arranged, (2) microstructure, which includes features that can be seen using a microscope, but seldom with the naked eye, and (3) macrostructure, which includes features that can be seen with the naked eye. The atomic structure primarily affects the physical, chemical, thermal, electrical, magnetic, and optical properties. The microstructure and macrostructure can also affect these properties but they generally have a larger effect on mechanical properties. Since the properties of a material are closely related to its structure, structure characterization is the fundamental steps for the study of the materials.

The purpose of structural analysis is to find the correlation between the structure and the properties of a material, so that we can modify the properties by altering the structure. Since BMG have no structure periodicity, the first problem would be “How to describe the structure of a disordered system in a scientific and systematic way?” In material science, one way of describing the structure of a material is to describe the relative position of each atom with respect to each other in that material. In crystalline materials, since the structure is very well defined, it can be done conveniently by describing the

arrangement within the solid of a small representative group of atoms, called the "unit cell". By multiplying identical unit cells in three directions, the location of all the particles in the crystal is determined. The translational order in a crystal leads to easy description of the structure, only a few positions are needed to specify the entire crystal structure. In liquids and glasses, atomic positions are dynamic. Particularly in liquids, the local environment of an atom changes rapidly as it diffuses. In glasses, different atoms of the same type are in different environments, but each atom's environment is more or less static. In either liquid or glass, the structure is inherently statistical. Because of the lack of long range periodicity in glass, describing the structure by specifying all the atomic positions becomes not only impractical, but also useless. Even if one was able to find out the atomic coordinates of all the, we say, 6×10^{23} atoms in a specimen, we would not be able to comprehend and use such information. Therefore, a better way is required to describe the structure of an amorphous material.

Clearly, the properties of a material are not determined by the absolute position of each atom, but by the relative positions of the atoms which are close enough to have some interaction. In other words, local atomic environment, the relative positions of the neighboring atoms, is what one has to know to understand the properties of the material. Therefore, a function is required to express the distance-atom density relationship. Here, a method, atomic pair-distribution function (PDF) analysis emerges as the solution for the structure characterization of amorphous alloys. PDF describes the distribution of distances between pairs of atoms contained within a given volume as illustrated in Figure 2-2. While traditional crystallographic analysis takes into account only the Bragg peaks, which are tall

and clearly visible in the diffraction pattern, the PDF method utilizes information buried in-between the Bragg peaks in the form of diffuse scattering, component. It allow both the Bragg and diffuse scattering to be analyzed together without bias, revealing the short and intermediate range order of the material regardless of the degree of disorder. Because all of the scattering signals are used, PDF analysis is also called “total scattering analysis”. PDF had been shown to be one of the very valuable techniques to study the amorphous or nano-crystalline materials[23, 24]. The theory and mathematical equations underlying PDF analysis as well as the experimental method will be described in Section 3.4.

Many techniques have been used to study the deformation mechanisms of BMGs. Ex-situ uniaxial tests (under tension or compression) are usually performed to study the mechanical behaviors of BMGs under different loading modes. Rich information, such as the elastic limit, yield stress, plastic strain of BMG…etc., can be obtained from these tests. In the tests, many characterization techniques have been utilized to investigate the deformation mechanisms of BMGs. For example, the serrated flow was characterized from stress-strain curves and high-speed camera. The spatiotemporally of shear banding and the fracture mode was studied by scanning electron microscopy (SEM). The structure of shear bands was studied by transmission electron microscopy (TEM). In crystalline materials, the crystalline structure is usually determined by X-ray diffraction. The evolution of lattice strains during deformation can be determined directly by calculating the changes of lattice spacing using diffraction experiments. The source of the diffracting wave can be either x-ray, electron or neutron. In amorphous alloys, which do not possess long range periodicity in the atomic structure, it is not so obvious if the same can be done or not. Poulsen et al.

[25] had been shown recently that the local strain in metallic glasses can be measured by high energy X-ray diffraction. By tracing the shifts in the first peak of the structure function, S(Q), or the oscillations in the atomic pair-density function (PDF), g(r), the strain can be estimated. Nevertheless, studying the response of atoms in metallic glasses under an applied external stress is very important for understanding the deformation mechanisms of BMGs.

Combining the high brilliance and high energy resolution, the in-situ high energy X-ray diffraction experiments of BMG used mainly synchrotron radiation as x-ray light source. The x-rays used for these experiments were monochromatic hard x-rays with energies between 80 keV~ 100 keV. The direct information collected from diffraction of metallic glasses is the scattering intensity, I(Q), as a function of the scattering vector, Q, which is defined as

$$Q = \frac{4\pi \sin\theta}{\lambda} \qquad (2\text{-}2)$$

where θ is half of the scattering angle, and λ is the wave length of the X-ray. The structure factor can be written as

$$S(Q) = \frac{I(Q)}{N\left\langle f(Q)\right\rangle^2} \qquad (2\text{-}3)$$

where N is the number of atoms, f(Q) is the atomic-scattering factor for x-rays, and the angular brackets indicate averaging over the composition of the materials [26]. The real space structural information is the PDF, g(r), in which r is the distance from an average atom located at the origin. It can be obtained through Fourier transformation of S(Q). The

radial distribution function (RDF), which is defined as $4\pi r^2 g(r)$, is also an important function related to PDF. By integrating the RDF spectrum over a suitably chosen range of r, the coordination number of a particular atomic shell can be obtained easily.

When an external macroscopic stress is applied to a metallic glass, the atoms will rearrange their position, and these changes can be observed in S(Q) and g(r) accordingly. For a uniaxial loading (compression or tension), the changes in the real space is easy to expect. The compressive stress will tend to move atoms closer in the loading direction, and, thus, a peak in g(r) for that direction will move to smaller values of r for a tensile stress, the opposite should happen. In the reciprocal space, Q is expected to shift toward higher values in the case of the compressive stress and lower values when the sample is tensioned. By analogy to the definition of engineering strain, the strain of BMG for an applied stress, σ, can be written as

$$\varepsilon_i(\varphi_i,\sigma) = \frac{Q(\varphi_i,0) - Q(\varphi_i,\sigma)}{Q(\varphi_i,\sigma)} \qquad (2\text{-}4)$$

which is polar-angle-dependent. In the transverse direction, a strain of the opposite sign can be expected due to the Poisson's effect. A typical diffraction image of a metallic-glass sample is shown in Figure 2-3. The diffraction from amorphous structure is board and has the first and strongest peak around Q = 2.8 ~ 3.2 $Å^{-1}$. There will be no sharp and clear ring from crystalline phases. The I(Q) can be integrated upon the polar coordinates (σ, φ). The integration can be done by dividing the entire circle into sections based on the divided angle. For example, the entire circle can be divided into 36 sections of 10º each. The integration of 2D image was performed by FIT2D software [27]. Since only elastic

scattering is interested, the integration of the intensity curves need to be corrected for the background, polarization, and inelastic Compton scattering. The structure factor, S(Q), can be calculated based on the equation with the help of the PDFgetX2 software package. Once the load is applied, the round concentric halos from Figure 2-3 become elliptical, and the asymmetry increases as the load increases. The angular variation of the strain can be fitted with the following equation

$$\varepsilon(\varphi,\theta) = \varepsilon_{11}\sin^2\varphi + \varepsilon_{12}\sin\varphi\sin\varphi + \varepsilon_{22}\cos^2\varphi \qquad (2\text{-}5)$$

The strain tensor including the axial, ε11, tangential, ε22, and in-plane shear component, ε12, can then be determined. In Figure 2-3, φ = 90º corresponds to the axial stress, and φ = 0º corresponds to the tangential stress. Components not in the plane perpendicular to the incoming beam can be determined by rotating the specimen around an axis perpendicular to the incoming beam. The similar analysis works in the real space. However, Dmowski and Egami [ref] pointed out that due to the presence of the structural anisotropy, PDF should be expanded into a spherical harmonics, otherwise systematic errors may occur especially in the first neighborhood.

Stoica et al. [28] studied the strain distribution of a $Zr_{64.13}Cu_{15.75}Ni_{10.12}Al_{10}$ BMG by in-situ tensile experiment using high energy synchrotron X-ray. They found that when a load was applied to the sample, the diffraction rings became elliptical. To describe such changes more quantitatively, the authors constructed a set of symmetrized intensity distributions, as described previously and traced the change in the first peak position as a function of the azimuth angle, φ, and tensile stress, σ. The experimental scatter of the measured strain values at each different stress level is shown in Figure 2-4 and Figure

2-5[28]. From Figure 2-4, it is proved that the asymmetry of the first diffuse maximum increases with increasing the load. The decrease in the peak position with increasing the tensile stress reflects the fact that atoms move apart along the tensile direction. An opposite behavior is observed in the transverse direction. Figure 2-5 shows the angular variation of the strain at a given stress, σ, as calculated from the relative change in the position of the first peak using Equation 2-5. The fit of the experimental data to Equation 2-5 gives the axial and tangential components of the strain tensor, ε11 and ε22, respectively. The stress-strain curves for different strain-tensor components are shown in Figure 2-6. The curves all present a linear behavior within the experimental error, which indicates the elastic deformation for the investigated specimens. The maximum axial strain (ε11) is 1.50 ± 0.01%. The elastic modulus determined in the tensile mode is E11 = 94 ± 1 GPa, and the experimentally-determined Poisson's ratio, $\nu = - \varepsilon 22 / \varepsilon 11$, is 0.325 ± 0.01.

Mattern et. al [29] studied the structure behavior of Cu_xZr_{100-x} metallic glass by PDF analysis. They determined the partial pair correlation functions of different Cu_xZr_{100-x} alloys by assuming the atom to stay unchanged and only the weight factors were changed. The results showed that the structure of Cu_xZr_{100-x} can be well described by a solid solution-like replacement of Cu and Zr atoms in the whole composition range. No indications are observed that would support the existence of special structure or the presence of phase separation in the glassy state of rapidly quenched Cu_xZr_{100-x} alloys.

Wang et. al. [30] investigated the tensile behavior of Zr-based and La-based BMG by in-situ high energy x-ray diffraction. They claimed that the tensile elastic modulus and Poisson's ratio can be determined accurately by x-ray diffraction. No excess free volume

appears in the fractured region. In La-based BMG, the atomic-level strains as a function of atom-to-atom distances along tensile direction is larger than that in Zr-based BMG, but no explanation was offered.

Nevertheless, high energy X-ray diffraction had been shown to be an effective technique to study the structure of BMG. The PDF analysis can reveal the response of atomic structure under an applied external stress. The Young's modulus, and Poisson's ratio from X-ray method are similar to those by other techniques such as ultrasonic measurement.

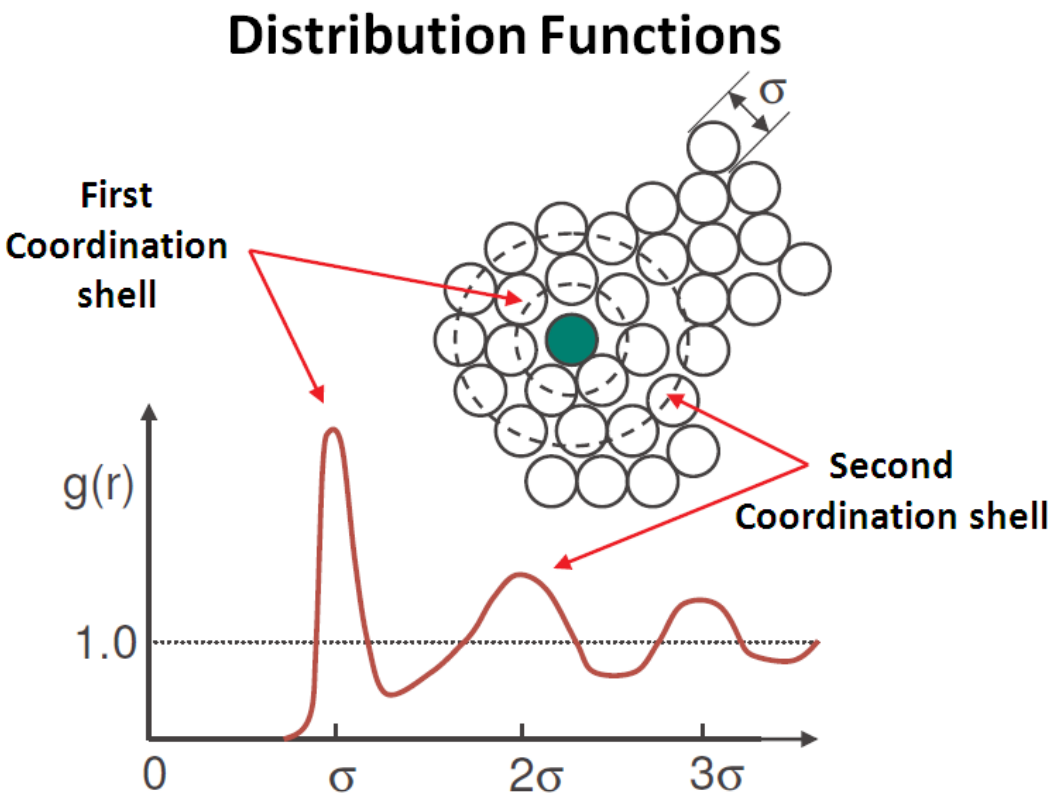

Figure 2-2 Distribution functions describing the atom-atom distance.

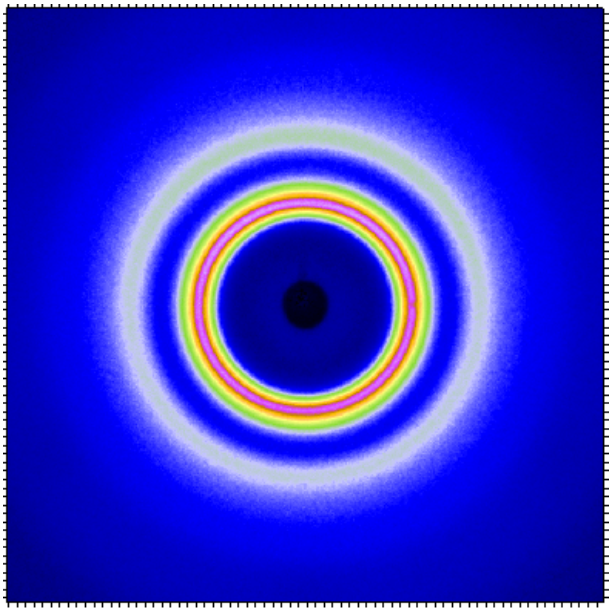

Figure 2-3 High-energy synchrotron X-ray scattering image recorded by a 2D detector.

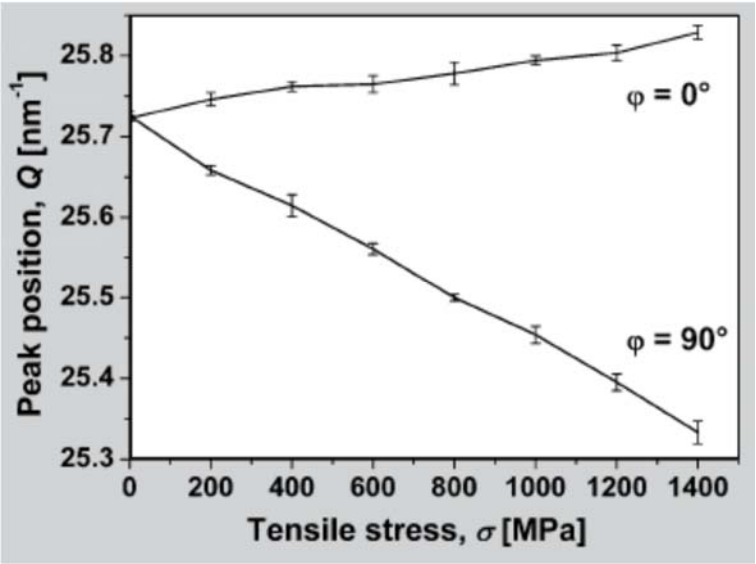

Figure 2-4 Shifting of first board peak as a function of applied tensile load, measured in tensile, and transversal direction for $Zr_{64.13}Cu_{15.75}Ni_{10.12}Al_{10}$ BMG [28].

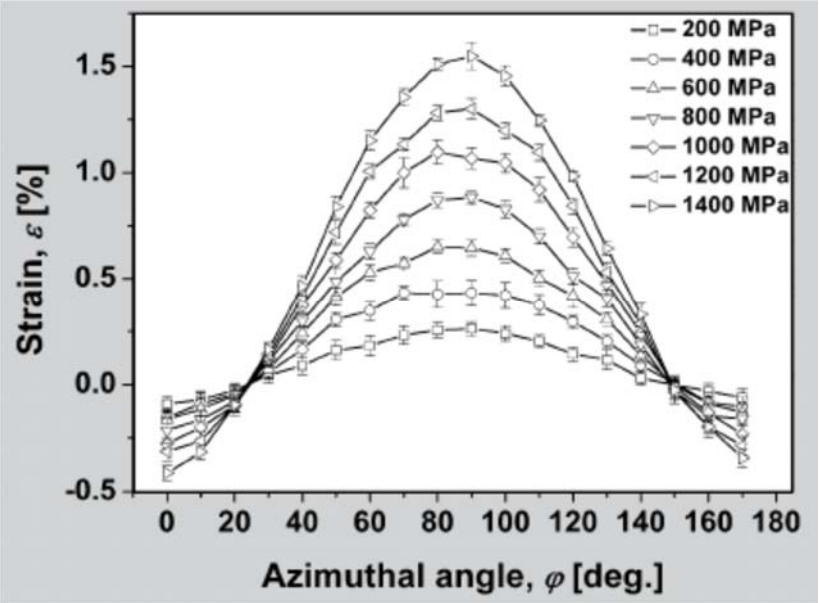

Figure 2-5 Angular dependence of the strain determined at various stages of tensile deformation of $Zr_{64.13}Cu_{15.75}Ni_{10.12}Al_{10}$ BMG, as calculated from the relative change in the position of the first peak using equation 1.5 [28].

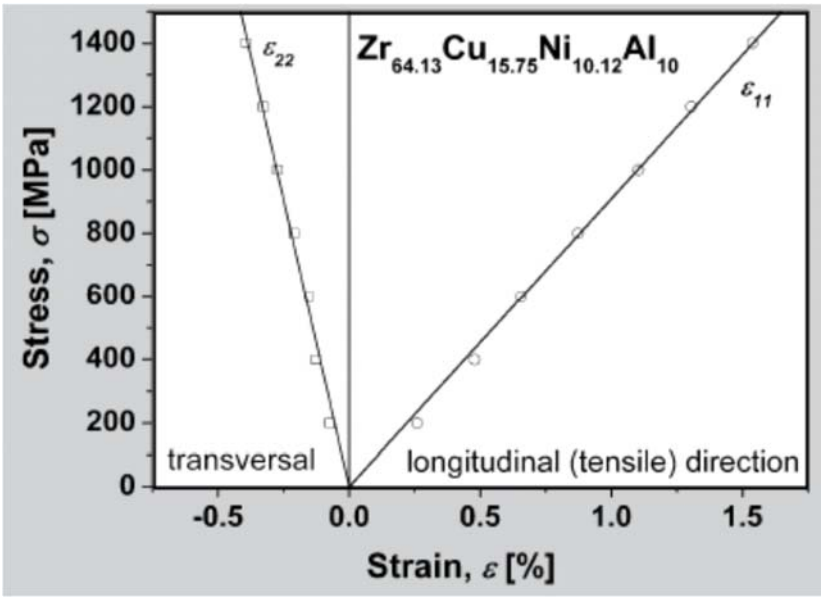

Figure 2-6 Stress-strain curves for different strain tensor components measured for $Zr_{64.13}Cu_{15.75}Ni_{10.12}Al_{10}$ BMG. The straight lines represent a linear fitting of the experimental data, starting from the origin of the coordinate system [28].

2.1.4 Fatigue behavior of BMGs

BMGs will undergo mechanical fatigue even when the applied cyclic stress is far below their yielding stresses, σ_{ys}. The stress-strain curve indicates that the deformation of the specimen at such stress levels should be elastic, i.e., the material returns to its original state after the applied load is removed. Several researchers [31-39] have shown that the fatigue behavior of the Zr-based BMGs shares many similarities with the crystalline materials. For example, the stress versus the number of fatigue-life cycles (S-N) curve of the BMG resembles its crystalline counterparts, where the fatigue life is inversely proportional to the applied stress and possesses a threshold, defined as the fatigue-endurance limit (typically refers to the stress or stress range at 10^7 cycles). In the present article, we use the stress range, $\Delta\sigma = |\sigma_{max.}-\sigma_{min.}|$, to calculate fatigue limit for our own results and other researchers' data, where $\sigma_{min.}$ and $\sigma_{max.}$ are applied minimum and maximum stresses, respectively. When the cyclic stress imposed on the sample is lower than this limit, the sample will not fail. A more rigorous description is that the failure of the sample will not occur within the testing time frame, 10^7 cycles in general.

The crack-propagation behavior in the BMG is similar to ductile crystalline alloys [32, 40]. The crack-growth rate depends on the applied stress range, and striations can be observed on the fracture surface [31]. The fatigue-failure process of the BMG can be categorized into three stages, crack initiation, stable crack propagation, and fast fracture, as in crystalline alloys. The fatigue-endurance limits of the Zr-based BMGs vary significantly, ranging from 0.05 ~ 0.5 σ_{ys}, depending on the test geometry (experiments under tension-tension, compression-compression, or bending), test materials,

environments… etc. Gilbert et al. [31, 40] first reported the fatigue behavior of the Zr-based BMG (Vitreloy-1). They conducted four-point-bending tests on beam specimens and found that the fatigue limit was ~ 8% of the ultimate tensile strength (σ_{UTS}). Menzel et al. [39] later reported similar results using the same material. Yokoyama et al. [41] conducted rotating-beam fatigue tests to examine the Wohler curve of the Zr-based BMGs. The fatigue limit of the specimen in their experiments was ~ 57% of the ultimate tensile strength. Nakai et al. [42] studied the fatigue-crack initiation and small crack-propagation behavior of Zr-based BMGs under tensile stresses. They reported a fatigue limit of 52% of the ultimate tensile stress. Subsequent compression-compression fatigue studies of the same material showed a slightly-lowered fatigue limit of ~ 20% of the yield stress [43]. Launey et al. [44] examined the bending-fatigue behavior of Zr-based BMGs from two different manufacturers. They found that fatigue limits are strongly affected by the free volume in the material. The differences in fatigue limits can be as large as 22% of σ_{UTS} (40% σ_{UTS} for the BMG system with less free volumes and 18% σ_{UTS} for the system with more free volumes [44]). Wang et al. [32, 33, 38, 45] and Peter et al. [36, 37] performed tension-tension fatigue tests on notched Zr-based BMG samples. These tests showed that the fatigue limit is 30 ~ 50% of the ultimate tensile strength [46]. Wang et al. [47] suggested that several factors could affect fatigue limits, such as composition, mean stress, quality of the specimen, specimen geometry, testing environment, cyclic frequency, surface condition, etc.

Wang et al. [47] further summarized the fatigue–failure process of BMGs under a tensile-stress state and as illustrated in Figure 2-7. At the first step, the shear band(s) will

form when a BMG is cyclically deformed as shown in Figure 2-7(a). Consequently, in the shear band, voids can develop during deformation due to the free-volume coalescence [Figure 2-7 (b)]. The growth and linkage of voids will be assisted by a tensile-stress state, perhaps leading to a large stress concentration near these voids. Then, followed by the initiation of fatigue crack from these voids. The crack-initiation is attributed to the resultant stress concentration [Figure 2-7 (c)]. If the sample continues undergoing a cyclic-tensile load, the fatigue crack will open and grow. A small plastic zone will form at the crack tip, and this plastic zone can blunt the main crack tip. Meanwhile, multiple shear bands or crack branches could and will develop near the crack tip [Figure 2-7 (d)]. This crack-branching phenomenon was observed by Flores et al. [48] when they studied the crack-growth behavior of the $Zr_{41.25}Ti_{13.75}Ni_{10}Cu_{12.5}Be_{22.5}$ BMG. Hence, the fatigue crack will propagate along another favorable direction, as illustrated in Figure 2-7 (e). The process of blunting and resharpening of the crack tip will form the striated crack-propagation region when the fatigue experiments of BMG samples are conducted under a tensile-stress state [Figure 2-7 (f)]. In case that BMGs include inclusions and porosities, a crack will initiate from these casting defects easily. The fatigue crack will propagate following the process of blunting and re-sharpening.

As for the fatigue process under compression–compression, Wang et al. [47] suggest the fatigue-fracture surface is similar to that observed in the monotonic compression test, which forms by the unstable fracture along a primary shear band [49]. There are no fatigue striations observed on the fractured surface after the compression–compression fatigue according to the studies in [49, 50]. This trend implies that the

mechanism of the fatigue facture under the compression–compression stress seems to be similar to that under a compression-stress state. The free volume in a shear band is expected to increase during the deformation of BMGs. Any free volume created in a shear band during the deformation is highly unstable and tends to form nanometer-scale voids [51]. Since a compressive stress will retard the void growth and linkage, the fatigue crack is difficult to originate under a compressive-stress state. However, the formation of voids will decrease the density of the material and its resistance to deformation in the shear band. After several compression-compression fatigue cycles, one primary shear band gradually becomes weak and cannot sustain the compressive stress. Finally, the BMG sample fails along one primary shear band, which forms a shear-fracture angle with respect to the stress axis. This fact could also explain why the fatigue lifetime under a compression-compression cyclic loading was longer than that under a tension-tension cyclic loading. With a tensile-stress state, the growth of voids would be promoted by the tensile stress while a compressive stress state would retard the void growth.

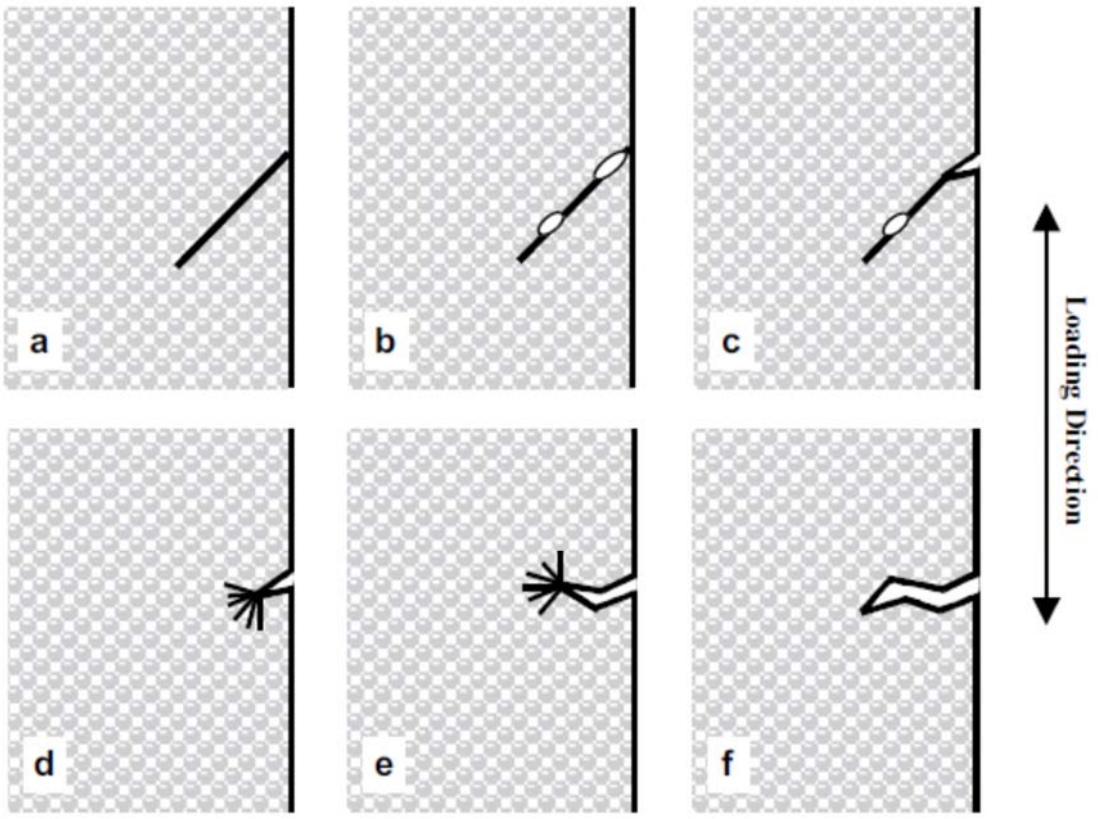

Figure 2-7 Proposed mechanisms of fatigue-crack initiation and propagation under a tension stress state.[47]

2.2 Ni-based superalloys

2.2.1 Fatigue damage mechanisms in crystalline materials

A general way of categorize the fatigue life of a crystalline material can be given as

$$N_T = N_i + N_p \quad (2\text{-}6)$$

where N_i is the number of cycles to 'initiation' of a crack-like defect and N_p is the number of cycles of propagation to critical dimension[52]. Classically, N_p can be described nicely using linear-elastic fracture mechanics (LEFM). The initiation life N_i is estimated using various approaches ranging from local stress-life approaches for high-cycle fatigue (HCF) to the Coffin-Manson equation for low-cycle fatigue (LCF), or combined approaches, such as the local strain-life equation, which combine these two over the full range of lives. The number of cycles to crack initiation typically relates to the formation of small cracks on the order of 0.5 mm to 2 mm in length. Such flaws are detectable. The label 'initiation life' is somewhat misleading since it includes processes of nucleation as well as the propagation of small cracks, alternatively termed as microcracks. In design for damage tolerance, the presence of an initial defect is assumed, and inspection intervals are set according to the application of propagation mechanics. Crack initiation mechanics do not provide much help in predicting the crack. This is a viable approach in structures where flaws can be monitored in critical locations, and where crack growth conforms to a well-established propagation law. In contrast, the initiation and growth of small cracks in reciprocating or rotary machinery subjected to HCF loading conditions may not be evident for the great

majority of total life, and in many cases the N_i term is dominant. The propagation behavior of small cracks during the 'initiation' phase is unfortunately not as well-characterized as that of long cracks.

A characteristic feature of HCF is the high degree of heterogeneity of local cyclic slip processes[53]. Microcrack distribution is also highly heterogeneous in homogenous macroscopic cyclic deformation states, the cyclic plastic slip processes are highly heterogeneously distributed among grains and surface crack density is sparse. There may also be an early transition to Stage II behavior, characterized by propagation normal to the direction of the maximum principal stress range. Persistent slip band (PSB) spacing and spacing of nucleated small cracks decreases with increasing strain amplitude. Typically, only a single dominant flaw ultimately propagates to failure in HCF and the crack density is relatively low in smooth specimens compared to the LCF case. There is a corresponding increase of scatter of fatigue strength under HCF conditions linked to this increasing heterogeneity.

Fatigue crack nucleation and growth occurs along a progression of length scales ranging from the order of 1 μm to the scale of individual grains, to long crack behavior where the scale of individual grains (50 μm -100 μm) is small compared to the crack length and the characteristic length scale for crack tip damage or the cyclic plastic zone, as illustrated in Figure 2-8. Each of these three scales corresponds to distinct mechanics treatments. Although implicitly embedded in the classical categorization of fatigue life, the identification of appropriate mechanics approaches for the lower scales and modeling of the transition from one dominant scale to the next are still not clear.

Stage I crystallographic (shear-dominated) microcrack growth is typically observed to transition to the Stage II growth regime for crack lengths on the order of 1 to 4 grain diameters. Figure 2-9[54] shows typical crack paths and crack length relative to grain size for uniaxial loading. High slip mobility on numerous systems promotes shear decohesion on conjugate slip planes at the crack tip, limiting Stage I coplanar growth and facilitating Stage II growth[54]. This transition depends on stress amplitude and stress state, and its conditions are not yet fully quantified. Propagation of long cracks in initially isotropic poly-crystals almost always exhibits Stage II growth, corresponding to mode I dominance.

Because of the distinction of the various length scales and associated mechanics approaches that are necessary, it is essential to define small or short cracks relative to long cracks. The behavior of long cracks may be predicted fairly well using conventional LEFM in most cases, whereas different approaches must be applied to sufficiently small or short cracks. Physically small cracks are those less than 1-2 mm in length. Below this, the notion of 'smallness' is governed by the ratio of crack size to microstructure (crack length < grain size). The microstructurally small or short cracks can be considered as the crack length is on the order of periodic microstructure, typically grain size. In some cases, colonies or packets of second phase in dual phase microstructures may define this length scale; in dual phase microstructures, influence of microstructure may persist up to crack lengths an order of magnitude longer than the characteristic grain sizes or mean second phase spacing. As distinguished from short cracks, microstructurally small cracks are those in which the crack length is on the order of microstructure in all dimensions. Microstructurally short cracks are those for which one dimension is on a scale much larger than the repeating

microstructure, but with length on the order of microstructure in the propagation direction. In both cases there is ample evidence to suggest that crack-microstructure interactions influence crack growth significantly, with stress state and amplitude also affecting such interactions. Mechanically small cracks are those which are physically small but no longer exhibit significant dependence on microstructure; the crack length for this transition to relative insensitivity is often on the order of 3-10 grain diameters. Mechanically small cracks may be correlated with long crack data using conventional fracture mechanics parameters that account for bulk plasticity and crack closure effects. [53]

To understand the behavior of small cracks in fatigue, one must consider the microstructure at grain level. A microstructure-sensitive fatigue model is required to predict the fatigue crack behavior at early stage of fatigue life. Dunne et al.[55, 56] studied low-cycle fatigue of polycrystalline Ni-based superalloy and confirmed that fatigue crack initiation is closely related to the cumulative plastic strain in the material. Grain morphology and orientation of their specimen were determined using EBSD, and polycrystal plasticity analyses carried out for the characterized microstructure with, in principle, identical conditions to the experiments. At the length scale of individual grains, fatigue crack nucleation and growth depends crucially on microstructure features such as grain boundaries, triple points, crystallographic orientation, and inclusions. It was found that crack nucleation occurred at free surface locations where localized slip banding was predicted to develop by the crystal plasticity analyses. Work by Manonukul and Dunne [56] on a similar polycrystalline material also adopted the accumulated plastic strain as key

fatigue damage parameter and their model captured the sites for fatigue crack formation in both HCF and LCF regimes as illustrated in Figure 2-10.

In their test[56], the free surface of the bend test sample was subject to a state of plane stress. The accumulated plastic strain distribution under these circumstances was also modeled and the results and comparisons with experimentally observed cracking are shown in Figure 2-10. The model test sample was subjected, in principle, to loading conditions identical to those in the experiments. The resulting free-surface cracking observed in the experiment is shown in Figure 2-10 (a), and the predicted distribution of accumulated plastic strain after one cycle of cyclic plasticity is shown in Figure 2-10 (b). Bands of intense slip are predicted to develop, emanating from the sample free surface at three particular locations.

Grain boundary regions seem to correlate with the development of the highest levels of plastic slip. Comparison of the simulated bands of slip localization with the experimentally observed sites of crack nucleation in Figure 2-10(b) on the free surface shows that the cracks which are observed to nucleate and grow lie within the predicted bands. The orientations of the propagating cracks also match those of the predicted slip patterns. However, crack formation was not observed experimentally in the left-most predicted slip band. Overall, the results indicate the importance of slip localization as reflected by a continuum measure of cumulative plastic strain on fatigue crack formation.

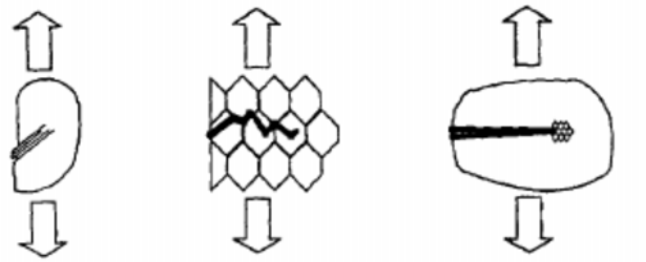

Figure 2-8 Progression of length scales in fatigue: (a) nucleation at PSBs or pre-existing defects, (b) crack length on the order of microstructure, and (c) long crack behavior.[53]

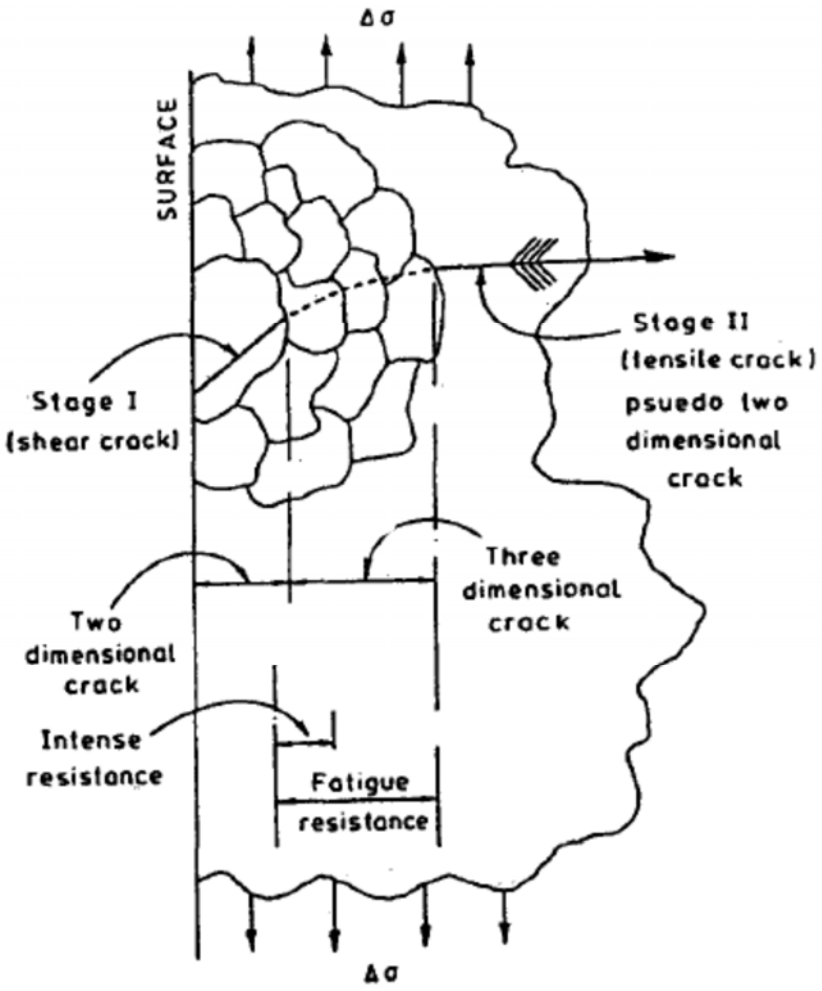

Figure 2-9 Stage I (shear) and Stage II (tensile) transition for uniaxial cyclic loading [54].

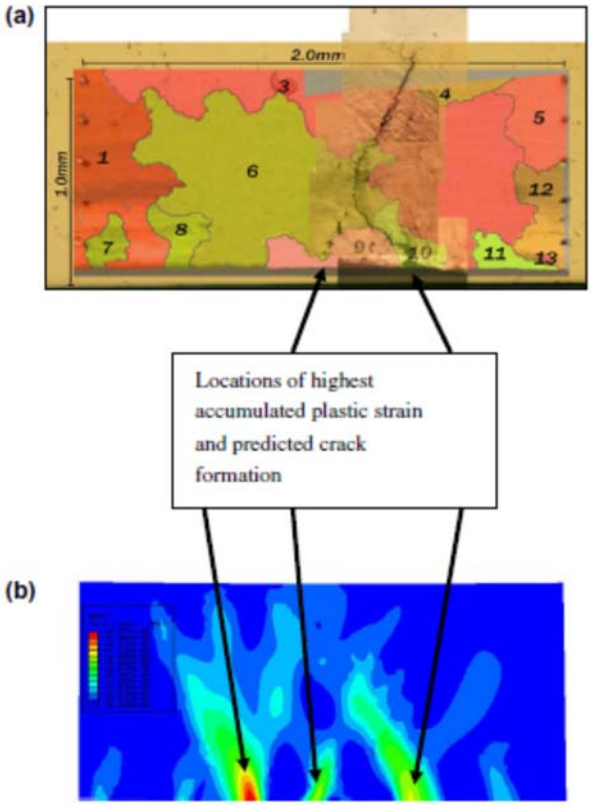

Figure 2-10 (a) Experimentally observed crack formation and early and growth under plane stress conditions and (b) the predicted site of fatigue crack formation and orientation based on the accumulated plastic strain. [56]

2.2.2 Fatigue-crack initiation behavior

It is generally agreed that the persistent slip bands (PSBs) are major nucleation sites for cracks in metals and alloys of high purity. The PSBs are thin lamellae where the plastic deformation is mainly concentrated during fatigue cycling. The plastic strain in the PSB lamellae is at least an order of magnitude higher than that in the matrix [57]. The cracks tend to form at the deep narrow intrusion, and the interface between the PSB and matrix, which is a plane of discontinuity and across which there are steep gradients in the density and distribution of dislocations. As schematically shown in Figure 2-11[58], the formation of PSBs leads to surface roughening, which is manifested as microscopic hills and valleys, commonly referred to as extrusions and intrusions. The intrusions function as micronotches, and the effect of the stress concentration at the root of the intrusions promotes the additional slip and fatigue-crack nucleation.

There is a wealth of experimental evidences indicating that the test environment plays important roles in fatigue-crack initiation. Gough et al. [59] and Wadsworth et al.[60], demonstrated that the fatigue life was markedly improved in dry, oxygen-free environment, as compared to the moist laboratory air. A well-accepted model is illustrated in Figure 2-12. When slip steps form during the tensile portion of a fatigue cycle in the laboratory air (or other chemically aggressivemedia), the oxygen (or other species) is absorbed on the freshly created slip steps to form an oxide layer (or other reaction products). Part of the oxide layer is drawn into the body of the crystal in the compression part of the cycle. This process is repeated, and more oxides are pushed into the matrix along the slip band, weakening the PSBs of the crystal and eventually leading to cracking. Cracks

can also be initiated at grain boundaries in embrittling environments (which preferentially attack grain boundaries or the particles on them) and at high temperatures (at which grain-boundary cavitation and sliding could occur).

The crack initiation in crystalline engineering alloys is very complicated. It could happen at voids, slag or gas entrapments, inclusions, dents, scratches, forging laps and folds, macroscopic stress concentrations, as well as regions of microstructural and chemical non-uniformities. In metals and alloys of high purity, cracks usually initiate at the free surface. In commercial alloys, it is common to see fatigue cracks nucleate at both near-surface and interior locations. The exact initiation sites are often specific to the alloy system considered. In high-strength Ni-base superalloys, for example, cracks have been found to initiate near the large defects, either pores or nonmetallic inclusions [61]. At ambient temperature, the fatigue cracks initiate at defects near the surface for both the low and high strain ranges applied. At high temperatures, cracks nucleate at the interior of the specimen when low-strain ranges are applied. However, when the high-strain ranges are applied, surface-crack nucleation is dominant. One of the objectives of this study is to correlate the microstructural changes to the fatigue life at the fatigue-crack-initiation stage by synchrotron X-ray scattering related techniques.

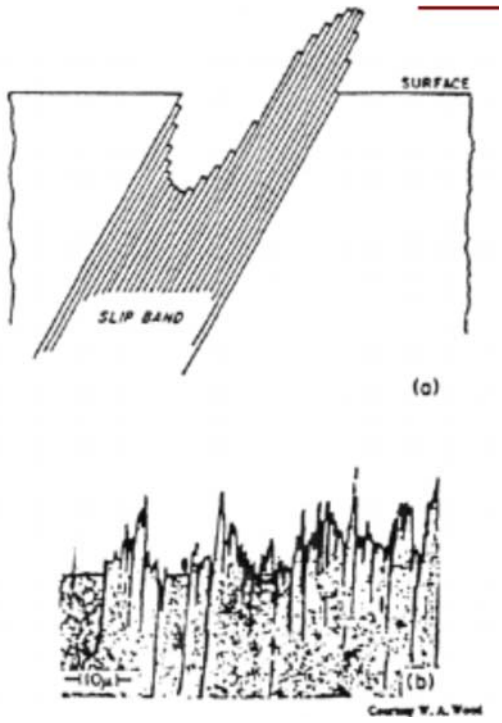

Figure 2-11 Schematic shows the roughening of surfaces due to the formation of persistent slip bands (PSBs).[58]

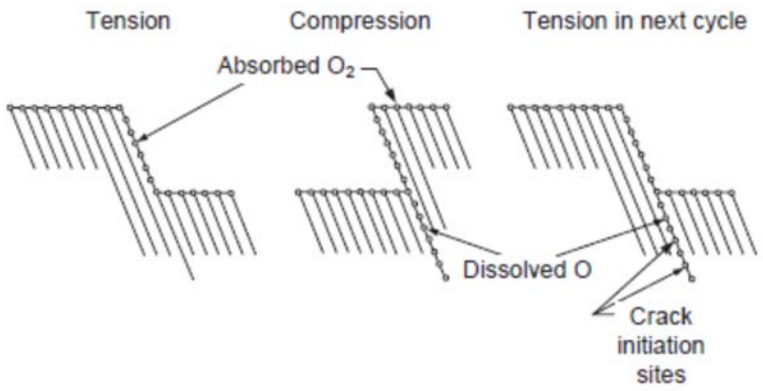

Figure 2-12 A model for fatigue crack initiation near a free surface by the synergistic effect of single slip and environmental interactions.[60]

2.3 Scientific issues and objectives

For the studies of fatigue behavior of BMGs, most research focus on the stress-life behavior of the material, and the actual structure changes in atomic scale due to cyclic loading are not fully addressed. Thorough the literature survey, the scientific issues are identified as follow.

1. Due to the structural features in BMGs (lack of grain-boundaries and dislocations), how does the atomic structure of BMGs change under mechanical deformation?
2. How does cyclic loading affect the structure of BMGs on an atomic scale?
3. Does cyclic loading cause the globalized fatigue damage to BMGs or is the fatigue damage localized? Can the fatigue-endurance limit of BMGs be improved?
4. Is there a fatigue-damage parameter present in the Ni-based superalloy that can be probed by nondestructive techniques?

The present research will focus on using experimental methods to address those issues. The overall objective of the research is to study the fatigue damage of both amorphous and crystalline alloys at the "initiation" stage of fatigue life by x-ray scattering techniques as illustrated in Figure 2-13. The results will provide a mechanistic understanding of fatigue damage in BMGs, and find a fatigue-damage parameters to better predict the fatigue life of Ni-based alloys.

A wide range of issues regarding fatigue crack initiation, fatigue damage mechanism in amorphous and polycrystalline engineering alloys, and how these fatigue-induced structural changes can be assessed by x-ray scattering techniques will also be addressed in the later chapters. That will include (1) Providing mechanistic understanding

of the elastic deformation in amorphous metallic materials at atomic scale, (2) Studying the effect of cyclic loading on the structure of BMGs. (3) Understanding the fatigue failure mechanism of BMGs. (4) Understanding of the grain-level stress/strain distribution around fatigue-crack initiation sites of an engineering alloy. (5) Developing an advanced, non-destructive characterization method to evaluate the fatigue damage of an in-service alloy.

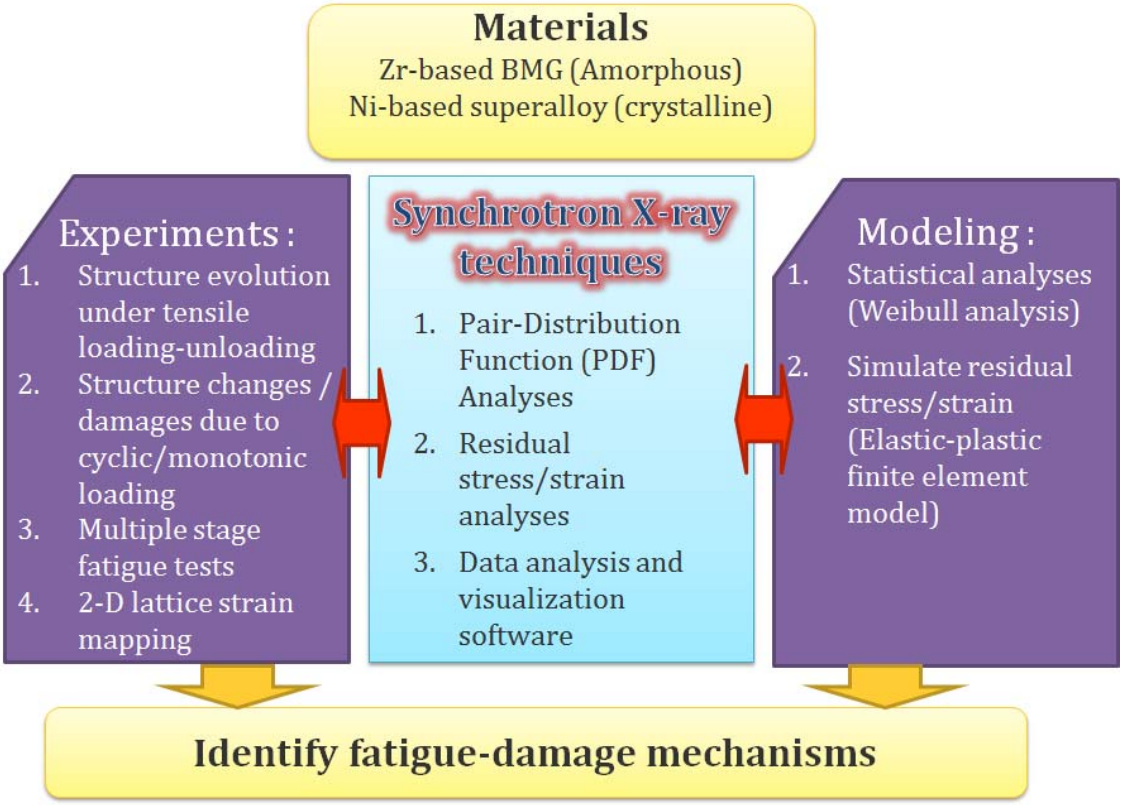

Figure 2-13 Illustration of the overview of the present research.

3 CHAPTER III

MATERIALS AND EXPERIMETNAL PROCEDURES

3.1 Fabrication of BMGs

There are many ways as shown in Figure 3-1 to make glassy alloys. From gaseous phase, one could use vapor deposition methods to make amorphous thin film. From liquid phase, rapid solidification techniques are the major way to fabricate amorphous alloy. Even when an alloy is crystallized in solid form, one can still use techniques like ion-implantation and mechanical alloying to turn it into amorphous alloy. Nevertheless, ion-implantation, mechanical alloying, vapor deposition can only make amorphous alloy in the forms of ribbon, thin film or powders. The only way to fabricate bulk metallic glasses today is rapid solidification of molten liquid.

BMGs are multicomponent alloy which could freeze without crystallization during solidification. Since it is in metastable state, the fabrication of BMGs has imposed a barrier to broad commercial adoption, particularly where the processing requirements of these alloys conflict with conventional metal processing methods. The fabrication of BMGs requires extra care.

The first thing to be considered in making BMGs is the cooling rate. In order to facilitate sluggish crystallization kinetics of an alloy during processing from the melt, a condition that enables the retention of the amorphous (liquid) structure, the molten alloy must be quenched relatively quickly, otherwise crystallization will occur when the cooling

or heating path intersects with the crystallization curve of the Time-Temperature-Transformation (TTT) diagram (Figure 3-2). In Figure 3-2, Blue curves represent the start-crystalline-transformation of conventional crystalline alloy, conventional metallic glass, and bulk metallic glasses. Olive green curve represents the complete-crystalline-transformation. These curves tell the volume fraction transformed if held at a particular temperature. The solid arrow (path-1) and dash arrow (path-2) show the different cooling rate. The majority of alloys will crystallize upon solidification. Conventional metallic glass can be made with extremely high cooling rate, but in the form of ribbons. A special combination of metallic elements, we called BMG formers, can have their TTT curve moved rightward, and open the possibility of making them into large-size metallic glass (mm to cm in its smallest dimension). In order to obtain amorphous alloy, the cooling path of the molten liquid should follow the path-1 indicated in Figure 3-2 to be lowered below T_g. The required cooling rate is typically larger than 10^2 K/Sec.

The second is the environment of the processing chamber. Impurities, especially oxygen, have detrimental effect on the glass forming ability of BMG former. A few hundred a-ppm of oxygen is found to destabilize the amorphous structure and cause decalescence during cooling from the molten liquid state [62].

Direct casting, and thermal-plastic forming are two common ways in practice to fabricate BMGs. Direct casting methods such as die casting, suction casting have been used as BMG net-shape fabrication. The formation of amorphous structure and the forming of the alloy into its final shape are made in a single step. It is usually done by pouring the molten alloy directly into the cooled mold, which is made by materials, usually metal, with

good thermal conductivity. While in thermal-plastic forming method, the forming and cooling to render the amorphous state during solidification are decoupled. Due to the simplicity of the processing procedure, equipment and the cost consideration, direct casting method was selected to fabricate BMG in this thesis.

Because of the complexity of the fabrication process, and the variety of chemical systems, mass production of BMG has not been commercialized yet. In the current study, all of the specimens were made in laboratory by a machine that composed of an environmental controlled arc-melting chamber and a suction casting apparatus. The machine has the ability to make the ingot, and cast the BMG in one step (without venting the chamber) and quickly change the mold to make specimen with various dimensions. A more detailed description of the machine can be found elsewhere [63]. The master ingot of the alloy was prepared by arc-melting the mixture of high-purity transition metals, Zr (> 99.95 % mass fraction), Cu (99.99 %), Ni (99.995 %), Al (99.9995 %), and Ti (99.995 %), in a water-cooled copper crucible under an argon atmosphere. The ingot was re-melted several times (> 4) before being ejected into a water-cooled copper mold to produce the desired shape. The as-cast ingot is shown in Figure 3-3(a). A mirror-like surface is a good indication of high quality glass. If the chamber contains high level of unwanted elements, such as oxygen or nitrogen, the ingot will be colored (turn yellow and gold for excess nitrogen, turn gray, black, blue, or green for excess oxygen), and the specimen made by these kind of ingot will not be in pure amorphous form.

6 mm in diameter rods, and 50 mm x 15 mm x 2 mm plates are made using the same procedure. Plate samples (2mm thick) with composition of $Zr_{52.5}Cu_{17.9}Ni_{14.6}Al_{10}Ti_5$ were

used to study the deformation behavior of BMG under monotonic tensile stress. Rod samples (6mm in diamter) with composiiton of $(Zr_{55}Cu_{30}Ni_5Al_{10})_{98}Er_2$ were used to study the effect of fatigue on the sturcutre and mechanical properties of BMG.

All of the specimens used in the experiments were examined by high-energy X-ray diffraction (XRD) in transmission geometry and differential-scanning calorimetry (DSC) prior to any tests to ensure that the specimens were in a fully amorphous state. All specimens showed a lack of sharp diffraction peaks by XRD and a distinct, reproducible glass transition point by DSC.

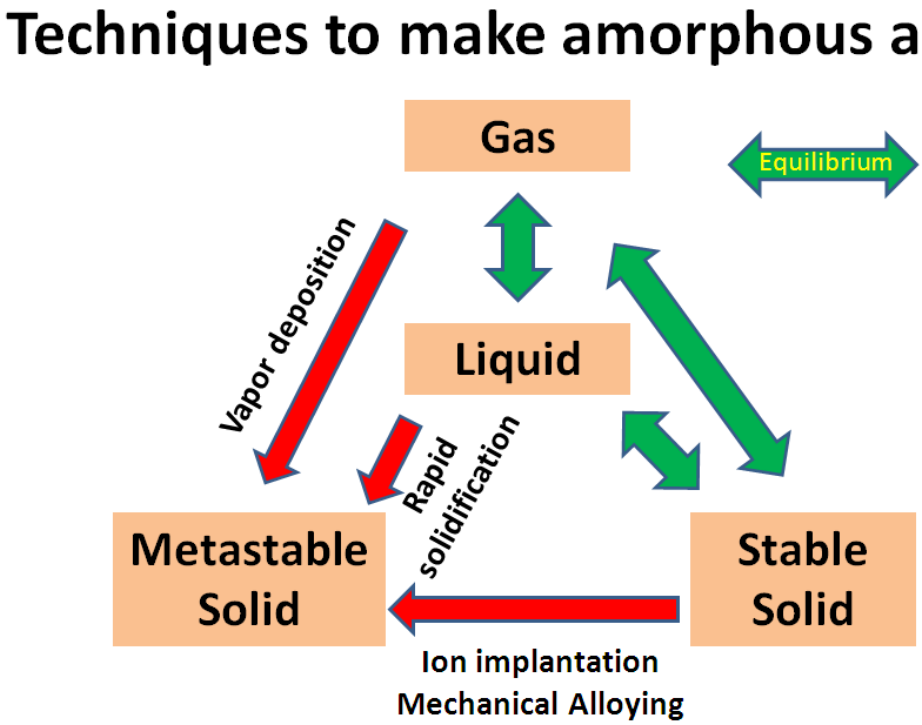

Figure 3-1 Techniques used to make amorphous alloys.

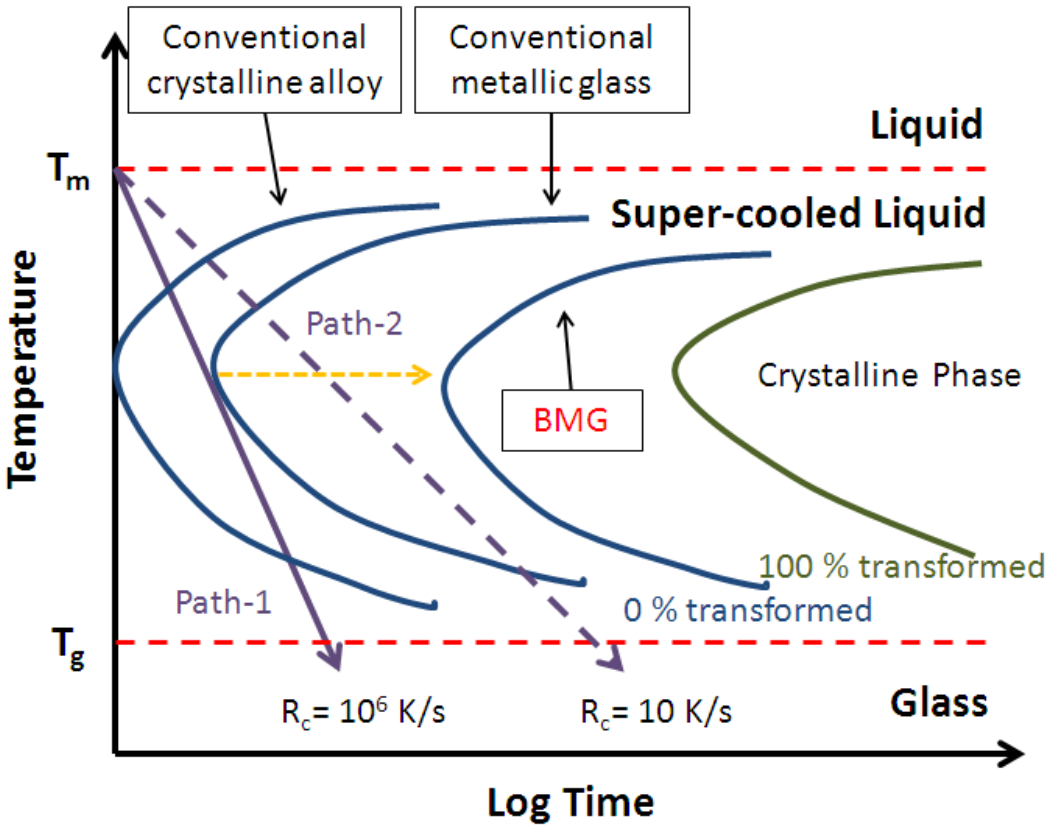

Figure 3-2 Schematic Illustration of a TTT diagram. Blue curves represent the start-transformation of conventional crystalline alloy, conventional metallic glass, and bulk metallic glasses. Olive green curve represents the completed transformation. These curves tell the volume fraction transformed if held at a particular temperature. The solid arrow (path-1) and dash arrow (path-2) show the different cooling rate. The majority of alloys will crystallize upon solidification. Conventional metallic glass can be made with extremely high cooling rate, but in the form of ribbons. A special combination of metallic elements can have their TTT curve moved rightward, and open the possibility of making them into glass, and making them in bulk form (mm to cm in its smallest dimension).

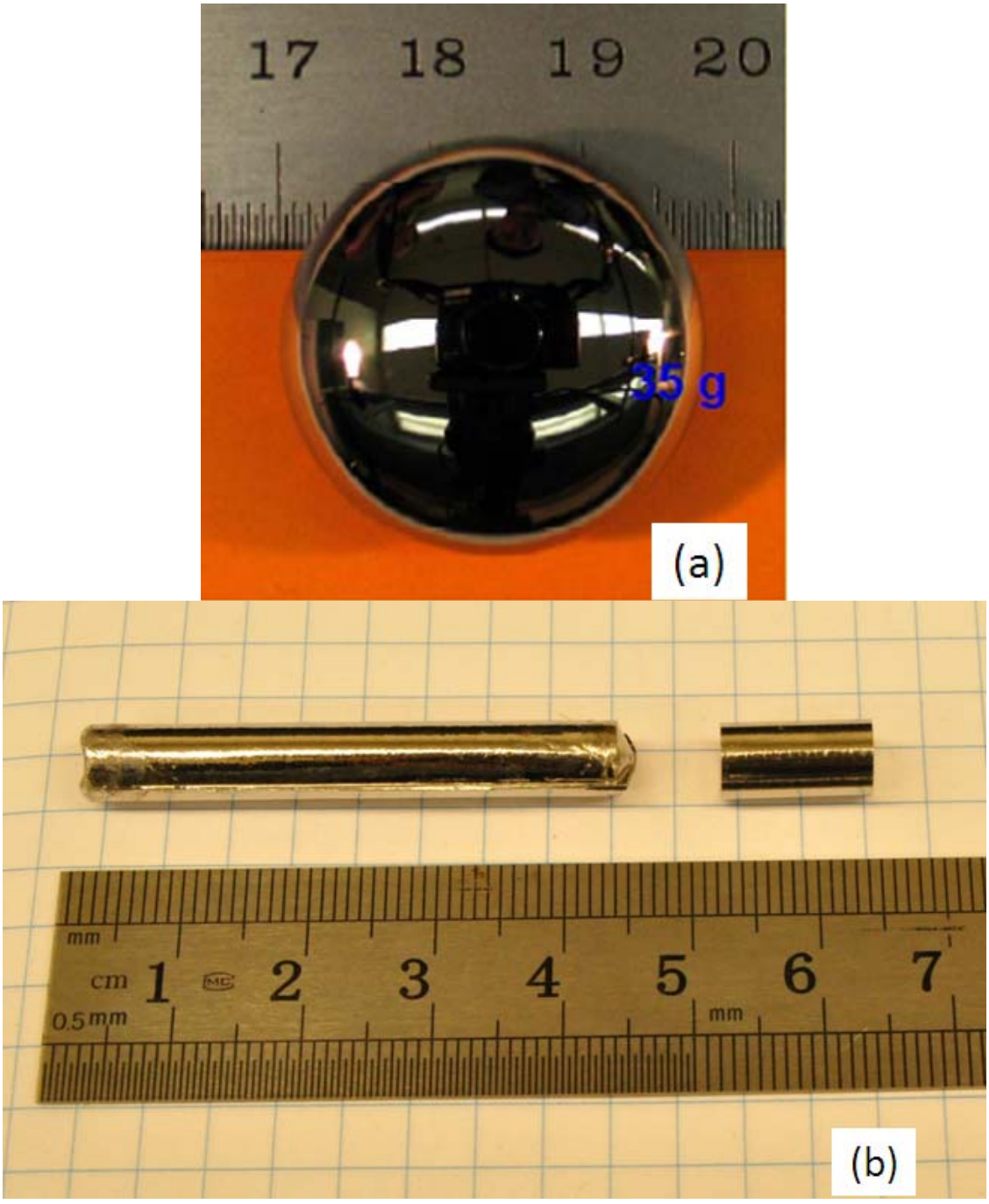

Figure 3-3 (a) the as-cast ingot of $Zr_{55}Cu_{30}Ni_5Al_{10}$. The mirror-like surface suggests it's in amorphous form. [Courtesy of Dr. Lu Huang] (b) An as-cast 5mm in diameter, cylindrical rod. The composition is $Zr_{52.5}Cu_{17.9}Ni_{14.6}Al_{10}Ti_5$ (Vit-105), one of the best glass formers.

3.2 Fatigue experiments of BMGs

A computer-controlled material test system (MTS, Model-810) was used for fatigue studies. Samples were tested under a load-control mode at a fixed stress range of 720 MPa, a load ratio [R, the minimum stress ($\sigma_{min.}$) divided by the maximum stress ($\sigma_{max.}$)] equal to 10 (i.e., R = 10, $\sigma_{max.}$ = - 80 MPa, and $\sigma_{min.}$ = - 800 MPa), and a frequency of 2 Hz using a sinusoidal waveform. The stress level was selected, based on the regular fatigue test of the same material with the same diameter under similar testing conditions (10 Hz, a fixed L/D ratio of 1.67, where L is the length of the specimen, and D is the diameter of the specimen). At this stress range, the fatigue life is around ~ 8 x 10^5 cycles. During fatigue experiments, peak and valley load values for individual cycles were intermittently recorded for verification. The test was ended when the sample was fractured. Then the sample was collected for visual inspections. The fractured part was cut by EDM for detailed surface characterization. The fracture-surface morphology was examined by a Leo-2010F high-resolution scanning-electron microscope (SEM). The undamaged part after cutting out the fracture surface was preserved for the 2^{nd}-round fatigue experiment using the same testing conditions. The sample for the 2^{nd}-run fatigue has smaller L/D ratios since the length is shorter. The same procedure was repeated until the L/D ratio of the left-over was less than 0.8.

The fatigue tests of each run were recorded for analyses. The schematic diagram of the above experimental plan is shown in Figure 3-4. Note that cutting of the damaged parts was purely determined by visual inspection. It is possible that there are hidden cracks inside the sample. These pre-existing cracks will certainly have a strong impact on the fatigue life

during the 2nd test. Two out of six samples failed within few cycles of the second tests. These samples were excluded from our analysis, since they most likely had pre-existing cracks from the first test.

The schematic diagram of the experiment is shown in Figure 3-4. The experiment is a series of constant-load compression-compression fatigue tests. For the first run, denoted as the 1st run, an as-cast BMG specimen is used. The repeated loading/unloading fatigue process continues until the specimen fails. Then, the broken/damaged region is removed, as illustrated in the figure, and the left-over is used for the 2nd-run test. The experimental condition of the 2nd-run is identical to the 1st-run test, except that the sample is shorter, since the fractured region was removed. The series of tests was continued until the L/D ratio of the left-over was less than 0.8. Jiang et al. [64] studied the effect of sample geometry on the deformation behavior of Zr-based BMGs under compression tests. They confirmed that as long as the L/D ratio is larger than 0.75, it will not affect the fracture mode and mechanism of BMGs under compression. Therefore, we only used samples with L/D larger than 0.8 for continuing the fatigue experiments.

Comparing the fatigue life of each run helps clarifying mechanisms of fatigue damage of BMGs. If the fatigue life of the 2nd-run test is longer than the 1st-run test, then the fatigue test produces only localized damage to the specimen. Once the crack is initiated, the damage is mainly accumulated around the existing crack, while the remaining part of the sample still undergoes elastic deformation. After the damaged region is removed, the rest of the sample is just like the as-cast sample but with fewer defects, since the weakest point of defects in the specimen has been screened out by the 1st-run fatigue test. Hence,

the next fatigue test will show a longer fatigue life than the first one. On the other hand, if the 1st-run test had the longer fatigue life than the 2nd-run test, cyclic loading produces globalized damage to the specimen. The crack will initiate more easily on the fatigued specimen. Therefore, the fatigue life will be shorter. In the present study, we found that the 2nd-run test has a similar or longer fatigue life than the 1nd-run test. Thus, the fatigue life of a large diameter specimen under a compressive stress could be controlled by the number of pre-existing crack-initiation sites (defects) in the specimen.

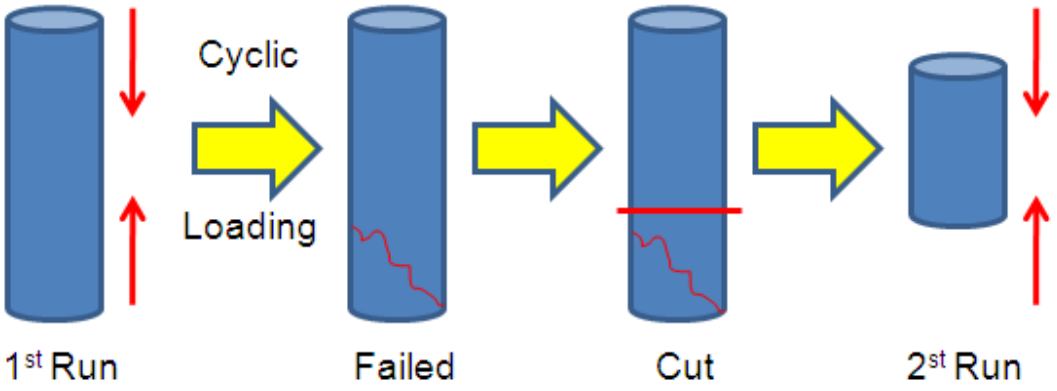

Figure 3-4 A schematic diagram of the experimental design. The as-cast sample undergoes compression-compression fatigue until it fails. Then, the damaged part is cut off, and the left-over is used for the next fatigue test as long as the rest part has an L/D ratio greater than 0.8.

3.3 Surface and Fracture Morphology

Surface and fracture morphology of the samples were examined first by optic microscopy (OM) and were examined by a LEO 1526 scanning electron microscopy (SEM) with the energy-dispersive spectroscopy (EDS). The specimens were ultrasonic-cleaned in acetone for 5 mins and air-dried before the examination.

3.4 Pair-Distribution-Function (PDF) analysis

3.4.1 Theory

The atomic PDF, $G(r)$, is defined as

$$G(r) = 4\pi r[\rho(r) - \rho_0] \qquad (3\text{-}1)$$

where r is the radial distance, ρ_0 is the average atomic number density, and $\rho(r)$ is the atomic pair-density function (PDF), defined as,

$$\rho(r) = \rho_0 g(r) = \frac{1}{4\pi N r^2} \sum_{\nu} \sum_{\mu} \delta(r - r_{\nu\mu}) \qquad (3\text{-}2)$$

where δ is a Dirac delta function. The function $g(r)$ is called the atomic pair distribution function (PDF). The function $G(r)$ gives information about the number of atoms in a spherical shell of unit thickness at a distance r from a reference atom. It shows peaks at characteristic distances, $r_{\nu\mu} = |r_\nu - r_\mu|$, separating pairs of atoms (ν^{th} and μ^{th} atoms). The sums are taken over all the atoms in the sample, and the resulting curve is a histogram of all the atom-atom distances in the solid. In practice, there are so many atoms in the material

that $\rho(r)$ becomes a quasi-continuous distribution function. Figure 3-5 shows a typical PDF of an amorphous metallic alloy. The composition of the BMG is $(LaCe)_{65}Co_{25}Al_{10}$. The atomic pair density function, $\rho(r)$, of the specimen was measured by high energy X-ray scattering at ID-11-C, Advanced Photon Source, Argonne National Laboratory. It shows the generic behavior of an amorphous material. At low-r, the data diminish to zero below a certain value because two atoms cannot come too close to each other. At high-r, PDF curve oscillate around $\rho_0 = 0.038\,(1/\text{Å}^{-3})$ and gradually converge to ρ_0 in which equivalent to g(r) = 1. In between the PDF oscillates showing atomic correlations (deviations from the average number density). There is a large peak at the average atomic separation of 3.6 Å, representing the nearest neighbors, followed by oscillations due to short-range-order. These oscillations, which is referred to as "correlations", show useful local structural information regarding the local environment of atoms, such as how many neighbors there are and how far away they are. Although the PDF is only the one-dimensional projection of the three-dimensional atomic structure, it is possible to recreate the three-dimensional structure with a relatively high degree of confidence by creating a three-dimensional model who's PDF agrees with the experimental PDF.

Now we have the PDF function, but how can we obtain this function through experiment? It happened that the microscopic real-space density of a material is simply given by a Fourier transform of the scattering amplitude, $\Psi(Q)$. Similarly, the Fourier transform of the scattered intensity, in the form of the structure function $S(Q)$, yields the atomic pair distribution function, g(r), defined by Equation $G(r) = 4\pi r[\rho(r) - \rho_0]$ (3-1).

$$G(r) = 4\pi r[\rho(r) - \rho_0] = \frac{2}{\pi}\int_0^\infty Q[S(Q) - 1]sin(Qr)dQ \qquad (3\text{-}3)$$

The structure function is related to the coherent part of the total diffracted intensity of the material.

$$S(Q) = \frac{I^{coh}(Q) - \sum c_i \left|f_i(Q)\right|^2}{\left|\sum c_i f_i(Q)\right|^2} + 1 \qquad (3\text{-}4)$$

where $I^{coh}(Q)$ is the measured scattering intensity from a powder sample that has been properly corrected for background and other experimental effects and normalized by the flux and number of atoms in the sample. Here, c_i and f_i are the atomic concentration and X-ray atomic form factor, respectively, for the atomic species of type i. This relation is extremely useful and important because that $S(Q)$ is a directly measurable quantity and g(r) is a quantity of profound physical importance; the crystal structure can be determined from it. Since $\rho_0 g(r)$ is a representation of the microscopic atomic pair density, this relationship allows us to directly measure the relative positions of atoms in a solid. A straightforward numerical Fourier transform of our measured scattering intensity, $S(Q)$, can be carried out in a computer according to Equation 2.7 to yield g(r), the pair-distribution function.

In single crystal scattering studies, the Bragg peak intensities are sometimes Fourier transformed. This results in a periodic real-space pair-correlation function known as the "crystallographic Patterson function" [65]. The PDF is related to the Patterson function. Usually, only the Bragg peaks are used in calculating the Patterson function which

therefore has the periodicity of the lattice. Both the Bragg peaks and diffuse intensity are included in obtaining the PDF. Thus the PDF does not necessarily have the lattice periodicity, and will be able to describe the deviations from lattice periodicity. One may also say that the PDF defined by Equation 2.7 is a spherically averaged generalized Patterson function.

The inverse transformation of Equation 3-1 can be defined and it yields the structure function S(Q) in terms of G(r).

$$S(Q) = 1 + \frac{1}{Q}\int_0^\infty G(r)Sin(Qr)dr \qquad (3\text{-}5)$$

The experiments to obtain S(Q) and further PDF are straightforward X-ray and neutron powder diffraction measurements. They are typically carried out at synchrotron X-ray sources and pulsed neutron sources, rather than on laboratory sources, because it is important to measure data over a wide range of momentum transfer, Q, for high accuracy and adequate real-space resolution of the PDF peaks. Since Q is equal to $4\pi \sin\theta / \lambda$ (for elastic scattering), and the Q range of > 25 $Å^{-1}$ are desirable, this suggest that short-wavelength, high energy, X-rays or neutrons are required. Based on the requirement (Q > 25 $Å^{-1}$), the X-ray energy of > 25 keV (λ = 0.496 Å) is required, but considering the geometry of the experimental setup and the X-ray penetration power, energies of 70 keV (λ = 0.177 Å) to 120 keV (λ = 0.103 Å) are typically used. Data from laboratory sources with Mo as target can give acceptable results, but working at a synchrotron or spallation neutron source is always to be preferred for the highest resolution measurements.

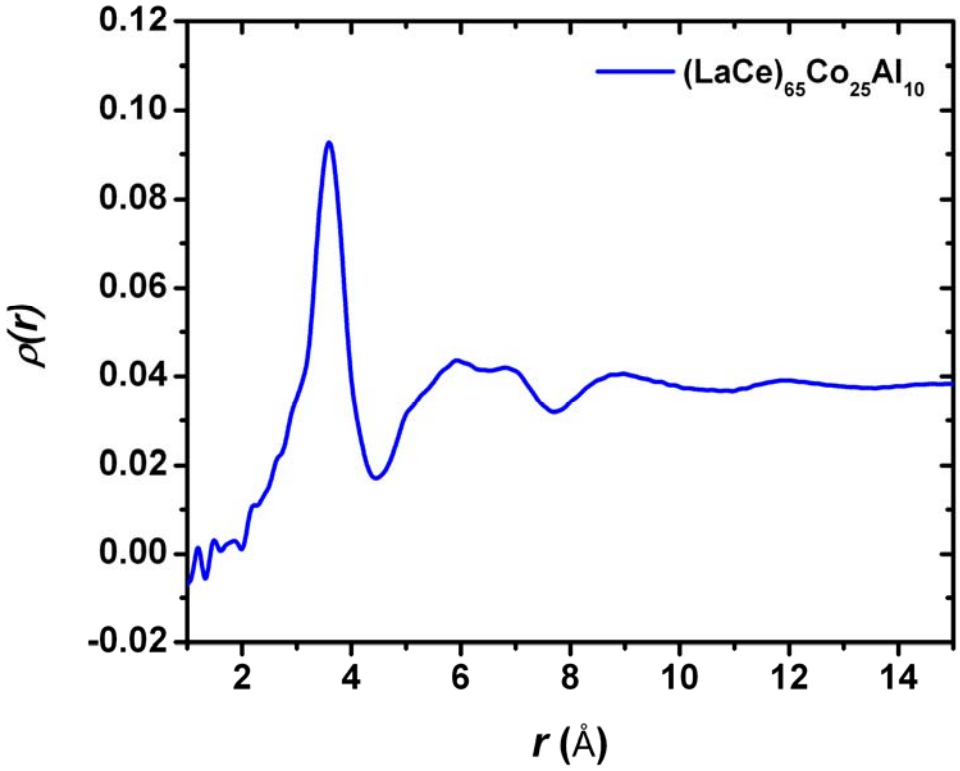

Figure 3-5 The atomic pair density function, $\rho(r)$, of a bulk metallic glass $(LaCe)_{65}Co_{25}Al_{10}$ measured by high energy X-ray scattering at ID-11-C, Advanced Photon Source, Argonne National Laboratory. It shows the generic behavior of an amorphous material. The data diminish to zero at low-r and to $\rho_0 = 0.038\,(1/\text{Å}^{-3})$ at high-r equivalent to g(r) = 1. In between the PDF oscillates showing atomic correlations (deviations from the average number density). For example, a greater probability of finding an atom at the hard-sphere separation distance of 3.6 Å, followed by a less than average probability of finding a neighbor between the first and second neighbor shell at 6 Å.

3.4.2 Ex-situ high-energy synchrotron X-ray scattering experiments

The structures of the as-cast and fatigued specimens were characterized by the HEXRD [Figure 3-6(a)]. The experiment was conducted at the 1-ID-C beam-line of the Advanced Photon Source (APS), Argonne National Laboratory. The samples were cut into a 1-mm-thick plate with the plane normal to the loading direction, as shown in Figure 3-6 (b), and were examined using 100 keV (with a wavelength, λ_{avg} = 0.12398 Å) radiation in a transmission geometry. The intensity of the scattered X-rays was collected by a MAR345 image plate. The experimental geometry is illustrated in Figure 3-6 (a). The final beam size was 0.025 x 0.1 mm. The data were processed and converted into tables of the scattering intensity versus scattering angle, θ, employing the FIT2D software [27].

To further examine the effect of cyclic loading on the short-range atomic structure, the pair-distribution function (PDF) analysis was performed. The measured scattering intensity, I(Q), was integrated over the azimuthal direction, and corrected for the polarization effect, fluorescence background, absorption, inelastic scattering, and the scattering from the air and container using the methods described in [66] to obtain the structure function, S(Q). The corresponding pair-distribution function, $G(r)$, was obtained by the Fourier transformation of the S(Q), where $S(Q)$ is the structure factor.

The failed specimen was sliced vertically along the loading axis, as shown in Figure 3-6 (c), and the structure characterization was performed along the loading direction. This geometry allows us to characterize the anisotropy term of the specimen under cyclic compression. In addition, the microstructures of the regions near and away from the fracture plane can be compared.

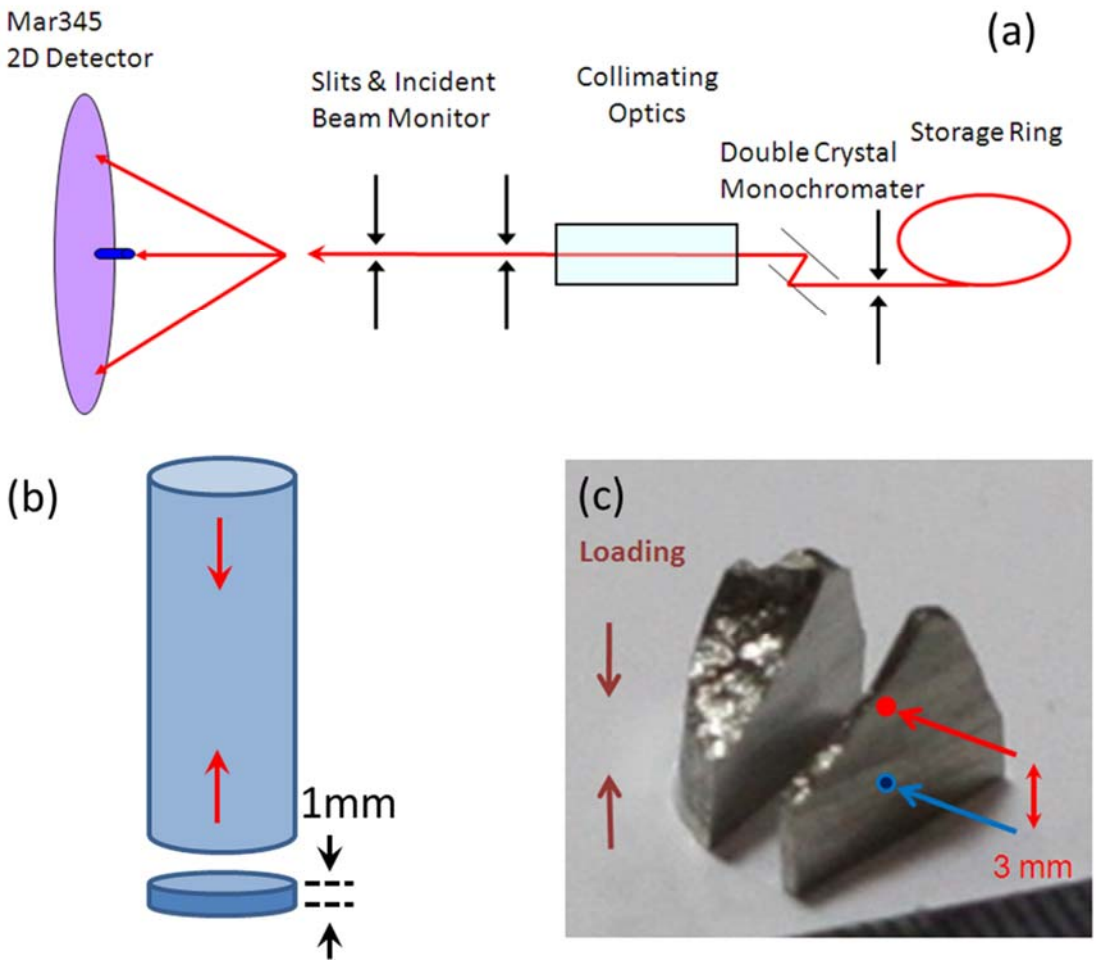

Figure 3-6 . (a) A schematic diagram of the high-energy synchrotron X-ray experiment at the 1-ID-C beam line of the Advanced Photon Source (APS), Argonne National Laboratory. The energy of the incident beam is 100 keV with a beam size of 0.025 x 0.1 mm^2. (b) Sample geometry-1 for HEXRD measurements. A 1-mm-thin plate is sliced from the rod with the plate normal parallel to the loading direction. (Red arrows indicate the loading direction.) (c) Sample geometry-2 for HEXRD measurements. The specimen was sliced into a 0.5-mm-thick plate. The scattering intensity is collected in a transmission mode. Note that the beam size in the vertical direction is only 0.025 mm.

3.4.3 In-situ high-energy synchrotron X-ray scattering experiments

The in-situ x-ray diffraction measurements were carried out at the 1-ID/XOR beam line of the Advanced Photon Source, Argonne National Laboratory. The incident energy was tuned to 120 keV ($\lambda = 0.10332$ Å). The beam size was 0.2 mm x 0.2 mm. The MAR345 area detector was placed 40 cm behind the sample to collect the diffracted x rays. The maximum Q value that can be probed for this setup is 24.6 $Å^{-1}$. The samples used were Vit-105 metallic glasses with the composition of $Zr_{52.5}Cu_{17.9}Ni_{14.6}Al_{10}Ti_5$. Samples were prepared by suction casting method with an arc-melter described in Section 2.1. The samples were cut by electric discharge machining (EDM) into dog-bone shapes, with the gauge area being 9.5 mm long as shown in Figure 3-7. The samples were polished to the final thickness of 0.67 mm and the width of 2 mm. The sample was placed in a tensile grip in a MTS load frame Model 858. Sample grips were encircled in an infrared heater with a front opening of ±30 degrees. The design of the heater permitted unobstructed scattering from the sample. The external stress was varied from 0 to 1.2 GPa with a 0.2 step. After reaching 1.2 GPa the temperature was increased to 300 °C and held for 30 min to induce creep deformation. After 30 min the sample reached the steady state rate. Then the sample was cooled and after reaching room temperature the external load was removed. The detail loading and heating procedure is shown in Figure 3-8. The elongation after reaching room temperature was 2%. At each step x-ray scattering was collected for approximately 1 h. For each measurement step frames were summed and the background due to dark current was subtracted. Data were then normalized by the incident beam monitor, and the expansion into spherical harmonics The g(r) were obtained by Fourier-transforming S(Q)

$$g(r) = 1 + \frac{1}{2\pi^2 r \rho_0} \int [S(Q) - 1] \sin(Qr) Q dQ \qquad (3\text{-}6)$$

where ρ_0 is the number density of atoms, with Q either parallel or perpendicular to the stress axis.

However, the above equation is only valid for when the material is isotropic. For anisotropy bodies, such as BMG under an applied stress, the structure function as well as PDF need to expand by the spherical harmonics, $Y_l^m(x)$,

$$g(r) = \sum_{l,m} g_l^m(r) Y_l^m(\frac{\boldsymbol{r}}{r}) \qquad (3\text{-}7)$$

$$S(r) = \sum_{l,m} S_l^m(Q) Y_l^m(\frac{\boldsymbol{Q}}{Q}) \qquad (3\text{-}8)$$

which are connect through spherical Bessel transformation

$$g_l^m(r) = \frac{(i)^l}{2\pi^2 \rho_0} \int S_l^m(Q) J_l(Q) Q^2 dQ \qquad (3\text{-}9)$$

where J(x) is the spherical Bessel function. Note that only for the isotropic component ($l = 0$), $J_0(x) = \frac{\sin x}{x}$ and Eq 2.10 is recovered. For axial symmetry, $l = 1,3,5,...$ and $m \neq 0$ terms become zero, only the terms with $l = 2,4,6,...$ and $m = 0$ have to be evaluated. The following normalization condition is used for the spherical harmonics

$$\int Y_l^m(\Omega) Y_{l'}^{m'}(\Omega) d\Omega = 4\pi \delta_{ll'} \delta_{mm'} \qquad (3\text{-}10)$$

where $d\Omega = \sin\theta d\theta d\phi$, and θ, ϕ are standard polar angles. For axial symmetry, m=0 and ϕ defines angle between $\mathbf{Q}$ and the stress axis. If only the ℓ=2 term is considered, the $S(Q)$ can be expressed as

$$\begin{aligned} S(Q,\theta) &= Y_0^0(\theta,\varphi)S_0^0(Q) + Y_2^0(\theta,\varphi)S_2^0(Q) \\ &= S_0^0(Q) + \sqrt{\frac{5}{4}}(3\cos^2\theta - 1)S_2^0(Q) \end{aligned} \qquad (3\text{-}11)$$

Since $Y_0^0 = 1$ and $Y_2^0 = \sqrt{\frac{5}{4}}(3\cos^2\theta - 1)$. The $g_2^0(r)$ is then obtained by the transformation of the $S_2^0(Q)$ where

$$J_2(x) = \left(\frac{3}{x^2} - 1\right)\frac{\sin x}{x} - \frac{3\cos x}{x^2} \qquad (3\text{-}12)$$

and $x = Q \cdot r$. Because of symmetry all terms of $S_\ell^m(Q)$ with ℓ = odd are zero.

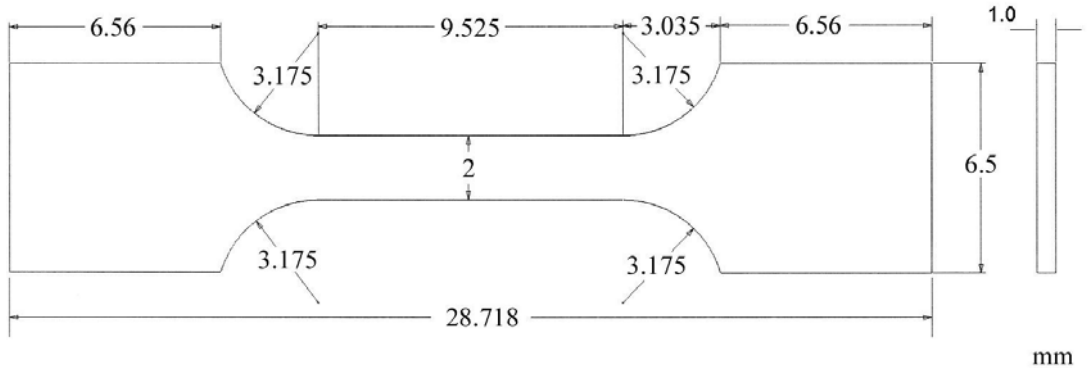

Figure 3-7 Sample dimension for the in-situ tension experiment.

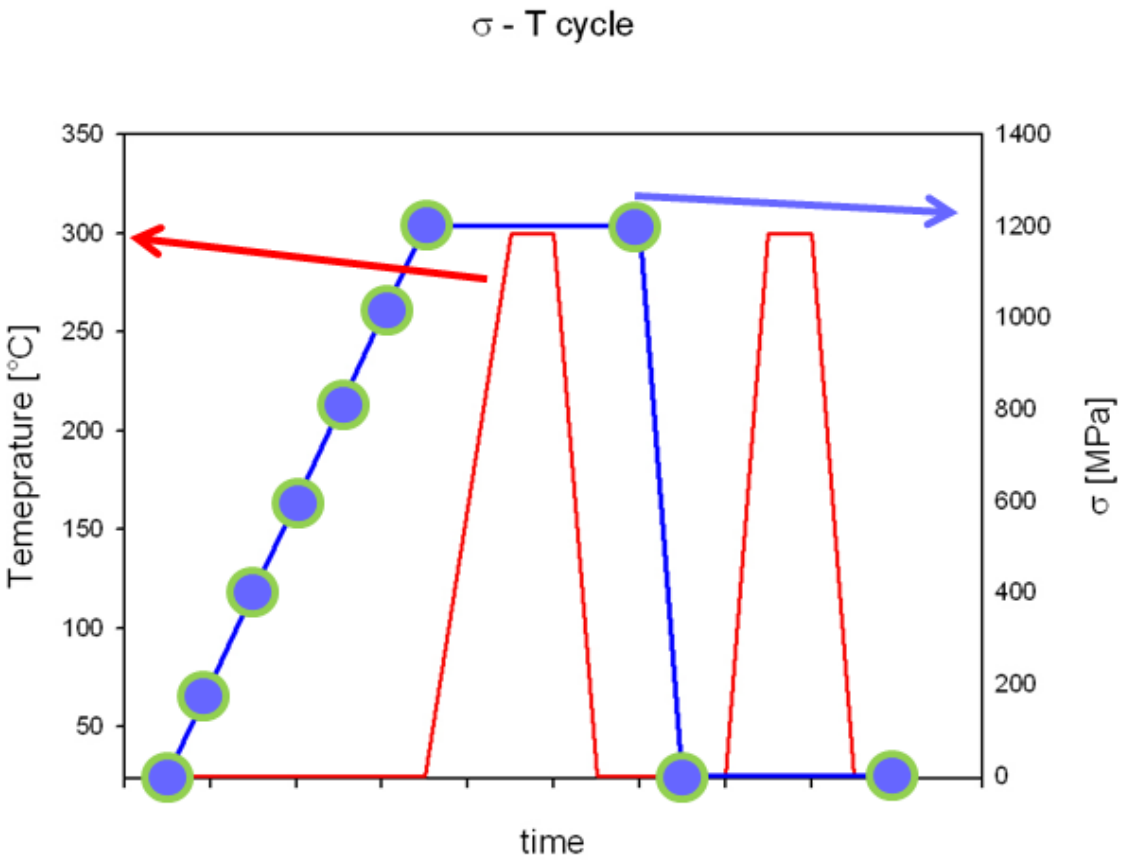

Figure 3-8 Schematic diagram of the experimental procedure.

3.5 Ni-based superalloy

The material used in the present study is a Ni-based superalloy developed by GE. It was developed to be more damage tolerant than Rene' 95. Hence the designation, while offering improved creep strength and fatigue crack growth resistance. The chemical composition of the material is listed in Table 3-1. The production allov is always processed through the powder metallurgy route. The Standard heat treatment consists of: a-super-solvus solution of 1.0 hr at 1150°C , followed bv a delayed oil quench, and aging for 8.0 hr at 760°C. Its main structural characteristics are thus a fine grain size, achieved through PM consolidation, and a duplex distribution of γ', the coarser forming on cooling from the super solvus solution, the finer predominantly on aging. The material is used in disk applications in advanced General Electric (GE) engines. The microstructure is mainly composed of the γ matrix phase (disordered face-centered cubic of Ni-based solid solution) and Ni_3Al-type γ′ precipitates (ordered L_{12} structure which is also a cubic). The cubic lattice parameters of γ and γ′ are very similar and the X-ray diffraction measurement described in this report cannot separate the lattice strain contribution from each phase. As the elastic moduli of γ and γ′ were reported to have very similar values, this treatment should not cause concerns.

Table 3-1 Composition of Ni-based superalloy (in mass percent).

Element	Ni	Co	Cr	Mo	W	Al	Ti	Nb	C	B	Zr	Fe
Mass%	balance	13	16	4	4	2.1	3.7	0.7	0.03	0.015	0.03	Max 0.5

3.6 Fatigue experiment of Ni-based superalloy

The material used in the present study is a polycrystalline Ni-based superalloy developed by GE. The specimens were prepared by electro-discharge-machining (EDM) of a plate with a thickness of ¼" to the double-notched dog-bone like plates. The gauge area has a dimension of 1" x 0.4" x 0.05" with four notches. The detail geometry is shown in Figure 3-9. The EDM was used to minimize the damage in the sample preparation process. The raw material has an estimated grain size of 20~50 μm and a random initial texture. Prior to the fatigue tests, the samples were mechanically polished and cleaned. The fatigue tests were performed in atmosphere at elevated temperature, ~400 ˚C, by a computer-controlled material testing system (MTS). The tests are in tension-tension mode and have a fixed stress range of 1995 lbf, an R-ratio ($\sigma_{min}/\sigma_{max.}$) equal to 0.05 (i.e., $\sigma_{max.}$ = 2100 lb., and $\sigma_{min.}$ = 105 lb.), and a frequency of 0.5 Hz using a triangle waveform. Three specimens were tests until fail to obtain the expected-fatigue-life of the material at current experimental condition. Based on the expected-fatigue-lift, a series of samples were pre-fatigued to 1%, 10%, 50%, 75% and 100% (broken) of its expected-fatigue-life under the same testing condition, and these samples were used for the present study. All of the pre-fatigued specimens, from 1% to 75% of the expected life, were still intact and had no visible macro cracks even under the maximum tensile load (2100 lb).

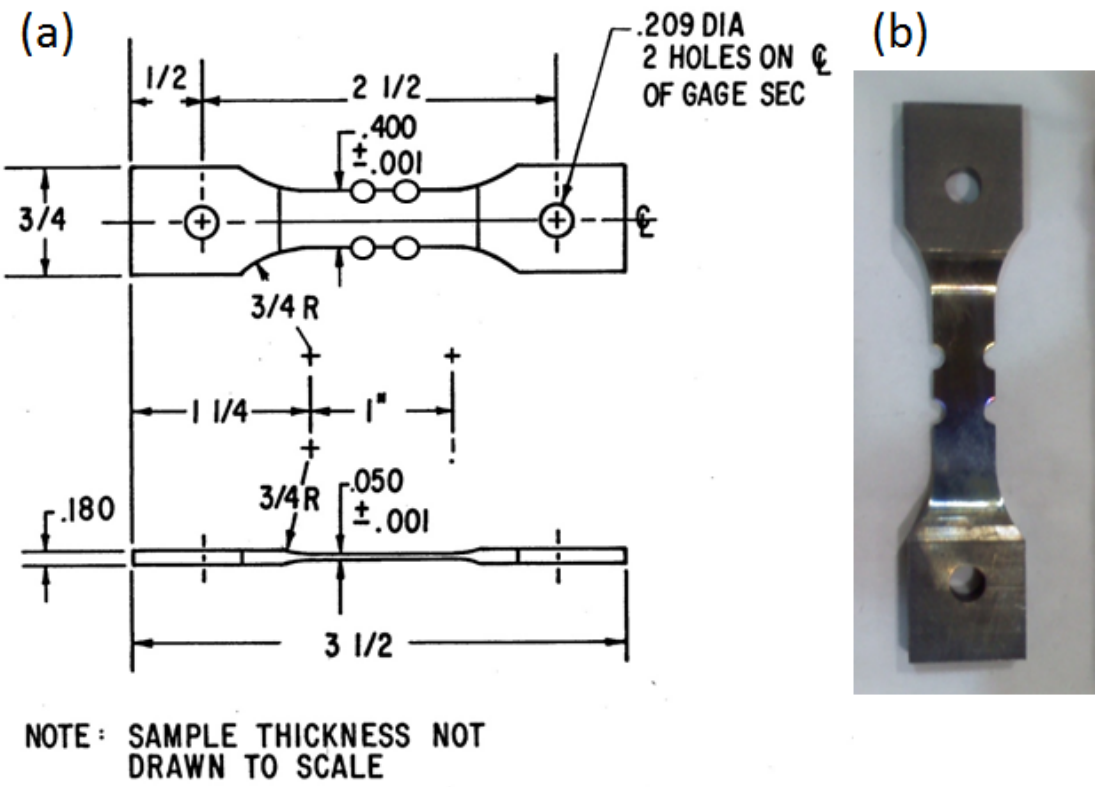

Figure 3-9 (a) Geometry of the double-notched specimen. (b) The picture of a specimen after the fatigue test and prior to the X-ray experiment. The specimen remains intact after pre-fatigue test.

3.7 In-situ lattice strain mapping by high energy synchrotron X-ray

The X-ray diffraction experiments were performed at 1-ID-C beamline of the Advanced Photon Source, Argonne National Laboratory. A high energy monochromatic X-ray beam of 70 keV was prepared by monochromator and a series of focusing optics and slits. The beam size on the specimen was 50 x 50 μm, positioned between two notches as shown in Figure 3-10. The measurement was in transmission mode, which means that the incident beam transmits through the sample and produces Debye rings in the forward direction, as illustrated in Figure 3-11. The diffraction pattern was recorded by a 2D detector (GE amorphous-Si, with 2048 x 2048 pixels and 0.2 mm pixel-to-pixel distance), located 880 mm from the sample. A 15 kN MTS servo-hydraulic load-frame was used to provide a peak load force up to 2200 lbf. The sample temperature of 400 ºC was maintained by a quartz-lamp IR furnace. For each sample, 2D diffraction patterns were taken as a function of load, from 0 lbf to 2100 lbf, with 100 lbf interval and 0.5 second data collection time. There were two types of measuring modes (line-scan, and map-scan) utilized in this study which cover different region of interests on the specimen. A line-scan, which consists of 18 points as shown in green dot in Figure 3-12(a), was used to monitor the evolution of lattice strain along notch-notch line. Two map-scans were used to collect the information around the notch with coarse-mapping (575 points) covers the entire notch area, and fine-mapping (316 points) focus only on the notch tip (plastic zone). The grid for coarse and fine-mapping were shown in blue and red dots in Figure 3-12 (a), respectively. All of the three modes have the measuring grid denser close to the notch, and looser away from the notch. The selection of the measuring positions provide the highest spatial resolution while

minimizing the data collecting time at different stress level. The line-scans were performed at each load level (100lb in step), and the mapping-scan were conducted at zero (5 lb.), half (1050 lb.), and maximum load (2100 lb.). The complete measuring scheme is illustrated in Figure 3-12 (b) and (c). A picture of the setup is shown in Figure 3-13.

The 2D diffraction pattern, as shown in Figure 3-14, consists of multiple diffraction rings with different hkl. The azimuthal angle, ϕ, is defined as 0° in the transverse direction, and as 90° along the loading direction. When the specimen is under a tensile load, the lattice spacing along the loading direction will expand, and in the transverse direction will contract. As a result, the diffraction ring will undergo an elliptical distortion, and such a distortion is the basis for further strain analysis. To facilitate the analysis, the diffraction rings were divided along the azimuthal direction into 360 slices (one degree each), and each slice can be considered as a 1D diffraction pattern.

Such 1D patterns were analyzed by Matlab® programs to obtain diffraction peak positions by fitting peaks with Voigt function. The lattice spacing for each hkl plane can be calculated from Bragg Law, $2d \sin\theta = \lambda$. Figure 3-15, for example, shows the variation of lattice spacing of (3 1 1) as a function of azimuthal angle under three different loads, 0 lbf, 1000 lbf, and 2100 lbf. Under zero load, the d-spacing remains constant vs. azimuthal angle. With increasing load, the lattice spacing increases along the loading direction (ϕ =90° and 270°), but decreases in the transverse direction according to the Poisson's ratio. The lattice strain as a function of ϕ is calculated according to $\varepsilon_{hkl}^{\phi} = \frac{d^{hkl} - d_0^{hkl}}{d_0^{hkl}}$, where d_0^{hkl} can be determined from data collected under zero load.

The general formula for calculating ϕ–dependent lattice strain using 2D detector is given by He

$$f_{11}\varepsilon_{11} + f_{12}\varepsilon_{12} + f_{22}\varepsilon_{22} + f_{13}\varepsilon_{13} + f_{23}\varepsilon_{23} + f_{33}\varepsilon_{33} = \varepsilon_{hkl}^{\phi} \quad (3\text{-}13)$$

where ε_{ij} are strain tensor components, and f_{ij} are diffraction geometry related coefficients. As the specimen was under a uniaxial load, we assume a bi-strain model, which means $\varepsilon_{11} = \varepsilon_{33}$, $\varepsilon_{12} = \varepsilon_{23}$, and $\varepsilon_{13}=0$ (see Figure 3-11). Under the bi-strain model, equation 3-13 can be simplified as:

$$\varepsilon_{hkl}^{\phi} = (f_{11} + f_{33})\varepsilon_{11} + (f_{12} + f_{23})\varepsilon_{12} + f_{22}\varepsilon_{22} \quad (3\text{-}14)$$

where

$$f_{11} = \sin^2\phi\cos^2\theta$$

$$f_{12} = -\sin 2\phi\cos^2\theta$$

$$f_{22} = \cos^2\phi\cos^2\theta$$

$$f_{23} = -\cos\phi\sin 2\theta$$

$$f_{33} = \sin^2\theta$$

θ is the diffraction peak position at azimuthal angle ϕ. For high-energy diffraction, θ is small and $\sin\theta \approx 0$ and $\cos\theta \approx 1$, equation (3-14) can be further simplified as:

$$\varepsilon_{hkl}^{\phi} \approx \sin^2\phi\,\varepsilon_{11} - \sin 2\phi\,\varepsilon_{12} + \cos^2\phi\,\varepsilon_{22} \quad (3\text{-}15)$$

When ε_{12} is zero (or very small), the observed strain is dominated by the first and the third terms, which gives arise the double sinuous curve with minima at $\phi = 90°$ and 270° respectively (Figure 3-15). When the shear strain ε_{12} is not negligible, the sinuous

strain curve will be shifted from 90° and 270°. In the current experiment, as the local stress is along the loading direction, ε_{12} is zero.

As the material has relatively large grains (20-50 μm) and beam size on the sample is small (50 x 50 μm), the number of grains within the probing volume (0.05 x 0.05 x 1.6 mm) satisfying the Bragg condition is limited. This is apparent from the "spottiness" of the diffraction rings shown in Figure 3-14. The implication to strain analysis is that at a particular azimuthal angle, the diffraction peak could be from a single or a few grains, and their strains could be skewed locally by inter-granular stress. To rectify the possible local deviation from inter-granular stress, the strain values, ε_{11}, ε_{22} and ε_{12}, were obtained by fitting all data points between 0° and 360° in ϕ with a sinuous curve defined by the bi-strain model (as shown in Figure 3-16)

Due to the fact that lattice strains along transverse direction (ε_{11}) come from different sets of grains, other than the diffracted grains along axial direction, the measured ε_{11} lattice strains for different hkl orientation versus stress were scattered.

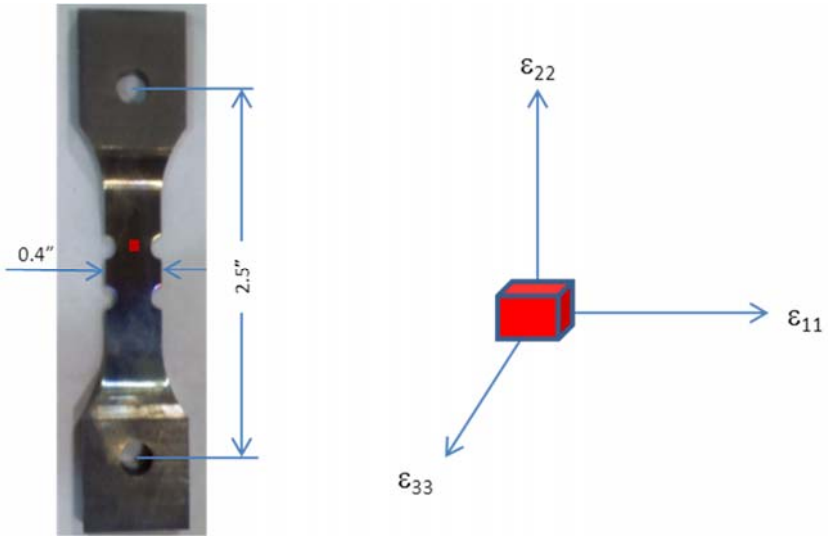

Figure 3-10 Notched flat-plate specimen used in X-ray diffraction measurement. The plate thickness is 0.065" (1.6 mm). The X-ray beam, 0.05 x 0.05 mm in size, was positioned between notches, as designated by the red square. The coordinate system for strain components is illustrated on the right, in which ε_{22} is along the loading direction.

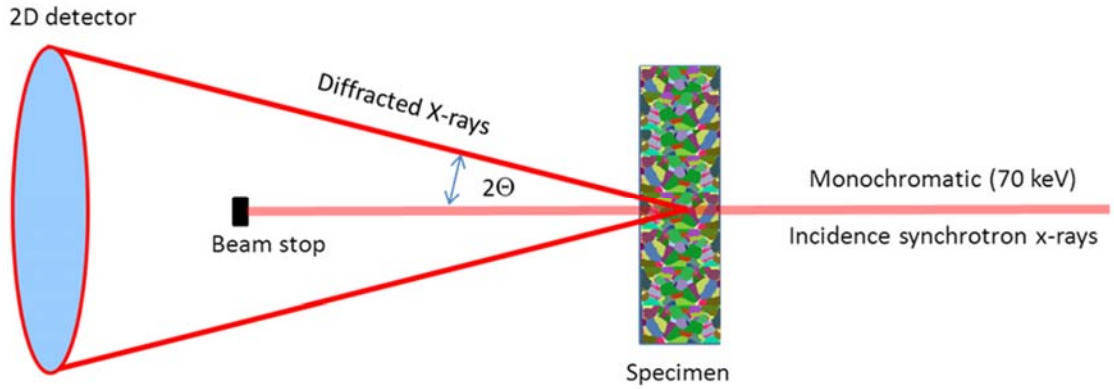

Figure 3-11 Illustration of the synchrotron high-energy X-ray diffraction experiment in transmission mode. A high-energy X-ray beam of 70 keV transmits the specimen and produces diffraction rings recorded by a 2D detector.

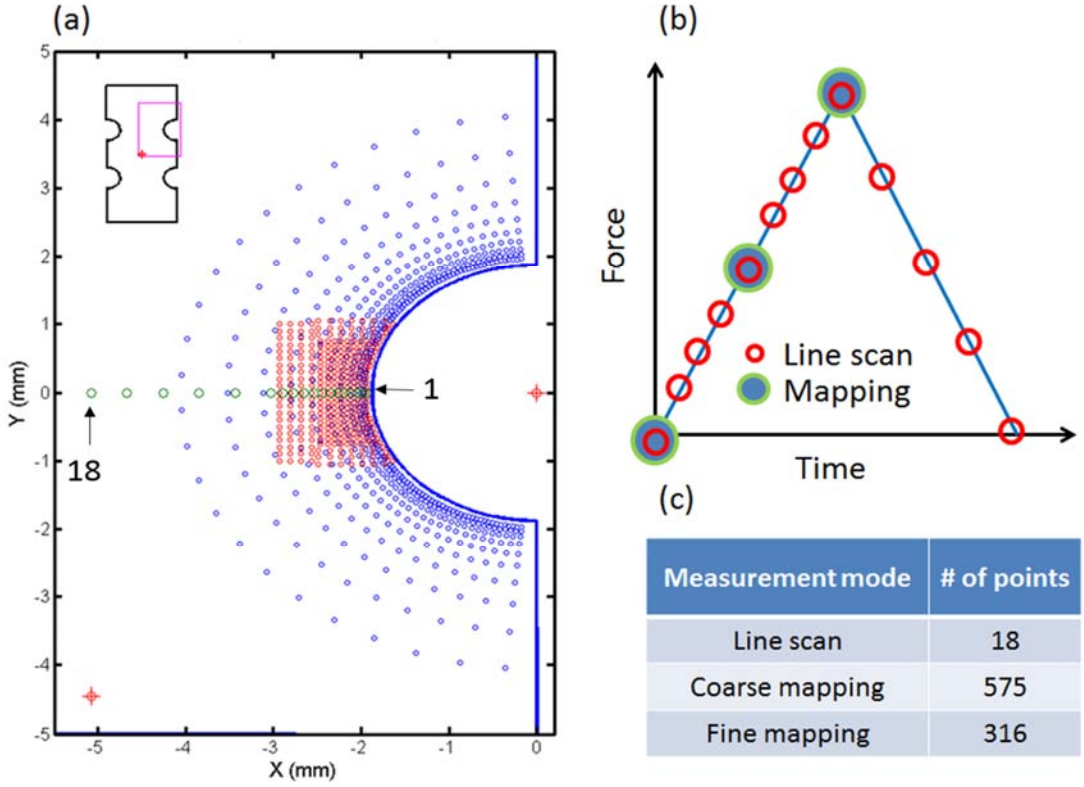

Measurement mode	# of points
Line scan	18
Coarse mapping	575
Fine mapping	316

Figure 3-12 Illustration of the measuring grid around notch. The origin (0,0) is at the center of the notch labeled by point-1. The blue, red and green dots represent three different measurement mode, coarse-mapping, fine-mapping, and line scan. The lower cross-circle is the center of the whole specimen. (b) The sequence of the diffraction measurement. Each specimen was pulled gradually from 0 to the maximum of 2100 lb. At every 100lb from zero to maximum load, line scan was conducted, and at 5lb, 1050lb, 2100lb, both coarse-mapping and fine-mapping were measured. (c) A table showing number of exposures at each measuring mode. Line-scan was measured along the two notches from notch tip to the vertical center line. Two map-scans cover the area near notch with coarse-mapping covering the entire notch, and fine-mapping covering the plastic zone. In all three modes, the grid is denser close to the notch, and looser away from the notch.

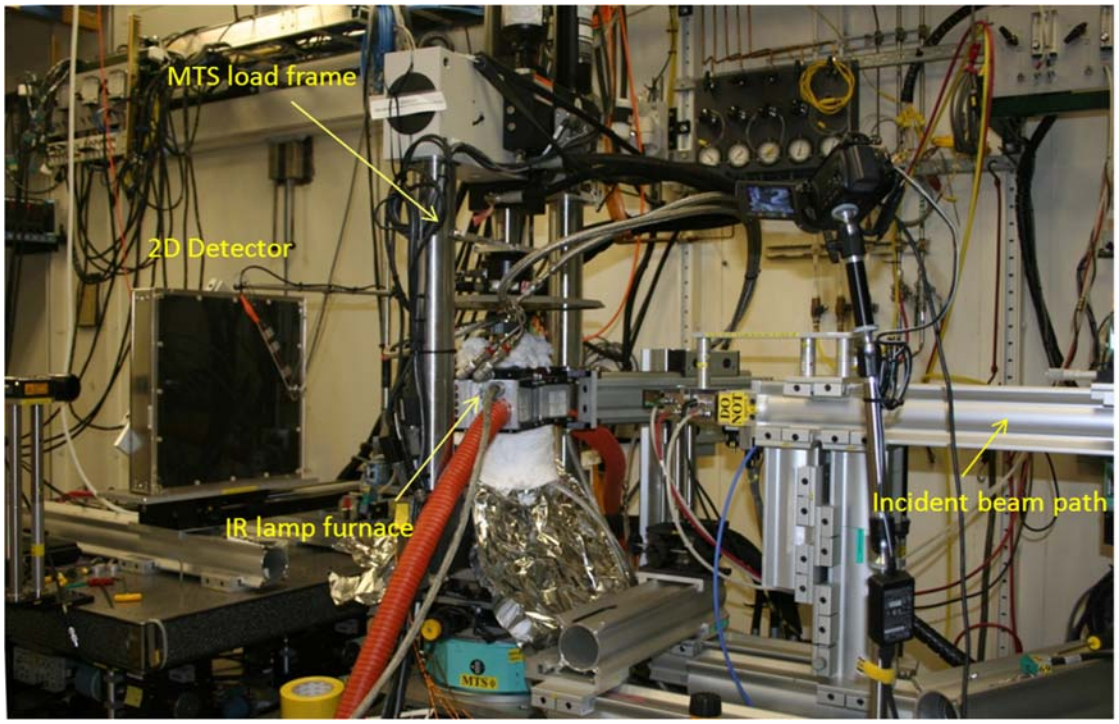

Figure 3-13 The experimental setup at 1-ID-C beamline. The specimen (invisible) is inside the IR lamp furnace, where the heat is provided by 12 halogen lamps. The MTS load fame is mounted on motorized stages for adjusting sample positions with respect to the incident beam.

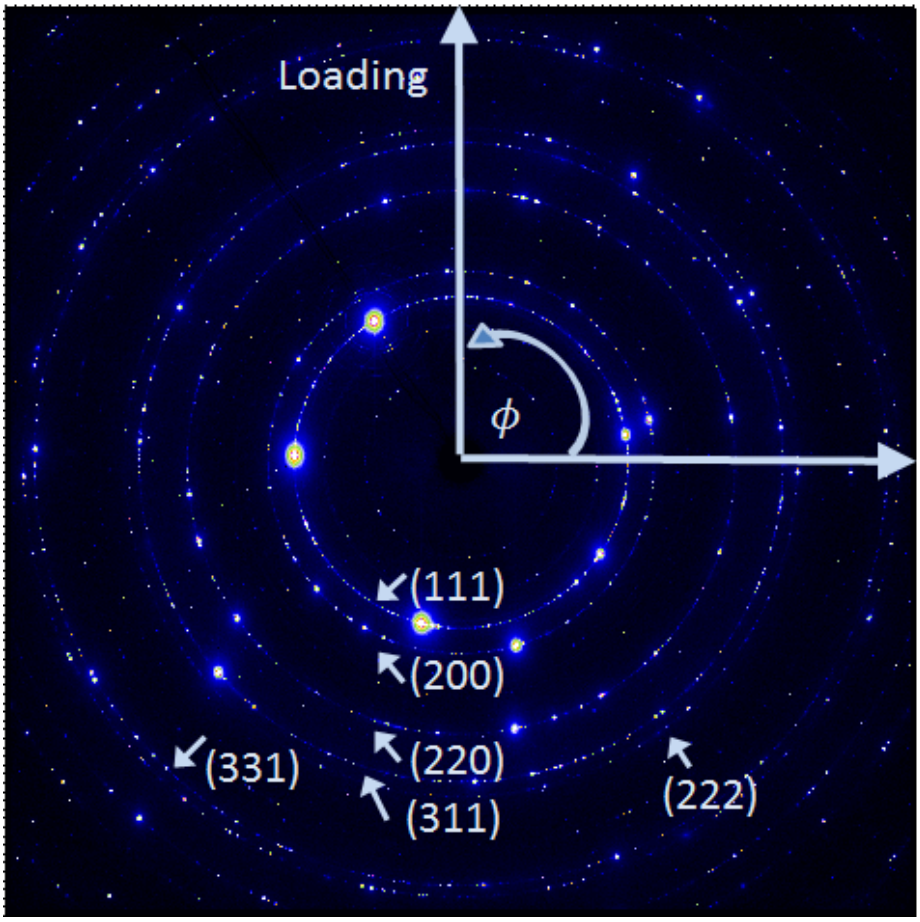

Figure 3-14 A typical 2D diffraction pattern collected away from notch on the pre-fatigued sample at zero load. The corresponding (hkl) peaks are labeled. The tensile loads were applied in the y-direction (vertical direction, also denoted as loading direction), and the azimuthal angle is defined as 90˚ in y-axis, and 0˚ in x-axis.

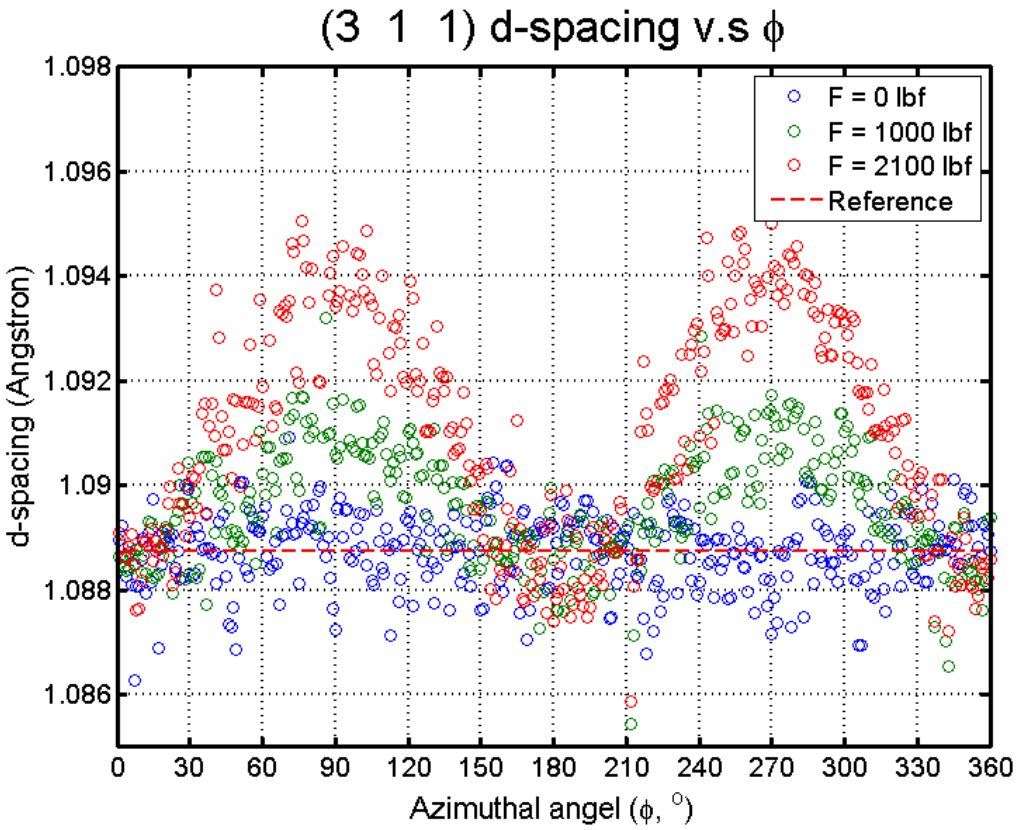

Figure 3-15 An example of (3 1 1) lattice spacing vs. azimuthal angle under three loading conditions, 0 lbf, 1000 lbf, and 2100lbf.

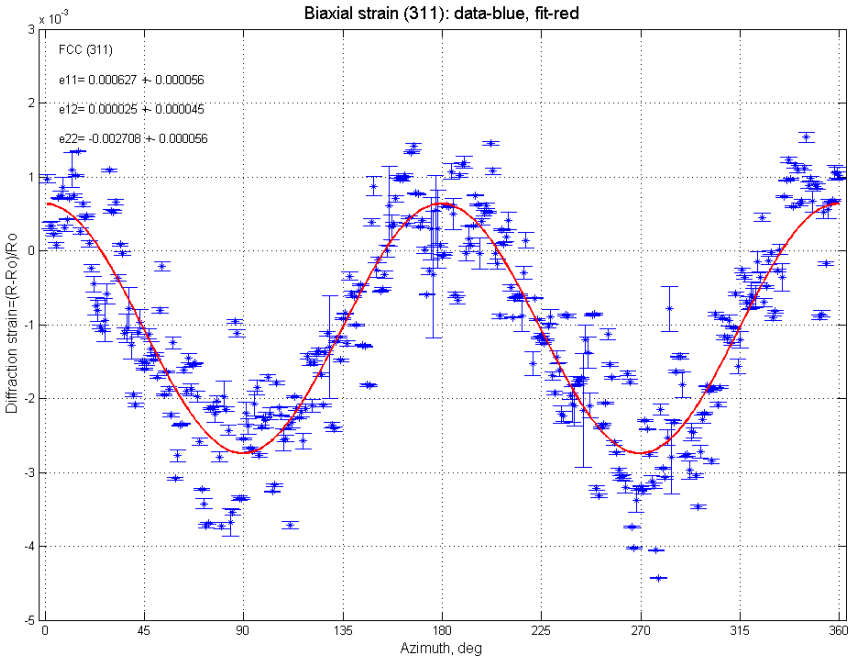

Figure 3-16 An example of least-square fitting of lattice strain vs. azimuthal angle. The observed strains from one or a few grains are in blue, and the fitted curve is in red. The fitting rectifies local strain variation due to inter-granular stress

4 CHAPTER IV

RESULTS

4.1 Deformation of BMG

The intensity vs. Q curve, I(Q), of the sample in loading direction under various uniaxial tensile stress is shown in Figure 4-1. The curves were obtained by integrating 5 degrees in azimuthal angles from the 2D-diffraction image. The inset is the local magnification of the top part of the first peaks, showing that the peak positions change with stress in the tensile directions. The figure clearly show that the increasing tensile stress causes the peaks in I(Q) to move to smaller q values in the loading direction and while to higher q values in the transverse, indicating the enlargement of distance between atoms in the loading direction and contraction in the transverse simultaneously. The shift of peak position in I(Q) under tensile stress is nearly linear. The corresponding structure function, S(Q), for each stress level were obtained using PDFgetX2 software. The $l = 0$ term and $l = 2$ of S(Q) were calculated through equation 2.12. In Figure 4-2, the isotropic ($l = 0$) component of S(Q), $S_0^0(Q)$, shows little changes with the applied stress, but, the elliptical ($l = 2$) component, $S_2^0(Q)$, shows significant changes as a function of applied stress. The amplitude of $S_2^0(Q)$ is roughly proportional to the stress, whereas the shape is almost independent of the stress. The elliptical ($l = 2$) component of the PDF, $g_2^0(r)$, was obtained by the spherical Bessel transformation, Eq.2.13, and is shown in Figure 4-3. The

$g^0_{2,obs}(r)$ is roughly proportional to the stress in amplitude, while the shape remains almost unchanged, as expected from the behavior of $S^0_2(Q)$.

It can be shown that for axial elongation along loading direction, the elliptical PDF due to affine deformation, $g^0_{2,aff}(r)$, can be expressed in terms of the derivative of the isotropic PDF[67, 68], $g^0_0(r)$

$$g^0_{2,aff}(r) = \varepsilon_{zz,aff}\,\overline{g}^0_{2,aff}(r) = -\varepsilon_{zz,aff}\left(\frac{1}{5}\right)^{1/2}\frac{2(1+\nu)}{3}\,r\frac{d}{dr}g^0_0(r) \qquad (4\text{-}1)$$

where ν is the Poisson's ratio. Indeed the experimentally observed $rg^0_{2,obs}(r)$ is close to the derivative as shown in Figure 4-4, particularly at large distances. The amplitude of the apparent elastic strain, ε_{app}, was estimated by matching the experimental $rg^0_{2,obs}(r)$ to $rg^0_{2,aff}(r)$ over the range of r between 6.6 and 25 Å, using the experimental value of ν=0.38, $\varepsilon_{app} = \varepsilon_{aff}$ over this range. The apparent Young's modulus, $\sigma / \varepsilon_{app}$, is 94.5 GPa, close to the value determined by ultrasound resonance method, 89 GPa [69]. The effective Young's modulus determined by diffraction experiments and published by others [28] are close to, but slightly higher than those determined by ultrasound measurements.

However, Figure 4-4 shows small but significant differences between the observed $g^0_2(r)$ and $g^0_{2,aff}(r)$ below 6.6 Å. These differences could be caused by the anelastic events. Earlier studies found that the apparent strain determined by the PDF analysis was not homogeneous, but was dependent on the atomic distance, r [25, 26, 28]. This has been suggested to be the effect of anelasticity [28]. However, in the earlier studies the elastic

and anelastic contributions have not been quantitatively separated. An additional technical complication is that in most papers the strain was assessed from the isotropic PDF. The anisotropic PDF analysis should be utilized for the in-situ tensile test.

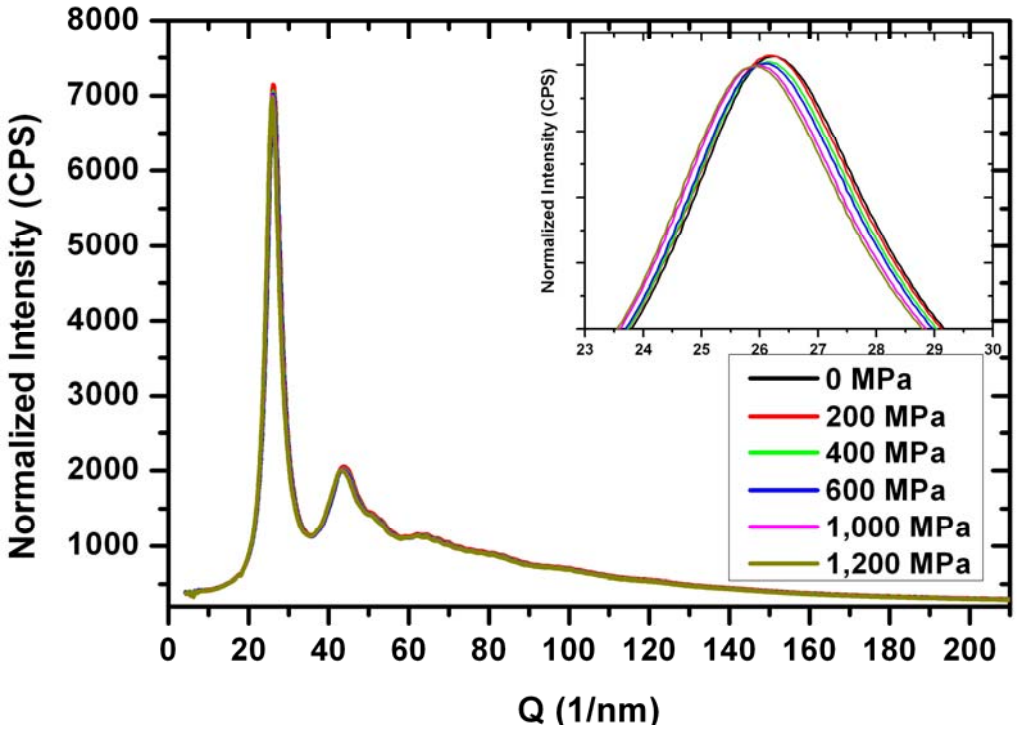

Figure 4-1 The intensity vs. Q curve, I(Q), of the sample in loading direction under various uniaxial tensile stress. The curves were obtained by integrating 5 degrees in azimuthal angles of the 2D-diffraction image in loading direction (90° and 270°)

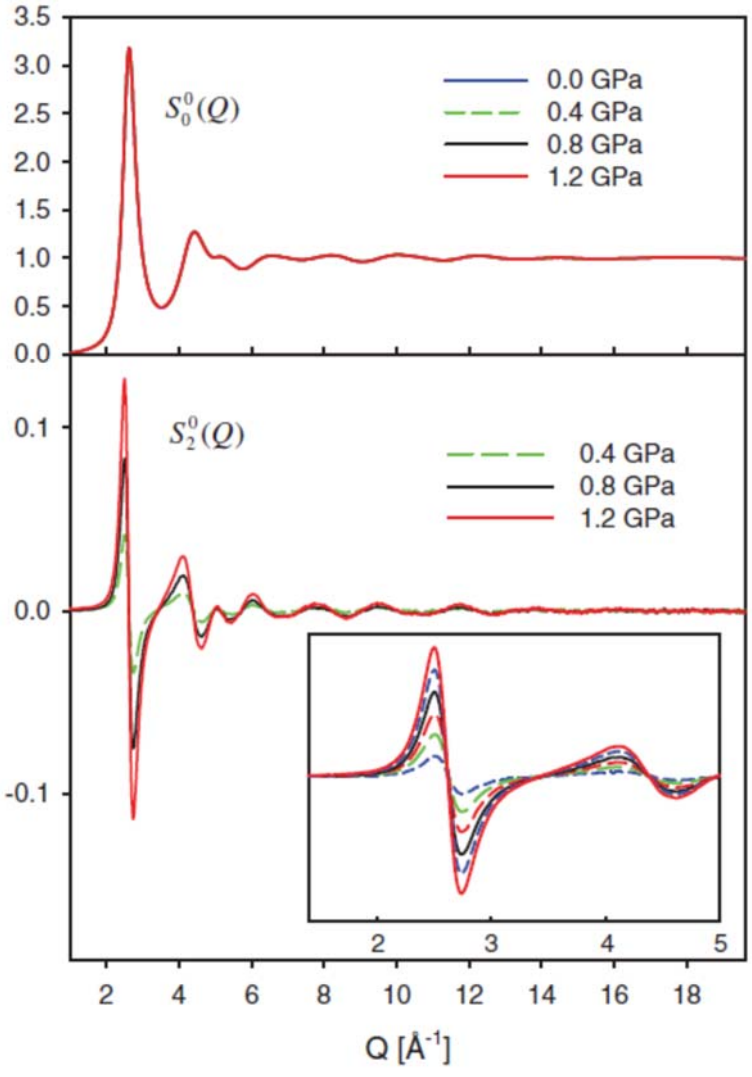

Figure 4-2 The isotropic part of the structure function, $S_0^0(Q)$ (above), and the change in the $l=2$ component of the structure factor, $S_2^0(Q)$ (below). For clarity only three stress levels are shown. The changes appear linear with the stress. The $S_2^0(Q)$ is also shown up to 5 Å in the inset with a stress step of 0.2, from 0.2 to 1.2 GPa[70].

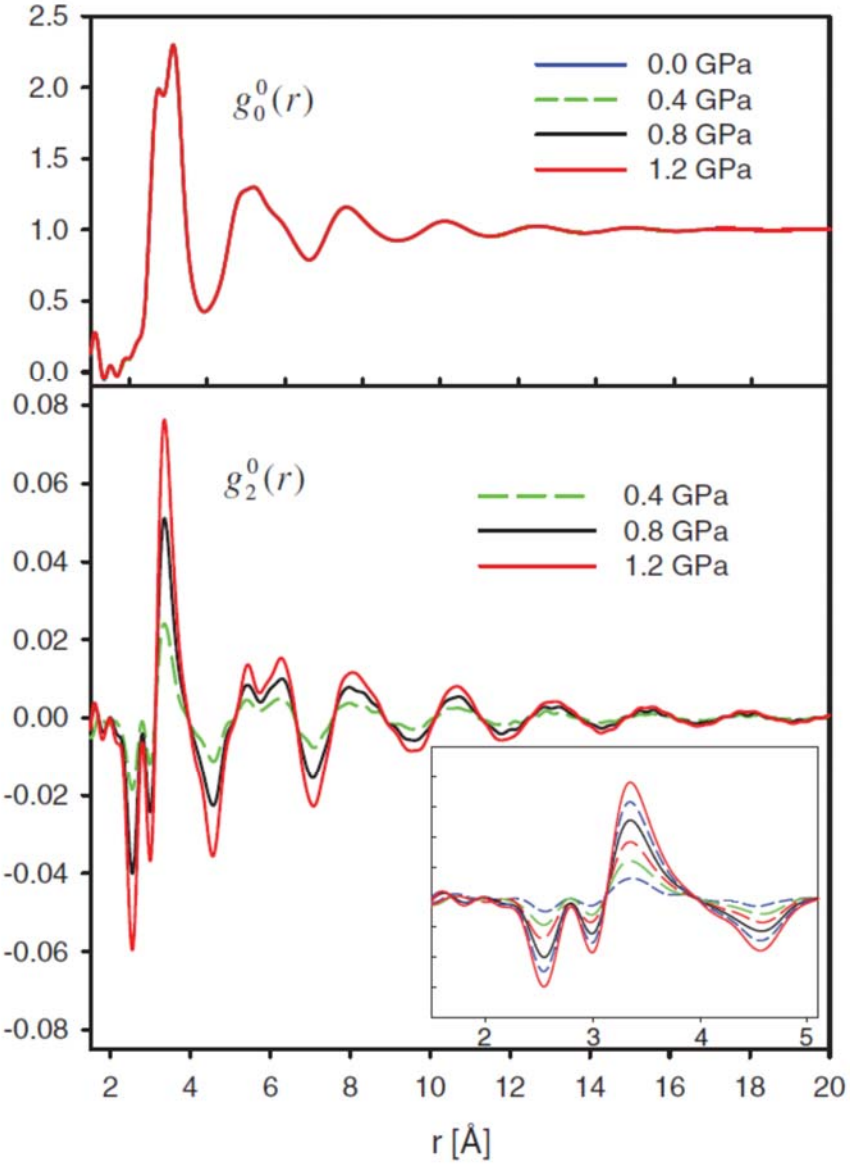

Figure 4-3 The isotropic part of the PDF, $g_0^0(r)$ (above). And the $l=2$, component of PDF, $g_2^0(r)$ (below), For clarity only three stress levels are shown. The amplitude of the anisotropic term is roughly proportional to the stress, whereas the shape remains largely unchanged[70].

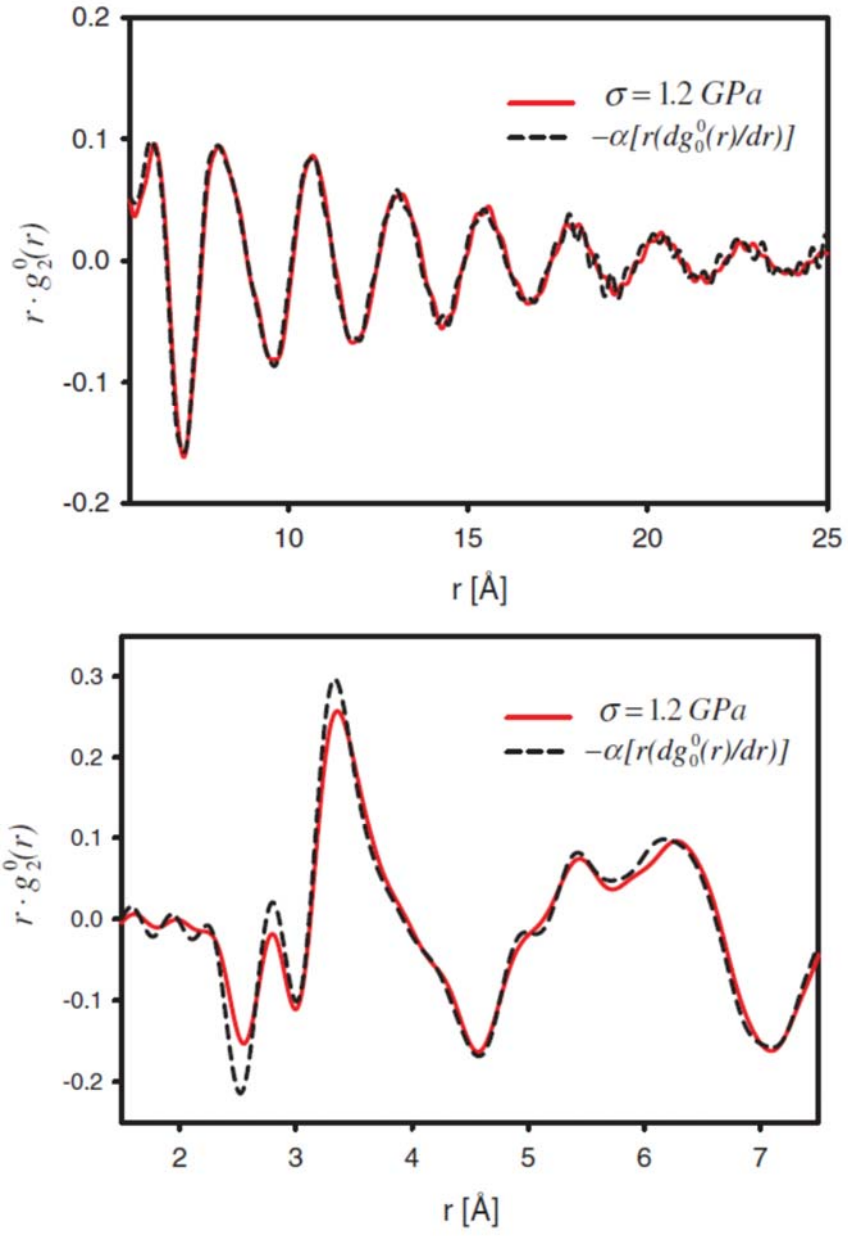

Figure 4-4 The $l = 2$, component of PDF, $g_2^0(r)$, at the applied stress of 1.2 GPa (red), compared to the PDF for affine deformation(black). Here, the $rg_2^0(r)$ is shown to emphasize oscillations at large r. The fit is very good beyond 6.6Å, but obvious deviations are found in the first atomic shell up to 4Å[70].

4.2 Fatigue life under compression-compression loading

Figure 4-5 shows the S-N curve (S: the stress range of the test, and N: the number of cycles to failure) of the as-cast $(Zr_{55}Cu_{30}Ni_5Al_{10})_{98}Er_2$ alloy, and the results of the series of fatigue tests from the current study. The open circle is the fatigue life of the studied material with a fixed L/D ratio of 1.67, and a testing frequency of 10 Hz at various stress ranges (typical fatigue tests). The colored symbols are the data from this study (a larger L/D ratio). The red color denotes the first-cycle tests (as-cast samples), and the blue color represents the proceeding tests using the left-over from the first fatigue test. The cycles-to-failure of each test was counted individually, the fatigue-life of 2^{nd}-run and 3^{rd}-run tests excluded the prior fatigue history. The first-cycle tests of the specimens show similar fatigue life (Figure 4 and Table I). For the second-cycle tests (open circle), it is seen that the fatigue life is comparable or longer when compared with the 1^{st}-cycle test (as-cast). To clearly show these results, we plot the fatigue data separately in Figure 4-6(a), and the detailed data are summarized in Table 4-1.

Many factors, such as the frequency of the test and the geometry of the specimen, will affect the fatigue behavior of BMGs [47]. Since the same sample is used for several runs of the tests, the sample will inevitably become progressively smaller. The changes of L/D ratios might affect the fatigue life of a specimen. We plot the fatigue life of each test as a function of L/D ratio in Figure 4-6(b). The results do not show strong correlation between the L/D ratio and the fatigue life within the range from approximately 0.8 to 4. Therefore, the dominant factor that affects the fatigue life of a specimen in this experiment could be related to cyclic loading.

Table 4-1 The table of fatigue data in Figure 4-6.

	1st As-cast		2nd Fatigued	
	cycle to failure	L/D	cycle to failure	L/D
A	1,535,442	4.17	1,269,216	0.82
			3,003,711	1.58
B	304,354	4.15	2,100,754	1.83
			4,639,253	1.4
C	1,315,717	4.15	1,703,792	2.92

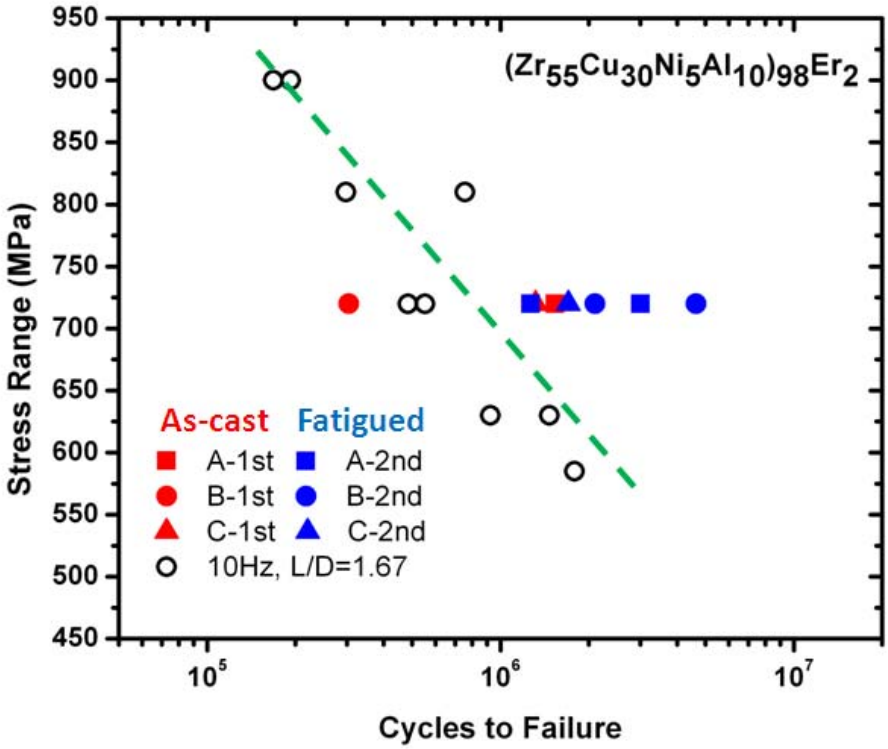

Figure 4-5 The stress-range versus number of cycles to failure (S-N curve) data of $(Zr_{55}Cu_{30}Ni_5Al_{10})_{98}Er_2$ BMGs. The open circle is the fatigue life of the same material with a fixed L/D ratio (L/D = 1.67), and a frequency of 10 Hz at various stress ranges. The colored symbols are the data from this study.

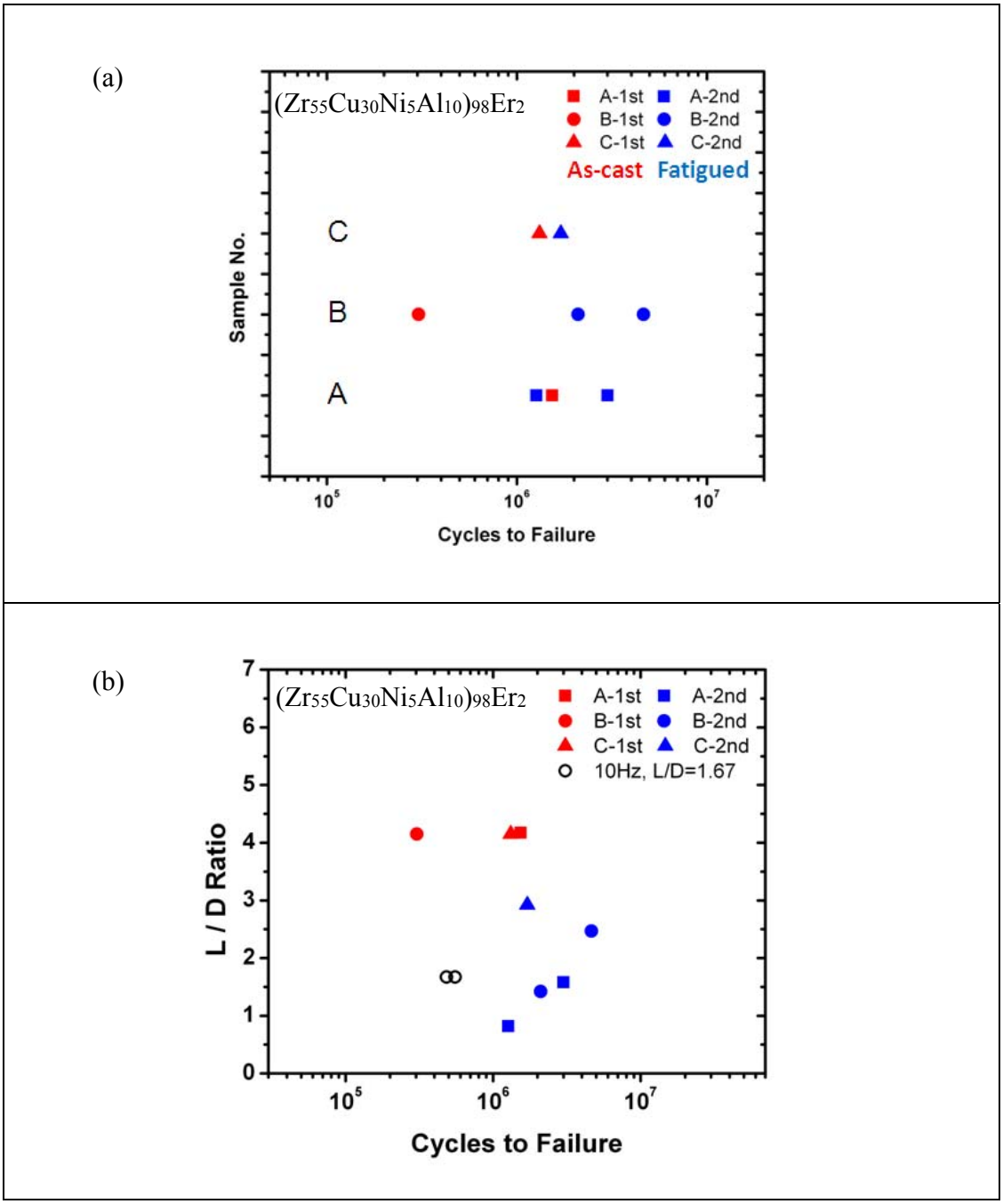

Figure 4-6 (a) The fatigue life of samples, A, B, and C. The 1st-run (in the as-cast condition) data is shown in red, and the 2nd run data is presented in blue. The number of cycles-to-failure of the 2nd-run test starts from zero, and does not include the cycles made in the 1st-

run test. The fatigue life of the "pre-fatigued" sample (left-over) is equal or longer, compared to the as-cast sample. The results suggest that the fatigue damage in the specimen is mainly localized, and the cyclic loading has no globalized effect on the sample. When the fractured part is removed, the rest of the material acts just like an as-cast material. (b) The number of cycles to failure as a function of the L/D ratio of the specimen. The results showed no correlation between the L/D ratio and the fatigue life.

4.3 Fracture surface of fatigued BMGs

To further identify the failure mechanism of the fatigue tests, we examine the fracture surface by scanning-electron-microscopy (SEM). Figure 4-7 presents the surface morphology of the fracture specimen. A characteristic vein-like pattern, as shown in Figure 4-7 (a) and the left side of Figure 4-7 (c), is observed on fracture surfaces. This pattern is commonly found on the fracture surface of BMGs under tension or compression tests [38, 40]. These features are believed to be formed during the final stage (fast fracture) of the fatigue fracture, when the stress on the remaining load-carrying cross-section of the sample reaches the load limit of the material, and the spread of fracture becomes catastrophic. Then the material on the shearing plane becomes melted due to the heat generated during the fracture process at the fast fracture stage. Striations, as shown in Figure 4-7 (b) and (c), could be found only on a small portion of the fracture surface. Figure 4-7 (b) is the enlarged view of the rectangle in Figure 4-7 (c). A molten droplet covers part of the striation. The striation spacing is ~ 190 nm. It is surprising to observe striations during the fatigue failure of BMGs under cyclic compression-compression loadings. These are commonly seen on the fatigue tests under bending conditions. The striations have not been reported before for Zr-based BMGs under cyclic compression- compression fatigue (although previous studies usually used samples with smaller diameters (< 3 mm in diameter). We could not locate the crack-initiation sites on the fracture surface, since they were destroyed by the surface melting due to severe shearing at the final stage of the fatigue failure.

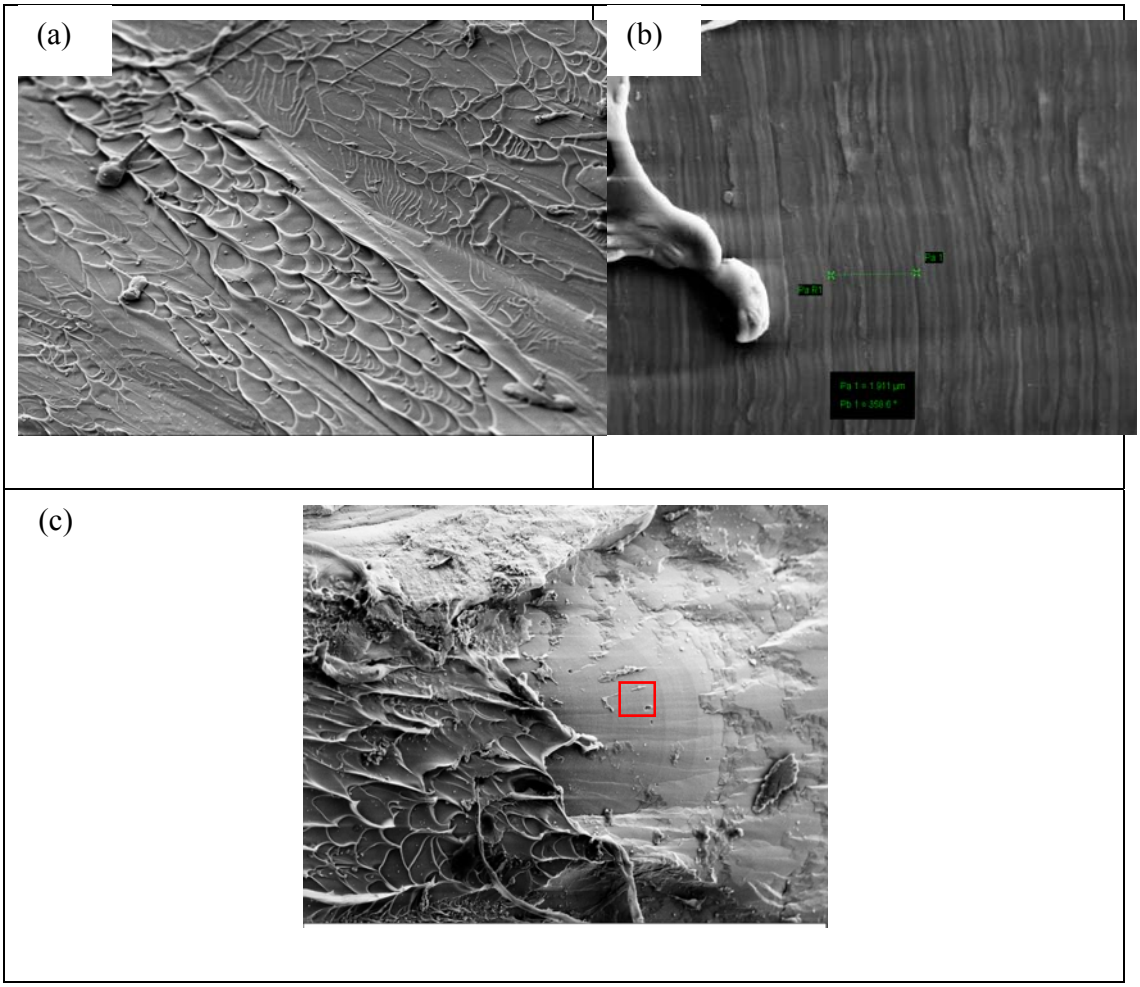

Figure 4-7 SEM pictures of the fracture surface. (a) A vein pattern can be found on the fracture surface. The feature is the same as the one typically found on the fracture surface of the sample under monotonic compression. [38, 40] (b) Striations were found on the fracture surface. It is believed to be in the slow, crack-propagation region. The striation spacing is 190 nm. (c) The possible crack-initiation site was destroyed by the surface melting due to the severe shearing at the final stage (fast fracture) of the fatigue fracture. The sample broke into several pieces at the end, the crack initiation sites cannot be found.

4.4 PDF analyses of fatigued BMGs

Figure 4-8 is the high-energy X-ray scattering spectrum of the as-cast, and two fatigued (2nd run) $(Zr_{55}Cu_{30}Ni_5Al_{10})_{98}Er_2$ alloys. The intensity, I(Q), versus Q (a wave vector) of three samples show identical features without the sign of crystalline phases. This result indicates that the specimens before and after the fatigue tests are in an amorphous state, without any major structure changes (phase transformations). We obtained the PDF shown in Figure 4-9 by the Fourier transformation of the structure function, S(Q), to study the local atomic structure of the amorphous samples. We compare the G(r) of an as-cast sample to that of the fatigued samples. The differences between as-cast and fatigued samples are very small (We only show G(r) of sample B in Figure 4-9 for comparison). The results suggest that there is no significant changes on the atomic structure of the BMG in the medium-range (>10 Å) region, but only small differences in the short-range (< 5 Å) region. Since the changes in the short-range region are rather small (less than ~ 0.6%), we used a standard statistical tool, the two-way analysis of variance; to test whether this differences is significant. We tested the $\Delta G(r)$ (in Figure 4-9) and the first derivative of $\Delta G(r)$ of the same sample measured at different instruments. The statistical analysis showed that the differences are not significant.

We compared I(Q) between the center region and the near-fracture-surface section of the sample. No significant differences can be observed in both I(Q) and G(r). With the measurement geometry used in Figure 3-6(c), we could compare the diffraction anisotropy of the samples after fatigue tests. To reveal the diffraction anisotropy, we subtract the I(Q) in the horizontal direction (transverse direction) from the I(Q) in the vertical direction

(loading direction). The result in Figure 4-10 showed that the diffraction anisotropy can only be observed near the fracture-surface region, and the magnitude is small (< 0.6%); while in the bulk region, the structure of the sample is still isotropic. This anisotropic behavior is likely caused by severe shearing in the fast-fracture stage, the last stage of the fatigue failure of the BMG, not the cyclic loading itself.

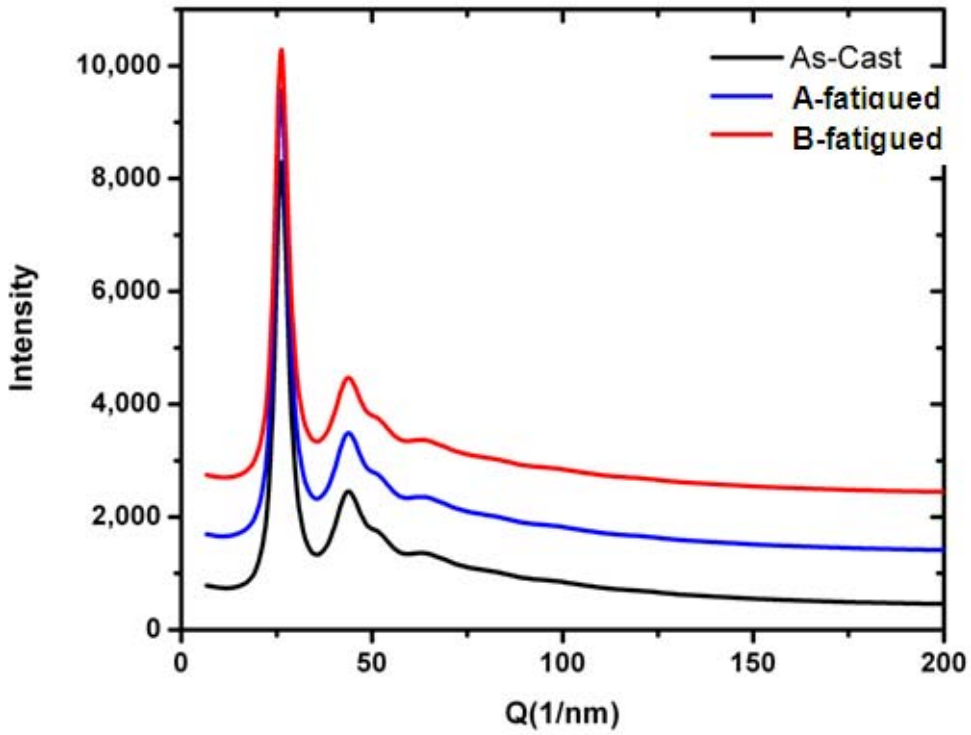

Figure 4-8 The high-energy synchrotron X-ray scattering of the as-cast, fatigued (2nd run) $(Zr_{55}Cu_{30}Ni_5Al_{10})_{98}Er_2$ alloys. The I(Q) shows identical features without the sign of crystalline phases. The specimens before and after the fatigue test are all in an amorphous state.

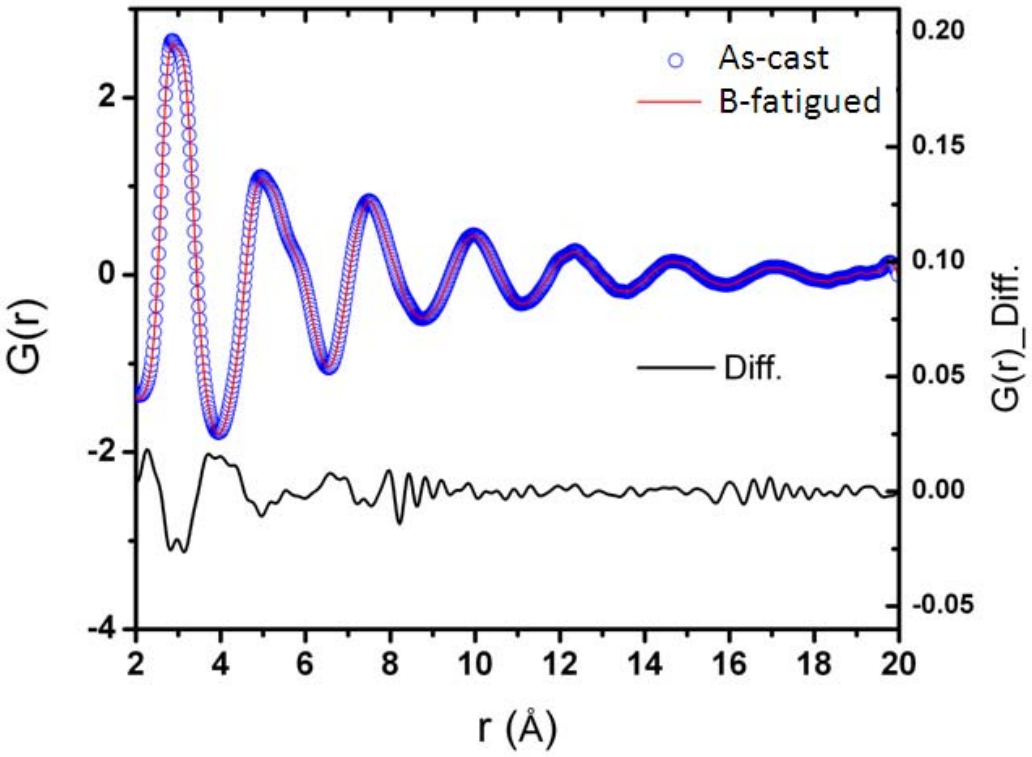

Figure 4-9 Reduced pair-distribution functions of the as-cast and fatigued samples. No significant changes between the as-cast and fatigued samples were found, but we do observe small differences in the short-range-order part (within 8 Å).

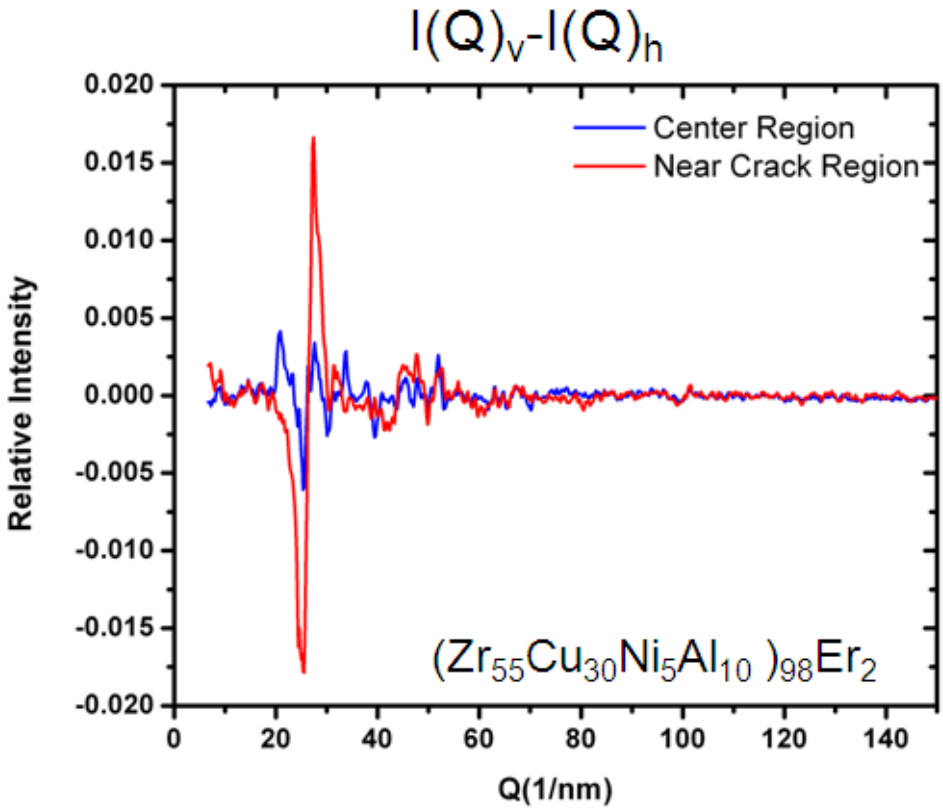

Figure 4-10 A very small but notable diffraction anisotropy, found at the fracture-surface region. It might result from severe plastic deformation inside the shearing plane at the final stage of the failure (fast cracking).

4.5 Determination of single crystal elastic constants by HE-XRD

Single crystal elastic constants are intrinsic material properties correlated with material response to applied load. Also, they are key input parameters for a variety of simulations on both single crystal and polycrystalline materials' deformation behavior, in particular when grain level stress-strain response is considered. Determination of single crystal elastic constants for a polycrystalline material is nontrivial, because of the difficulties in fabricating single crystals with exactly the same composition as polycrystalline material, necessary size, purity, microstructure, and shape, for elastic constant measurements by either ultrasonic methods or tensile tests. In fact, single crystal elastic constants are usually not available for many multicomponent alloy systems. The available single crystal elastic constants at elevated temperatures are even rare.

4.5.1 deWit's method

An alternative approach to obtain single crystal elastic constants by high-energy X-ray diffraction of polycrystalline materials is described below. This approach is to measure lattice spacing of a set of reflections (hkls) as a function of load, which can be performed in-situ at elevated temperatures at a synchrotron source. The use of high-energy X-rays (say 70keV) allows collecting diffraction data in transmission mode from bulk specimen of a few mm in thickness. By using a large area detector, multiple reflection rings can be recorded simultaneously, and lattice strains along and perpendicular to the loading direction can be determined from a single measurement. Like typical powder diffraction measurement, only those grains within the probing volume satisfying Bragg condition will diffract.

The diffraction elastic constants $S_1(hkl)$ and $S_2(hkl)$ for different hkl orientation, can be experimentally determined in the elastic deformation regime as

$$S_1(hkl) = (\nu_{hkl} / E_{hkl}) \quad (4\text{-}2)$$

$$\frac{1}{2} S_2(hkl) = \left[(1 + \nu_{hkl}) / E_{hkl} \right] \quad (4\text{-}3)$$

where hkl are Miller indices, E_{hkl} and ν_{hkl} are the hkl dependent Young's modulus and Poisson's ratio from experiment, respectively. E_{hkl} and ν_{hkl} are calculated from the linear response of hkl lattice strain in the loading and transverse directions with respect to the macroscopic stress under uniaxial tensile test. Continuum mechanics theories have been developed to derive single crystal elastic constants from the measured diffraction elastic constants of polycrystalline materials. Most models are extended from Kröner model which is based on Eshelby's theory of spherical elastic inclusion in isotropic media. These models consider the elastic anisotropy (the hkl dependent Young's modulus) and inter-granular strain caused by elastic anisotropy, and thus calculate different stress field for individual grain.

In deWit's method, single crystal elastic stiffness (C_{11}, C_{12}, and C_{44}) for cubic symmetry are related to isotropic bulk modulus, K, and isotropic shear modulus, G, as

$$3K = C_{11} + 2C_{12} \quad (4\text{-}4)$$

$$G^3 + \alpha G^2 + \beta G + \gamma = 0 \quad (4\text{-}5)$$

where α, β, γ are coefficients as a function of C_{11}, C_{12}, C_{44}, and elastic anisotropy factor A_{hkl} as

$$\alpha = \frac{3}{8}\left[\left(C_{11}+2C_{12}\right)+4\left(C_{44}+3A_{hkl}\left(\frac{C_{11}-C_{12}}{2}-C_{44}\right)\right)\right]-\frac{1}{5}\left(C_{11}-C_{12}+3C_{44}\right) \quad (4\text{-}6)$$

$$\beta = \frac{\left(C_{11}+2C_{12}\right)}{4}\left[C_{44}+3A_{hkl}\left(\frac{C_{11}-C_{12}}{2}-C_{44}\right)\right] - \frac{3}{40}\left[\left(C_{11}+2C_{12}\right)\left(C_{11}-C_{12}\right)+3C_{44}\left(C_{11}+2C_{12}\right)+10C_{44}\left(C_{11}-C_{12}\right)\right] \quad (4\text{-}7)$$

$$\gamma = \frac{-\left(C_{11}+2C_{12}\right)C_{44}\left(C_{11}-C_{12}\right)}{8} \quad (4\text{-}8)$$

$$A_{hkl} = \frac{h^2k^2+l^2k^2+h^2l^2}{\left(h^2+l^2+k^2\right)} \quad (4\text{-}9)$$

Diffraction elastic constants can be calculated from K and G as

$$S_1(hkl) = \left(1/9K\right)-\left(1/6G\right) \quad (4\text{-}10)$$

$$\frac{1}{2}S_2(hkl) = \left(1/2G\right) \quad (4\text{-}11)$$

Based on deWit's method, Thomas et al. [1] proposed the least square fitting approach to derive C_{11}, C_{12}, and C_{44} from S_1(hkl) and S_2(hkl) by minimizing the difference between measured and calculated diffraction elastic constants as

$$\chi^2 = \sum_{i=1}^{n}\left\{\left[\frac{\frac{1}{2}S_2(hkl)_{measure}-\frac{1}{2}S_2(hkl)_{calc}}{\sigma\left(\frac{1}{2}S_2(hkl)_{measure}\right)}\right]^2+\left[\frac{S_1(hkl)_{measure}-S_1(hkl)_{calc}}{\sigma\left(S_1(hkl)_{measure}\right)}\right]^2\right\} \rightarrow \min \quad (4\text{-}12)$$

where $\sigma\left(\frac{1}{2}S_2(hkl)_{measure}\right)$ and $\sigma\left(S_1(hkl)_{measure}\right)$ are standard errors for diffraction elastic constants obtained from experiment.

4.5.2 X-ray elastic constant of the specimen

Based on de-Wit's method and least square fitting approach[71], diffraction elastic constants are calculated with the initial input of single crystal stiffness. The calculated values are fitted to the measured values using least-square refinement described from Eq. (4-4) to (4-12), which generates refined values of single crystal stiffness. The method applies to materials with cubic crystal symmetry and assumes that the polycrystalline material is texture free, which indeed is the case for our samples. However, similar theory has been extended to incorporate texture and accommodate other crystal symmetry into the calculation [72, 73]. The accuracy of results depends on the number of grains detected in the volume of X-ray beam and number of independent hkl orientations. The fitting includes 5 independent hkl orientations ranging from the most compliant orientation (2 0 0) to the stiffest orientation (1 1 1). Therefore, the results provide a good estimation of single crystal elastic constants. It has been found that the final fitting results are not sensitive to the initial input value of single crystal stiffness.

Figure 4-11 shows reciprocal of hkl dependent Young's modulus derived from the diffraction measurement of polycrystalline specimen as a function of elastic anisotropy factor A_{hkl}. In single crystal with cubic crystal symmetry, the Young's modulus is governed by hkl crystal orientation as

$$\frac{1}{E_{hkl}} = \frac{C_{11} + C_{12}}{(C_{11} + 2C_{12})(C_{11} - C_{12})} - 2\left(\frac{1}{C_{11} - C_{12}} - \frac{1}{2C_{44}}\right)A_{hkl} \qquad (4\text{-}13)$$

The elastic anisotropy factors for different hkl planes are listed in Table 4-2. In Figure 4-12, a good linear trend is evident for both first cycle and fatigue 75% samples, which is an additional support for the appropriateness of using DeWit's methodology to derive single crystal elastic constants.

The calculated and measured E_{hkl} for (1 1 1), (2 0 0), (2 2 0), (3 1 1), and (3 3 1) orientations are listed in Table 4-2, which compare favorably. The fitted single crystal stiffness for the material is presented in Table 4-3. Literature values of single crystal stiffness for other Ni-based superalloy [74, 75] are plotted together for comparison. The results for both samples are similar to each other, and show agreement with the published values of other Ni-based superalloys detected through ultrasonic methods or tensile tests. This similarity between two samples may be expected as fatigue induced deformation should not change the elastic response of the material to external load. C_{12} of the specimen is slightly higher than other Ni-based superalloys and C_{44} is slightly lower.

The calculated stress-lattice strain responses from the fitted C_{11}, C_{12}, and C_{44} along with measured values are plotted in Figure 4-12 for the first cycle and fatigue 75% samples. The measured data lie perfectly on the calculated linear lines, demonstrating the reliability of the results. The 95% confidence intervals for the fitted C_{11}, C_{12}, and C_{44} are (192, 263), (125, 197), (98, 114), respectively.

Table 4-2 Values of hkl-specific Poisson's Ratio for pure Ni (extracted from Ref.[76]) and elastic anisotropy factor A_{hkl} for measured hkl orientations. Measured and fitted E_{hkl} are also listed for the 75%-fatigued sample, in the unit of GPa.

	(111)	(200)	(220)	(311)	(331)
ν_{hkl}	0.28	0.40	0.33	0.36	0.32
A_{hkl}	0.333	0.000	0.250	0.157	0.274
Measured E_{hkl}, fatigue 75% sample	205	141	198	175	220
Fitted E_{hkl}, fatigue 75% sample	227	137	200.0	175	208

Table 4-3 Calculated single crystal elastic constants from first cycle and fatigue 75% samples at 752°F, compared with elastic constants of other Ni-based superalloys measured by ultrasonic techniques at the same temperature [74, 75]. All elastic moduli are given in units of GPa.

Elastic Constants	Present work: As-cast	Present work: 75%-fatigued	CMSX-3 [74]	TMS-26 [75]
C_{11}	241	233	230	238
C_{12}	169	167	150	152
C_{44}	105	111	115	120

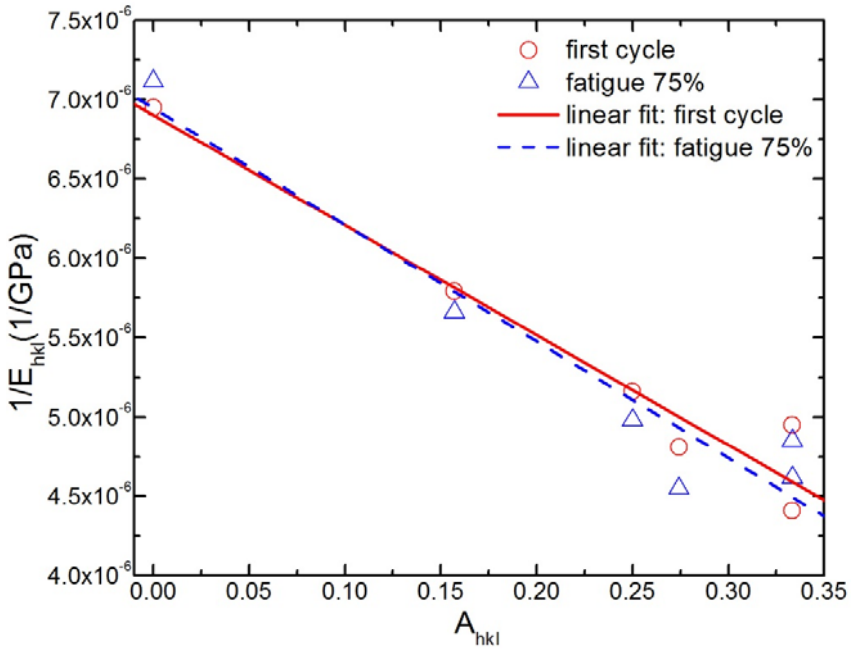

Figure 4-11 The measured reciprocal of hkl dependent Young's modulus in the polycrystalline sample as a function of elastic anisotropy factor A_{hkl}.

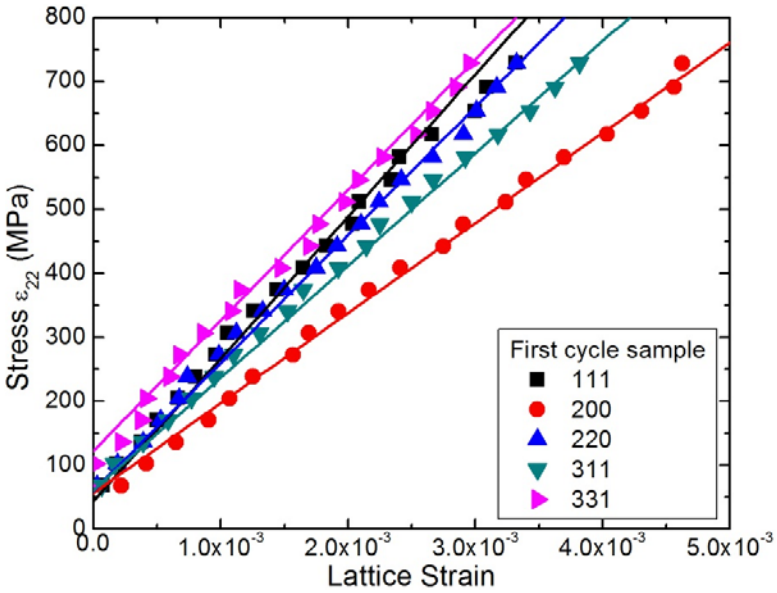

(a)

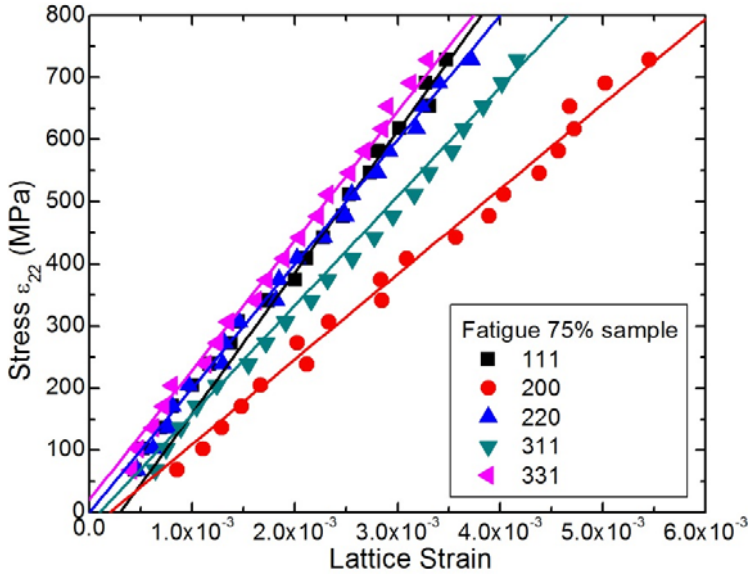

(b)

Figure 4-12 Measured lattice strain (scatters) as a function of local axial stress ε_{22} (FEM simulated), plotted together with stress-lattice strain response (lines) calculated from fitted C_{11}, C_{12}, and C_{44}, for (a) first cycle sample and (b) fatigue 75% sample.

4.6 Evolution of lattice strain during loading and unloading

We first examine the lattice strains near and away from the notch of a heavily fatigued specimen. Before the load is applied, the evolution of lattice strain as a function of applied tensile loading for heavily fatigued specimen is shown in Figure 4-13. The corresponding nominal stress along the notch-notch line for the loading of 2100lbf is 1.16 GPa, which is slightly below the yield stress of the studied material at 400˚C. Since the deformation is in elastic range, at center of the specimen [position-18 as indicated in Figure 3-12(a)], the lattice strain increases linearly with increasing the load as shown in Figure 4-13 (a). The force-strain curve of the same specimen near the notch is presented in Figure 4-13 (b). A substantial compressive residual stress is developed after cyclic loading. The compressive residual stress is believed to be closely related the plastic zone ahead of notch tip. Due to the higher stress intensity factor near notch, the material in these area subjected to a stress that is over the yielding stress of the material although the nominal stress is still below the yield point. Therefore, the plastic deformation is expected to occur, and when the load is removed, a compressive residual stress will be developed. This creates a significant crack closure ahead of notch tip. An easy way to quantify this compressive stress is to use Figure 4-13. The intersection of the force-strain curve in loading direction and in transverse direction gives the residual stress at the measured region. In the case of 75%-fatigued sample, at 0.5 mm ahead of notch [position 2 in Figure 3-12(a)], ~ 700lbf is required to overcome this compressive residual stress. By using this intersection method, and defined the force as recovery force, one can plot the recovery force as a function of distances to notch tip as shown in Figure 4-14. Figure 4-14 shows the comparison of the

samples at different stage of fatigue life, and as a function of distances to notch tip. The "recovery force" within ±200 lbf, labeled in red band, can be considered as unaffected (0 lbf), since it's within the error bar of our calculation. The distributions of recovery force clearly mark the zone of compressive residual stress, this zone extends ~0.7 mm ahead of notch tip. However, the extension of the zone along the notch line cannot differentiate the age of the specimen.

Figure 4-15 is the lattice strain of (311) along notch for samples with different fatigue history at various applied forces. The figure compares (a) 1-cycle sample, (b) 1%-fatigued sample, (c) 10%-fatigued sample, and (d) 75%-fatigued sample. A significant residual strain is developed even after 1-cycle of loading-unloading. The residual strain maximize its value at ~0.25 mm ahead of notch tip. The maximum residual strain for 1-cycle, 1%, 10%, and 75%-fatigued sample are ~2.1×10^{-3}, 2.9×10^{-3}, 2.85×10^{-3}, and 3.2×10^{-3}, respectively. The residual strain builds up rapidly at the beginning of the fatigue process, and keeps stable for the majority of the sample's life before it speed up again at the end of fatigue life.

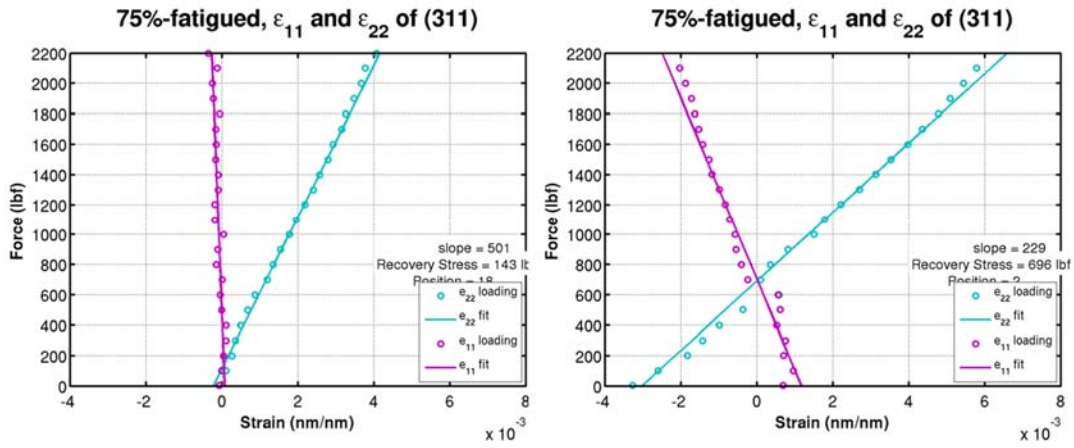

Figure 4-13 The changes of (311) lattice strain as a function of applied force. (a) at the center (3.17 mm ahead of notch tip) and (b) at notch (0.08 mm ahead of notch tip). The lattice strain increase linearly with increasing the load. Because of the compressive residual stress at notch area, the ε_{22} strain at notch without the load is negative (compressive stress). The slope of force-strain curve at notch is smaller than that at the center because the actual stress at notch is higher.

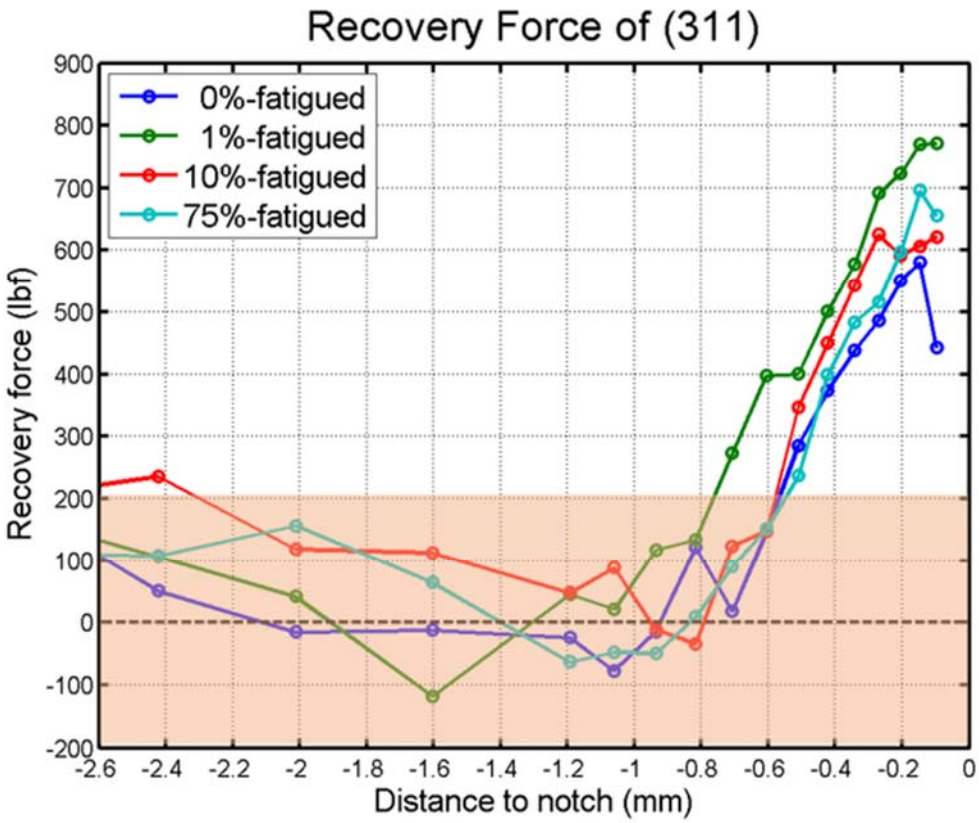

Figure 4-14 The recovery force of (311) as a function of distances to notch tip for samples at different age of its fatigue-life. The "recovery force" within ±200 lbf, labeled in red band, can be considered as unaffected (0 lbf), since it's within the error bar of our calculation. The distributions of recovery force clearly mark the zone of compressive residual stress, this zone extends ~0.7 mm ahead of notch tip. However, the extension of the zone along the notch line cannot differentiate the age of the specimen.

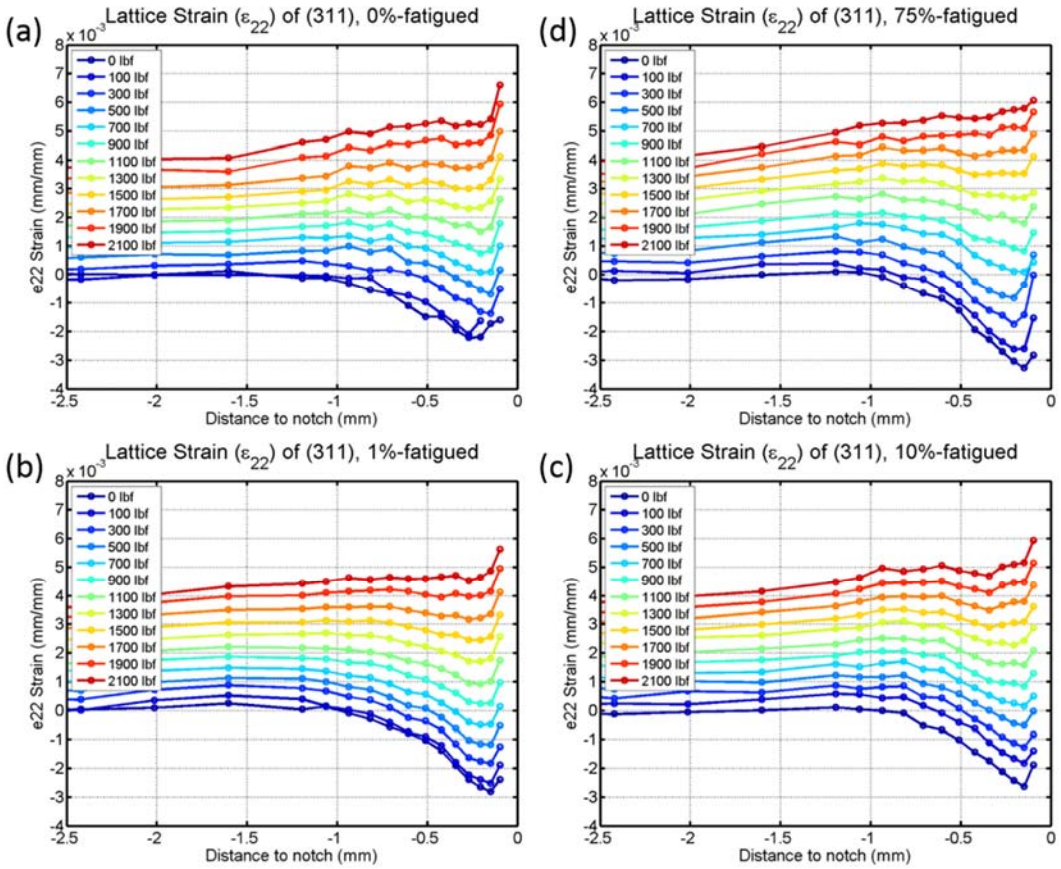

Figure 4-15 Lattice strain of (311) along notch for samples with different fatigue history at various applied forces. (a) 1-cycle sample. (b) 1%-fatigued sample. (c) 10%-fatigued sample. (d) 75%-fatigued sample. A significant residual strain is developed even after 1-cycle of loading-unloading. The residual strain maximize its value at ~0.25 mm ahead of notch tip. The maximum residual strain for 1-cycle, 1%, 10%, and 75%-fatigued sample are ~2.1×10^{-3}, 2.9×10^{-3}, 2.85×10^{-3}, and 3.2×10^{-3}, respectively. The residual strain builds up rapidly at the beginning of the fatigue process, and keeps stable for the majority of the sample's life before it speed up again at the end of fatigue life.

4.7 Strain mapping around notch tip

Previous section shows only the strain evolution alone the notch line, if the whole area around notch is measured, a two-dimensional strain map can be obtained as shown in Figure 4-6. With this 2D strain map, the effect of fatigue can be observed more clearly. Figure 4-6 presents the (311), ϵ_{22} lattice strain maps around notch for virgin (left) and 75%-fatigued (right) samples. Note that ϵ_{22} in the present study is the strain component parallel to the loading direction. The map clearly shows that significant compressive stress/strain is developed after cyclic loading. On the left hand side, where sample has no prior loading history, it shows a flat, featureless map. While on the right hand side, after cyclic-loading for 75% of its life, it shows a compressive strain near notch, and tensile strain a little bit away from tip. The features are consistent with the prediction by finite-element simulation (FEM) analysis.

To further quantify the compressive zone size, we defined a criteria, -0.15% in this case, and calculate the size of the area by a Matlab program. It is found that the size of the compressive zone is small, 0.026 mm^2, for sample with only one cycle of loading, but becomes large, 0.374 mm^2, when it was cyclic-loaded to 75% of the expected life (Figure 4-17). The compressive residual strain ahead of notch tip will grow in terms of size and quantity as fatigue-cycle increases. The comparison of the self-defined zone size at different stages of fatigue life is shown in Figure 4-18. In this figure, the areas are normalized to the size of notch, and it shows the residual stress will build up significantly at the beginning of the fatigue-life, and stabilize before it speed up again at the end of fatigue life. It follows fast-slow-fast pattern similar to da/dN vs dK in crack propagation

experiment. The observation implies that the size of compressive-strain zone can be used as an index to show the remaining life of a specimen. Although the sensitivity may not be very high when the remaining life of a specimen is between 20%~80% of fatigue life.

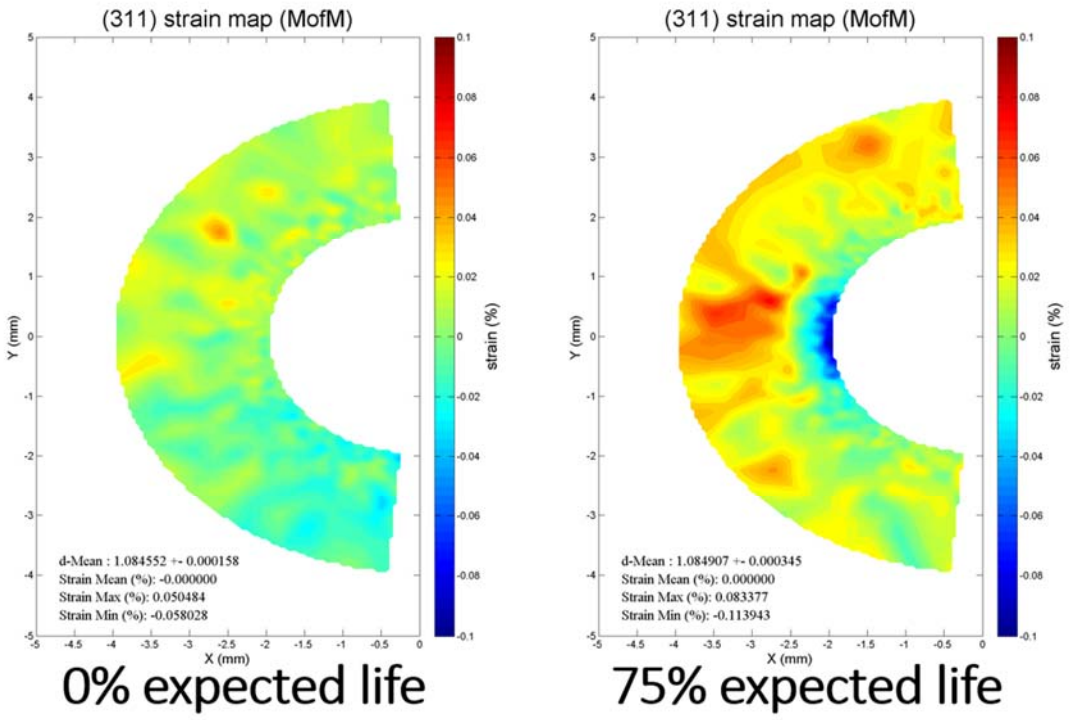

Figure 4-16 (311), ϵ_{22} lattice strain maps around notch for virgin (left) and 75%-fatigued (right) samples. Note that ϵ_{22} in the present study is the strain component parallel to the loading direction.

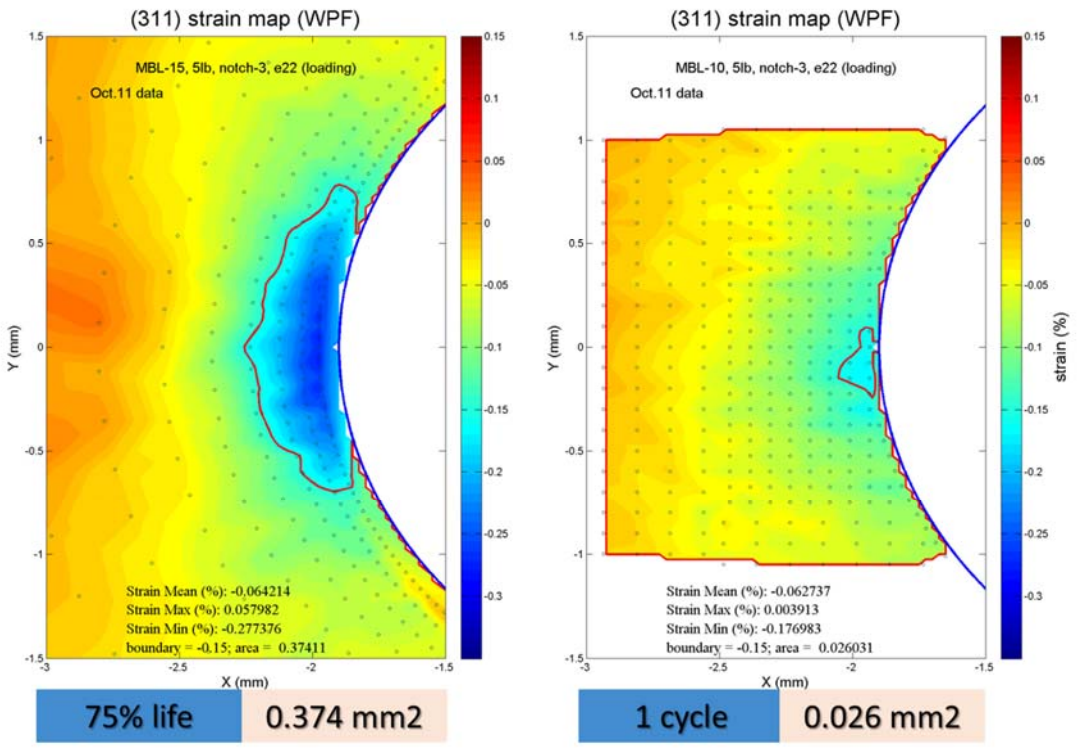

Figure 4-17 The comparison of (311) strain map near notch between (a) 1-cycle-fatigued sample and (b) 75%-fatigued samples. The compressive residual strain ahead of notch tip will grow in terms of size and quantity as fatigue-cycle increases. A criteria of -0.15% is used to illustrate the growth of residual-stress-zone as a function of fatigue life.

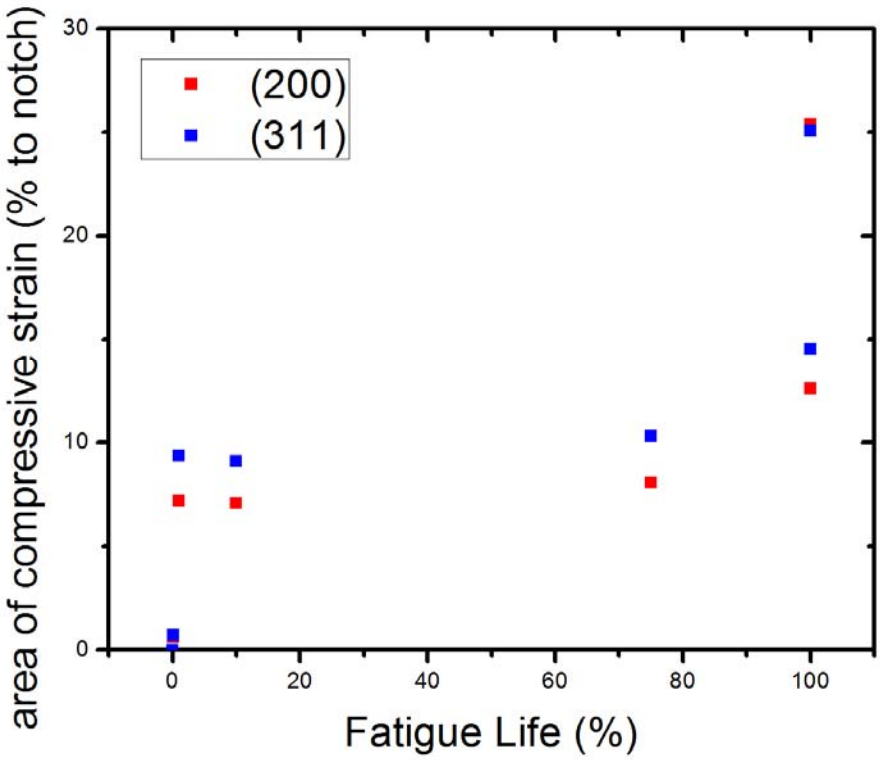

Figure 4-18 The evolution of residual stress zone ahead of notch tip as a function of fatigue life. The areas are normalized to the size of notch. The residual stress will build up significantly at the beginning of the fatigue-life, and stabilize before it speed up again at the end of fatigue life. It follows fast-slow-fast pattern similar to da/dN vs dK in crack propagation experiment.

5 CHAPTER V

DISCUSSION

5.1 Deformation of BMG in macroscopic scale

When a stress is applied to a viscoelastic material, the strain response can be expressed as

$$\varepsilon(\tau_{\exp}) = \varepsilon_{el} + \int_0^{\infty} \varepsilon_{anel}(\tau)[1 - e^{-\tau_{\exp}/\tau}]d\tau \qquad (5\text{-}1)$$

where ε_{el} is the elastic strain, τ_{exp} is the experimental time scale, for instance the inverse of the strain rate, τ is the relaxation time and $\varepsilon_{anel}(\tau)d\tau$ is the anelastic strain with the relaxation between τ and τ+dt. By approximating the exponential function by a step function we obtain

$$\varepsilon(\tau_{\exp}) = \varepsilon_{el} + \int_0^{\tau_{\exp}} \varepsilon_{anel}(\tau)d\tau \qquad (5\text{-}2)$$

Thus all the viscoelastic responses with the response time shorter than the experimental time scale are included in the apparent elastic strain. In order to evaluate the anisotropic PDF due to the anelastic strain, the sample which was creep deformed as described above, at the stress of 1.2 GPa and T = 573 K for 30 min., to obtain the ℓ = 2 PDF, $g^0_{2,anel}(r)$. In Figure 5-1, $g^0_{2,anel}(r)$ is similar to $g^0_{2,aff}(r)$ at large distances. By comparing $g^0_{2,anel}(r)$ to $g^0_{2,aff}(r)$ at large distances, the anelastic creep strain for the particular experiment, ε_{creep}, and obtained $g^0_{2,anel}(r)$, was determined by normalizing $g^0_{2,anel}(r)$ to the anelastic creep

strain of unity. The results showed that the deviations of the anelastic PDF, $g^0_{2,anel}(r)$ from the affine PDF, $g^0_{2,aff}(r)$, are very similar to those for the tensile strain experiment after appropriate scaling. This similarity indicates that the local structural changes due to anelastic strain induced by the apparently elastic deformation are very similar to those due to the anelastic creep deformation, in spite of the differences in time scale and temperature. As discussed previously, the $\ell = 2$ PDF which is due to the anelastic effect is independent of the stress level except for the amplitude, and when normalized by the strain results in the identical $\overline{g}^0_{2,anel}(r)$. Therefore, the total PDF should be fit by

$$g^0_{2,total}(r) = \varepsilon_{zz,anel}\,\overline{g}^0_{2,anel}(r) + (\varepsilon_{app} - \varepsilon_{zz,anel})\,\overline{g}^0_{2,aff}(r) \qquad (5\text{-}3)$$

where $\varepsilon_{zz,anel}$ is the anelastic strain, and $\varepsilon_{zz,aff} = \varepsilon_{app} - \varepsilon_{zz,anel}$ is the affine (elastic) strain.

Figure 5-2 compares the observed $g^0_{2,obs}(r)$ with $g^0_{2,total}(r)$ at $\sigma = 1.2$ GPa. Except for small differences which are most likely due to the mismatch of resolution and noise. The excellent agreement confirms that the strain in this metallic glass includes both the anelastic as well as affine components. The fraction of the affine strain to the total strain, $\gamma = \varepsilon_{zz,aff} / \varepsilon_{app}$, is plotted as a function of the applied stress, σ, in Figure 5-3. The value of γ is nearly constant over this range of stress, and in average 24% of the total strain is anelastic. This result is in excellent agreement with the simulation that suggested that about 20% of the apparent elastic strain is actually an anelastic strain [67]. Many theories, such as the free-volume theory, assume that the defect level is of the order of 1% [21], whereas the defect density suggested by the present results is higher by an order of magnitude. On

the other hand this value agrees very well with the fraction of the frozen liquid-like atoms, 24.3%, in the theory of the glass transition in metallic glasses[77].

The above analysis suggests that the applied load is supported by only 76% of the body, and the rest, the anelastic sites, offer no resistance to load at the time scale of the experiment. Thus, the true elastic constant of the elastic portion can be evaluated as $E_{el}=\sigma/\varepsilon_{zz,aff}$ = 124 GPa. It has been known that the value of the shear modulus of a metallic glass is lower by 20%–30% than calculated for affine deformation [67] and the values for crystalline solids of the same composition. The difference has been attributed to the non-collinear effect [78] and anelasticity [67]. Because the Young's modulus, E, is closely related to the shear modulus, G,

$$E = G\frac{9}{3+G/B} \qquad (5\text{-}4)$$

where B is the bulk modulus, result from current study confirms that the apparent softening of the shear modulus occurs because about a quarter in volume fraction of a metallic glass is anelastic, and does not offer shear rigidity at the experimental time scale.

The results from the in-situ tensile experiment show that about a quarter of the volume of a metallic glass is occupied by anelastic sites, which are soft and bear no static shear load. Consequently, the shear modulus of a metallic glass is lowered by a quarter compared to the instantaneous value. Just as other glasses, metallic glasses are fundamentally viscoelastic, and the volume fraction of the viscous sites is as much as a quarter, not of the order of 1% as in many theories.

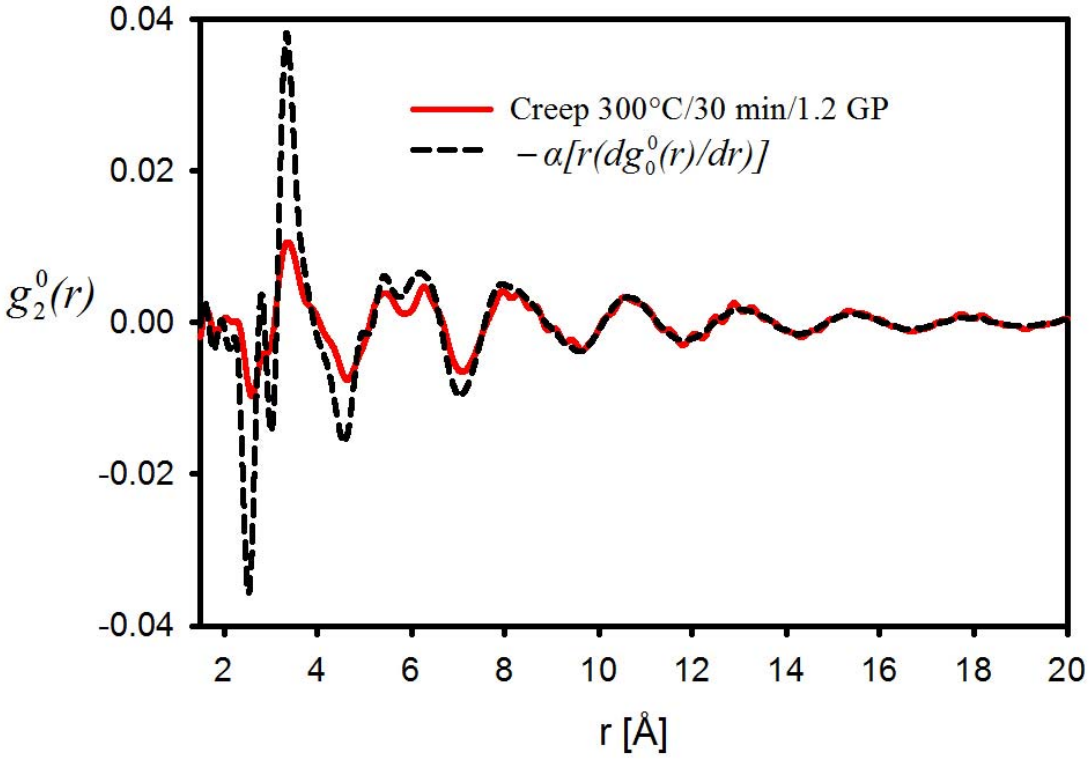

Figure 5-1 The $\ell = 2$ component of the PDF, $g_2^0(r)$, after creep at 574 K for 30 min with the applied load of 1.2 GPa. The dashed line shows the PDF expected for affine (elastic) deformation, which is fitted to the data at large distances. The anelastic strain determined by the fit is 0.4%, whereas the total creep strain is 2%. The difference, 1.6%, is the plastic creep strain.[70]

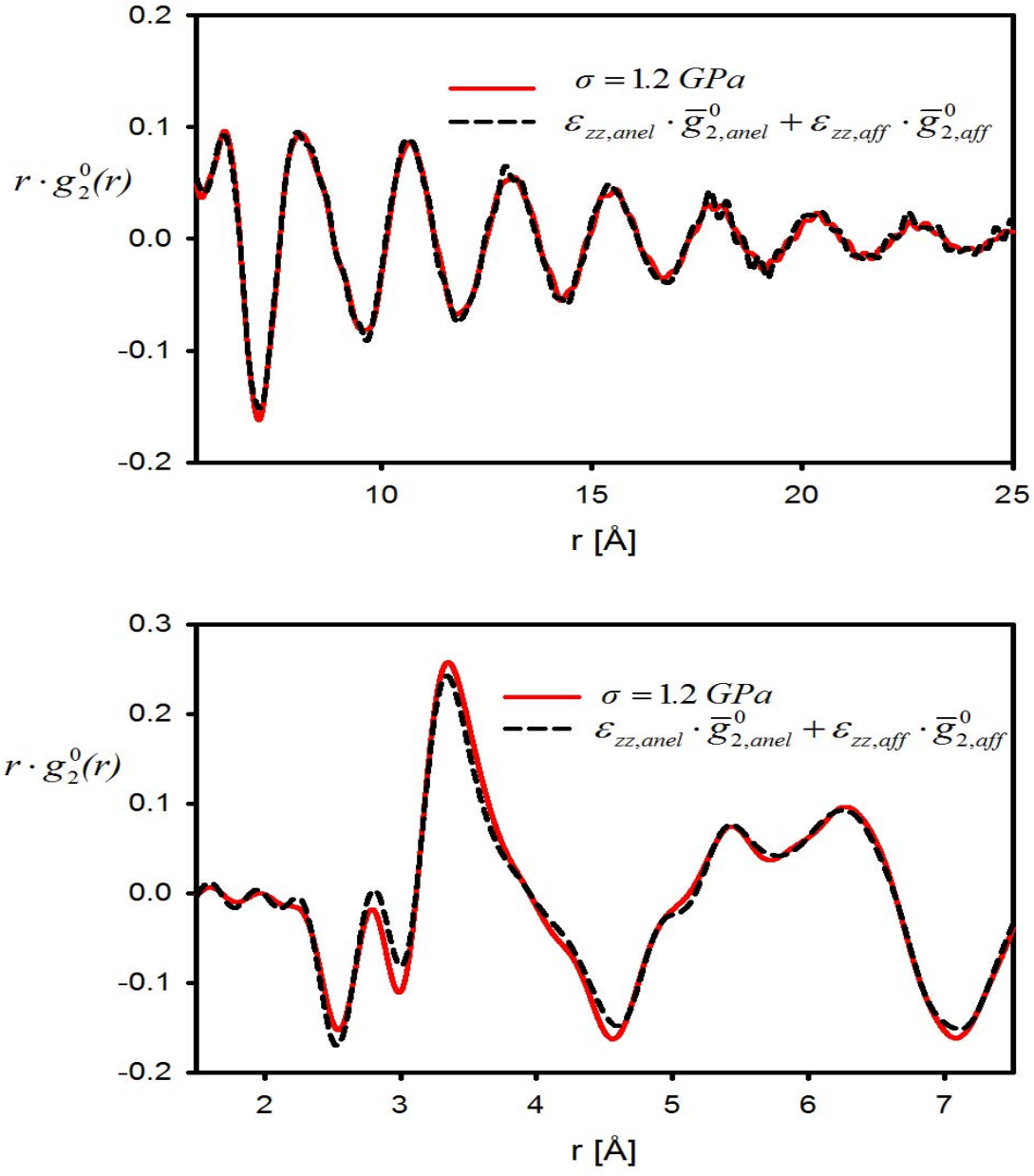

Figure 5-2 The $\ell = 2$ component of the PDF, $g_2^0(r)$, at 1.2 GPa, fitted to the combined PDF for affine (elastic) and creep (anelastic) deformation, Eq. 4.4. The fit shows marked improvement over the one in Figure 4-4[70].

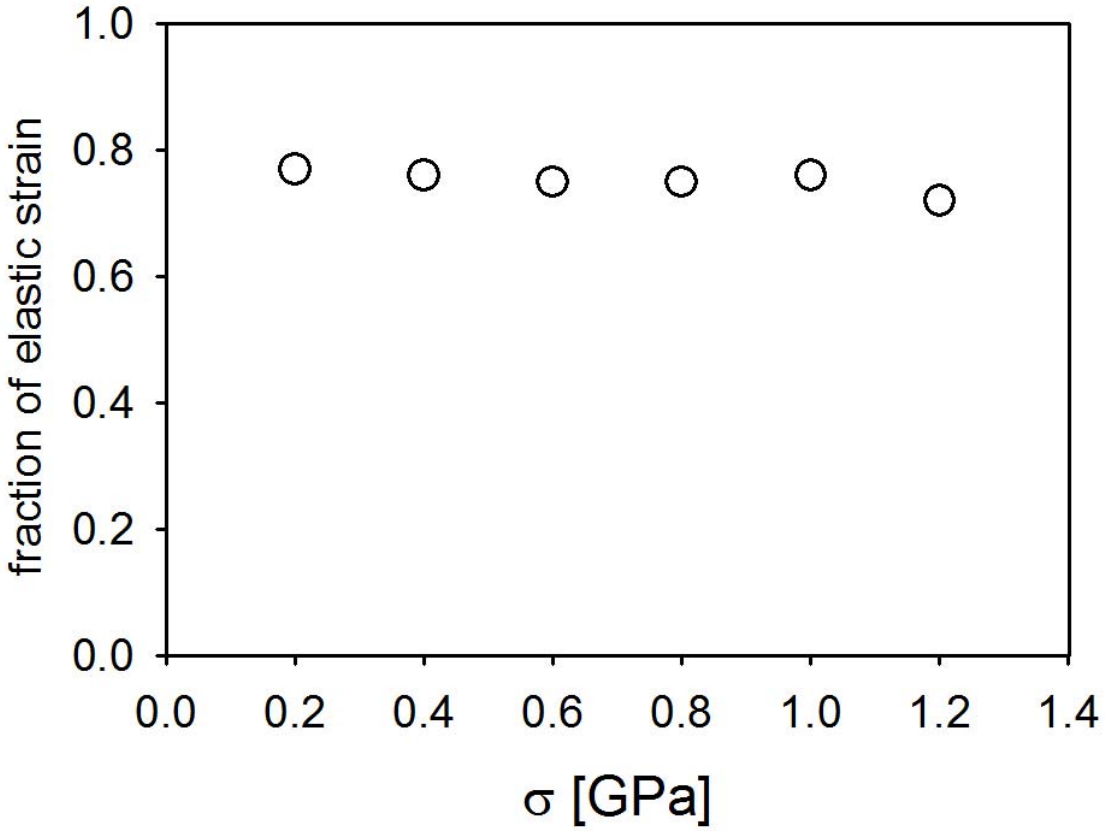

Figure 5-3 The fraction of elastic strain compared to the total apparent strain. It appears constant of applied external stress up to 1 GPa, and on average it is about 76%. The rest, 24%, is the anelastic strain.[70]

5.2 Fatigue fracture of large-diameter BMGs in compression-compression tests

Similar to the samples with smaller diameters, fracture of larger-diameter samples under cyclic compression mostly occurred in a pure shear mode. The major fracture plane formed an angle of ~ 42^{o} with respect to the loading axis [79, 80]. However, unlike the smaller samples in which the major shear plane passes through the whole specimen and separates the specimen into two pieces with a relatively flat shear plane, these larger samples usually broke into two or more pieces, with a convex-shaped major shear plane. This phenomenon could be explained as follow. During the fatigue test, there are many possible shear planes for cracks to form; some of the possible shear planes do not cut through the whole specimen, but start from the end of the specimen as illustrated in Figure 5-4(a). When a shear plane formed from the side surface to the end of the specimen, a small piece of the sample will be removed, as shown in Figure 5-4 (b). Because the sample is large, the stress on the load-carrying cross-section of the sample is still less than the strength of the material. As a result, the fatigue test is carried out on an irregularly-shaped specimen with higher stress levels. The odd shape of the sample creates a fairly complex stress state within the specimen, and further diversifies the final failure mode of the sample. This peculiar mode creates difficulty to identify the failure mechanism of large BMGs specimens under compression-compression fatigue tests, since crack-initiation sites and crack-propagation regions [as shown in Figure 4-7(c)], are destroyed by severe shearing during the final stage of the failure.

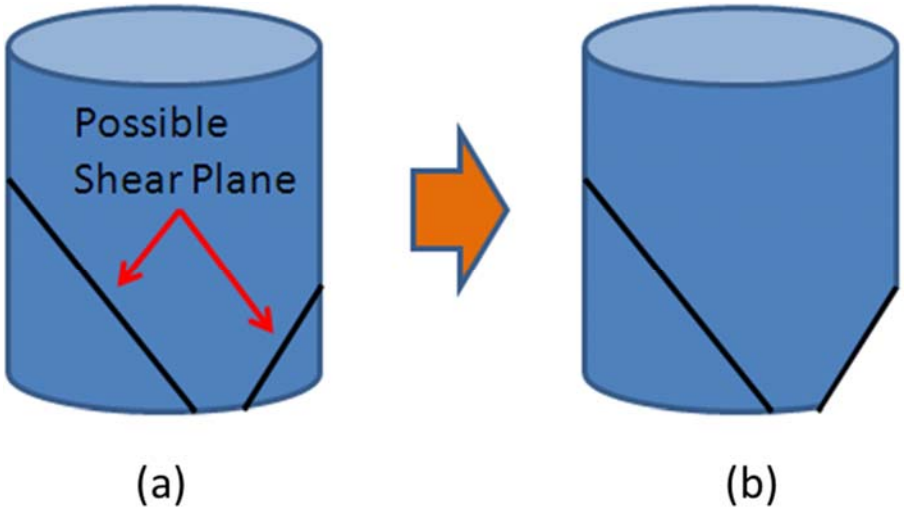

Figure 5-4 Possible failure mode of the large-diameter BMG under cyclic-compression stresses. (a) Some of the possible shear planes do not cut through the whole specimen, but start from the end of the specimen. (b) When a small piece of the sample was separated from the major part, the stress on the load-carrying cross-section of the sample is still less than the strength of the material. The situation became as if we were running a fatigue test using an irregularly-shaped specimen with higher stress levels.

5.3 Size-dependent fatigue behavior of BMGs

In Figure 4-6(b), we have shown that the fatigue life does not strongly correlate with the L/D ratio of the specimen. However, the sample volume also changed between the fatigue tests and become progressively smaller. Then the size effect on the fatigue behavior of BMGs should be examined. In the following section, we use statistical analyses to examine the effect of sample size on the fatigue life.

5.3.1 Model

A statistical model is developed to predict the fatigue life of the BMG based on the defect volume. We hypothesize that the fatigue life can be characterized by the Weibull theory. The Weibull theory assumes that the fatigue failure is determined by the presence of a critical defect, and such defects occur randomly within a material [81]. As a consequence, specimens with larger volumes will have higher probability of finding a critical defect, and, therefore, have statistically shorter fatigue lives when compared with specimens with smaller volumes [82, 83].

The two-parameter Weibull fatigue-life distribution has the following cumulative distribution function,

$$F(N \mid \alpha, \beta) = 1 - \exp\left[-V\left(\frac{N}{\alpha}\right)^{\beta} \right] \qquad (5\text{-}5)$$

where N denotes the cycles to failure, and V is the volume of the test specimen. This model has two parameters, α and β. α is the characteristic fatigue life of a unit volume, and β is

the Weibull fatigue modulus [81, 83]. The probability density function of the Weibull fatigue-life distribution is

$$f(N \mid \alpha, \beta) = V \frac{\beta}{\alpha}\left(\frac{N}{\alpha}\right)^{\beta-1} \exp\left[-V\left(\frac{N}{\alpha}\right)^{\beta}\right] \qquad (5\text{-}6)$$

Given the cycles to failure and the volumes of n test specimens, denoted by N_i and V_i, respectively, for $i = 1,\ldots, n$, the unknown parameters, α and β, can be estimated by the maximum likelihood method [84]. The maximum likelihood estimates of α and β maximizes the likelihood function given by

$$L(\alpha, \beta \mid N_1, \ldots, N_n, V_1, \ldots, V_n) = \prod_{i=1}^{n} V_i \frac{\beta}{\alpha}\left(\frac{N_i}{\alpha}\right)^{\beta-1} \exp\left[-V_i\left(\frac{N_i}{\alpha}\right)^{\beta}\right] \qquad (5\text{-}7)$$

The Weibull theory implies a volume-scaling relation between the fatigue life and the specimen volume. Assuming equal failure probabilities, the volume effect on the fatigue-life ratio for two specimens of volumes, V_A and V_B, is

$$\frac{N_A}{N_B} = \left(\frac{V_B}{V_A}\right)^{1/\beta} \qquad (5\text{-}8)$$

where N_A and N_B are the respective fatigue lives. This volume scaling relation suggests a possible way to assess the goodness-of-fit of the Weibull fatigue-life model, given a small amount failure data, by scaling all the observed fatigue lives to a reference volume. If the Weibull model is an appropriate model to describe the variability in the data and the volume effect, the scaled fatigue lives at the reference volume should follow a Weibull distribution.

5.3.2 Statistical analysis

Table 5-1 lists the volumes and the fatigue lives of ten specimens tested at a stress range of 720 MPa. The MATLAB Optimization Toolbox is used to maximize the likelihood function (4). The maximum likelihood estimates of the two-model parameters are $\beta = 1.453$ and $\alpha = 115.323$ million cycles.

Figure 5-5 shows the predicted median, 2.5 percentile, and 97.5 percentile lives. The 2.5 and 97.5 percentiles form a 95% predictive interval. This 95% predictive interval captures almost all the observations. Only one observation falls outside the predictive interval. To assess the goodness-of-fit of the Weibull fatigue-life model [81], all the observed cycles to failure are scaled to a reference volume of 700 mm^3 according to Equation (5). Table 5-2 lists the scaled fatigue lives. The Anderson-Darling goodness-of-fit test is applied here to test the hypotheses, H_0: the scaled fatigue lives follow the Weibull distribution vs. H_1: the scaled fatigue lives do not follow the Weibull distribution. The Anderson-Darling goodness-of-fit test yields a P-value of 0.202, and fails to reject H_0 at a significance level of 0.05 or 0.10.

We used the Weibull theory to describe the fatigue behavior of this material from the statistical point-of-view. According to the analytical results, the Weibull fatigue-life model seems to be an appropriate model to describe the variability in the observed fatigue data and the volume effect. The fatigue behavior of this material, therefore, may be explained by the Weibull theory. Although statistical analysis implies the possible size-dependent fatigue behavior (i.e., a smaller-volume sample tends to exhibit longer fatigue

life, Figure 5-5), more experimental and analytical work, however, need to be conducted to warrant the conclusions.

Table 5-1 Volumes and fatigue lives of ten experimental specimens.

Sample, i	Volume, V_i (mm^3)	Cycles to failure, N_i (million cycles)
1	282.7433	0.484017
2	282.7433	0.552864
3	707.4238	1.535442
4	704.0309	0.304354
5	704.0309	1.315717
6	139.1097	1.26922
7	268.0407	3.00371
8	495.3663	1.70379
9	240.8973	2.10075
10	419.0256	4.63925

Table 5-2 Scaled fatigue lives of the ten experimental specimens at the reference volume of 700 mm^3.

Sample, *i*	Scaled cycles to failure (million cycles)
1	0.259366
2	0.296259
3	1.546630
4	0.305559
5	1.320926
6	0.417446
7	1.551494
8	1.342976
9	1.008221
10	3.258950

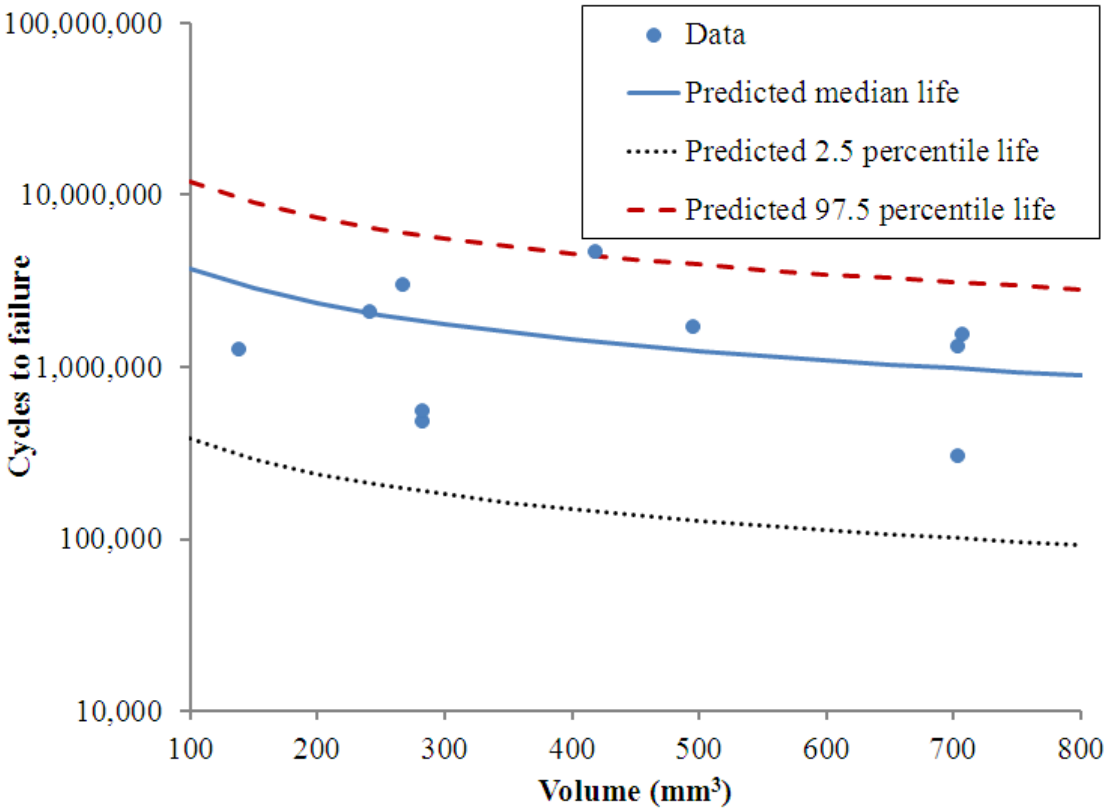

Figure 5-5 Predicted percentile lives by the Weibull fatigue-life model

5.3.3 Size effect

Recent studies of fatigue behavior of metallic-glass (MG) nanowires by computer molecular-dynamic simulations [85] showed that the MG will not fatigue. Shi et al. simulated the fatigue behavior of MG nanowires under strain-controlled compression-compression tests and found that "irreversible deformation occurs during all fatigue simulations. However, the MG nanowire does not suffer from structural damage, and no softening occurs during cyclic loading" [85]. Jang, Greer, and Gross [86, 87] reported a significant strength increase and highly-localized-to-homogeneous deformation mode change, when the size of the MG nanowire decreases to a nano-meter scale. The strength of the MG pillar starts increasing with decreasing the diameter at a micro-meter scale, and reaches its maximum value of 2.6 GPa at a diameter of 800 nm, compared to the yield strength of 1.7 GPa in the bulk (millimeter) scale. Below a diameter of 800 nm, the yield strength of the MG nano-pillar remains unchanged. However, there is a change of the deformation mechanism from a highly-localized shear-deformation mode to homogeneous viscous flow at a diameter of 100 nm. Jang, Maaβ, and Greer [88] further studied the fatigue behavior of MG micron-sized pillars and found that the fatigue limit is generally very close to the yield strength of BMGs, i.e., MGs will not fatigue at submicron scales. The experimental results are consistent with Shi et al's molecular-dynamic (MD) simulation [85]. These studies [85-87] showed that the size of the specimen does affect the fatigue behavior of amorphous alloys under compression-compression fatigue, i.e., smaller-size samples generally exhibit longer fatigue life. The results from the present study, Figure 5-5, do not show strong size-dependent behavior. The reason is likely due to

the fact that the sizes of the specimens used in the current study are on the millimeter scale. The size effect on the compression-compression fatigue could be pronounced at a micro-meter scale or below [27-29, 31].

Wang et al. [46] studied the effect of specimen size on the fatigue behavior of Zr-based BMGs under 4-point bending tests. They reported that the smaller-sized sample (2 mm x 2 mm x 25 mm) has shorter lifetime and lower fatigue-endurance limits than the large-sized sample (3 mm x 3 mm x 25 mm). Their results are different from what we observed in the present study. The inconsistency is most likely due to the different fatigue-fracture mechanisms between bending-fatigue and compression-compression fatigue tests. In bending fatigue, the small-sized BMG samples show the flexural and fracture failure, while the large-sized BMG samples only exhibit the fracture failure. Due to the improved bend ductility of the small-sized BMG sample, more multiple shear bands can form easily than the large-sized sample under cyclic loading. The cracks initiated from these shear bands. Thus, in the small-sized BMG sample during the bending test multiple shear bands act as weak spots initiating cracks, which shortens the fatigue life, relative to the large-sized sample [46]. On the other hand, in compression-compression-fatigue tests, crack initiation is associated with critical flaws (the weakest point) in the sample. The probability of having these flaws scales with the size (volume) of the sample. Therefore, smaller samples might have longer fatigue life under compression-compression fatigue.

5.4 Proposed fatigue-damage mechanisms

From several research papers [36, 37, 45, 89-91], one can categorize the fatigue failure of BMGs into three stages. The first is the crack-initiation stage, where a crack is initiated at the weakest point of the material, followed by the crack-propagation stage, where the crack advances slowly under the repeated loading and unloading fatigue process; and finally, the fast propagating stage, which causes the final failure of the material. The crack-initiation stage is the key to determine the fatigue life of such materials with very little or no plasticity. The fatigue-crack initiation sites in BMGs could be further divided into two groups. One is an intrinsic defect, such as free volumes and/or shear bands, which is associated with the nature of amorphous alloys, and the other is related to the extrinsic defects, such as inclusions, micro-voids, and nano-crystalline particles formed during the fabrication process, which, theoretically, can be eliminated by better fabrication techniques and/or procedures.

From this study, the fatigue-failure mechanism of the large (6-mm in-diameter) Zr-based BMGs under cyclic compression-compression stresses is suggested, and illustrated in Figure 5-6. The crack initiates at the weakest points (extrinsic defect sites as defined above) in the sample. The crack propagates slowly at the beginning and leaves the striation on the crack surface. The crack continues to grow until the sample cannot sustain the stress and then the fast-shearing process starts, which causes the catastrophic failure. During the crack-propagation process, the fatigue damage is localized. When one crack starts to grow, the rest of the sample still undergoes elastic deformation; the microstructure away from the crack region generally remains unchanged. Therefore, after cutting off the damaged part,

the remaining part performs like an as-cast material. The above mechanism implies that the fatigue limit of BMGs under cyclic compression-compression stresses can be greatly improved by reducing the number of extrinsic defects (crack-initiation sites) in the material.

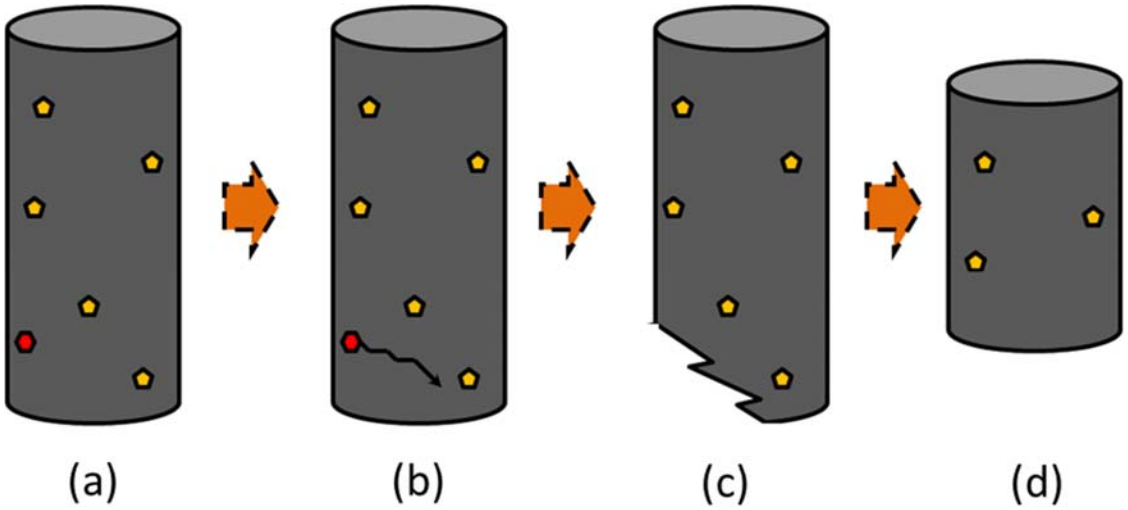

Figure 5-6 Proposed fatigue-failure mechanisms of the large (6-mm in-diameter) $(Zr_{55}Cu_{30}Ni_5Al_{10})_{98}Er_2$ BMGs. (a) The as-cast sample contains weak points (defect sites, such as microvoids or nanocrystalline particles formed during the fabrication process). (b) The crack initiates at the weakest point in the sample. The crack propagates slowly at the beginning and leaves the striation on the crack surface. (c) The crack continues to grow until the sample cannot sustain the stress and then starts the fast shearing of the sample (fast fracture). The fatigue damage is found to be localized. When one crack starts to grow, the rest of the sample still undergoes elastic deformation. The microstructure away from the crack region generally remains unchanged. (d) Therefore, after cutting off the damaged part, the remaining material performs like an as-cast material with less defects.

6 CHAPTER VI

CONCLUSIONS

(1) For the study of the effect of mechanical loading on the structure of BMG. The elastic formation of BMG in the macroscopic scale is not “elastic” in atomic scale. Through x-ray scattering and the anisotropic PDF analysis, it is shown that about a quarter of the volume of a metallic glass is occupied by anelastic sites, which are soft and bear no static shear load. Consequently the shear modulus of a metallic glass is lowered by a quarter compared to the instantaneous value. Just as other glasses, metallic glasses are fundamentally viscoelastic, and the volume fraction of the viscous sites is as much as a quarter, not of the order of 1% as in many theories. This point has to be fully taken into account in the application of metallic glasses, particularly as structural materials.

(2) For the study of the effect of cyclic loading on the structure of bulk metallic glasses. The effect of “pre-fatigue” on the fatigue behavior and atomic structure of Zr-based BMGs had been studied, aiming to provide better mechanistic understanding of the fatigue process in BMGs. The complete compression-compression fatigue study was conducted on the as-cast, 6-mm in-diameter, Zr-based BMGs. The fatigue-endurance limit and the fatigue ratio of this material were 500 MPa and 0.27, respectively. Fatigue experiments on the pre-fatigue-to-failure samples indicated that these leftovers generally had similar or longer cycles-to-failure than the as-cast samples. The PDF analysis of the as-cast and post-fatigue samples, using the high-energy

synchrotron X-ray scattering method, showed very small changes of local atomic structures. The results suggest that the fatigue life of the 6-mm in-diameter Zr-based BMG is dominated by the number of pre-existing crack-initiation sites in the sample. Once the crack initiates, the fatigue-induced damages are accumulated locally on these initiated sites, while the rest of the region deforms elastically. The statistical model predicts that the fatigue life of BMGs under compression-compression fatigue tests may be longer when the size of the sample decreases. The results from the present study imply that the fatigue failure of BMGs under compression-compression fatigue tests is a defect-controlled process.

(3) For the study of the fatigue damage in Ni-based superalloys. The two-dimensional lattice-strain map of a double-notched specimen at different stage of its expected fatigue life under various loading conditions were obtained by in-situ x-ray diffraction measurement. The as-prepared samples are free of residual stress prior to the fatigue tests, but substantial residual stress is developed around the notch tip after only 1 cycle. The cyclic loading creates a compressive-residual stress zone around the notch tip. The maximum compressive stress measured by the lattice strain can be as high as 830±50 MPa at the beginning of the fatigue life (1% expected life), and gradually decreases as the fatigue test continues to ~700±50 MPa for samples at 75% of expected life. The size of the compressive-stress zone increases with fatigue cycles, following a fast, slow, and fast pattern, similar to the da/dN vs. ΔK curve in fatigue-crack propagation experiments. Such compressive-stress zone increase rapidly in the first few cycles, and then transform into a slowly, and steady growing plateau, and

then speed up before failure. The fast-growing stage before failure is probably associated with the fatigue-induced failures. The size of the compressive-stress zone seems to be a good indication for the progressive fatigue damage during cyclic loading. However, the estimation of fatigue damage is qualitative, not quantitative. Finally, the strain variation possibly caused by the intergranuler stresses is large at the beginning of the fatigue life, but decrease with increasing fatigue cycles which indicates more and more grains were plastically deformed.

LIST OF REFERENCES

[1] Suresh S. Fatigue of materials. Cambridge England ; New York: Cambridge University Press, 1991.
[2] Forsyth PJE. The physical basis of metal fatigue. New York,: American Elsevier Pub. Co., 1969.
[3] Wood WA. Philosophical Magazine 1958;3:692.
[4] Zhou BZ, Chung YW. Jom-Journal of the Minerals Metals & Materials Society 1997;49:43.
[5] Sriram TS, Ke CM, Chung YW. Acta Metallurgica Et Materialia 1993;41:2515.
[6] Sriram TS, Fine ME, Chung YW. Acta Metallurgica Et Materialia 1992;40:2769.
[7] Venkataraman G, Chung YW, Nakasone Y, Mura T. Acta Metallurgica Et Materialia 1990;38:31.
[8] Harvey SE, Marsh PG, Gerberich WW. Acta Metallurgica Et Materialia 1994;42:3493.
[9] Inoue A, Shen BL, Chang CT. Intermetallics 2006;14:936.
[10] Zhang ZF, Eckert J, Schultz L. Acta Materialia 2003;51:1167.
[11] Schuh CA, Hufnagel TC, Ramamurty U. Acta Materialia 2007;55:4067.
[12] Zhang ZF, Eckert J, Schultz L. Metallurgical and Materials Transactions a-Physical Metallurgy and Materials Science 2004;35A:3489.
[13] Zhang ZF, He G, Eckert J, Schultz L. Physical Review Letters 2003;91.
[14] Zhang ZF, Eckert J, Schultz L. Journal of Materials Research 2003;18:456.
[15] Spaepen F. Scripta Materialia 2006;54:363.
[16] Spaepen F. Acta Metallurgica 1977;25:407.
[17] Lewandowski JJ, Greer AL. Nature Materials 2006;5:15.
[18] Argon AS. Acta Metallurgica 1979;27:47.
[19] Turnbull D, Cohen MH. Journal of Chemical Physics 1970;52:3038.
[20] Turnbull D, Cohen MH. Journal of Chemical Physics 1961;34:120.
[21] Cohen MH, Turnbull D. Journal of Chemical Physics 1959;31:1164.
[22] Egami T. Intermetallics 2006;14:882.
[23] Billinge SJL. Journal of Solid State Chemistry 2008;181:1695.
[24] Takeshi Egami, Billinge SJL. Underneath the Bragg Peaks: Strucutral Analysis of Complex Materials. Oxford: Pergamon Press, Elsevier, 2003.
[25] Poulsen HF, Wert JA, Neuefeind J, Honkimaki V, Daymond M. Nature Materials 2005;4:33.
[26] Hufnagel TC, Ott RT, Almer J. Physical Review B 2006;73.
[27] Hammersley AP, Svensson SO, Hanfland M, Fitch AN, Hausermann D. High Pressure Res. 1996;14:235.
[28] Stoica M, Das J, Bednarcik J, Wang G, Vaughan G, Wang WH, Eckert J. Jom 2010;62:76.
[29] Mattern N, Schoeps A, Kuehn U, Acker J, Khvostikova O, Eckert J. J. Non-Cryst. Solids 2008;354:1054.
[30] Wang XD, Bednarcik J, Saksl K, Franz H, Cao QP, Jiang JZ. Applied Physics Letters 2007;91.
[31] Gilbert CJ, Lippmann JM, Ritchie RO. Scripta Materialia 1998;38:537.

[32] Wang GY, Liaw PK, Peter WH, Yang B, Freels M, Yokoyama Y, Benson ML, Green BA, Saleh TA, McDaniels RL, Steward RV, Buchanan RA, Liu CT, Brooks CR. Intermetallics 2004;12:1219.
[33] Wang GY, Liaw PK, Peker A, Freels M, Peter WH, Buchanan RA, Brooks CR. Intermetallics 2006;14:1091.
[34] Harlow DG, Liaw PK, Peter WH, Wang GY, Buchanan RA. Acta Materialia 2008;56:3306.
[35] Tatschl A, Gilbert CJ, Schroeder V, Pippan R, Ritchie RO. Journal of Materials Research 2000;15:898.
[36] Peter WH, Liaw PK, Buchanan RA, Liu CT, Brooks CR, Horton JA, Carmichael CA, Wright JL. Intermetallics 2002;10:1125.
[37] Peter WH, Buchanan RA, Liu CT, Liaw PK. J. Non-Cryst. Solids 2003;317:187.
[38] Wang GY, Liaw PK, Peker A, Yang B, Benson ML, Yuan W, Peter WH, Huang L, Freels A, Buchanan RA, Liu CT, Brooks CR. Intermetallics 2005;13:429.
[39] Menzel BC, Dauskardt RH. Acta Materialia 2006;54:935.
[40] Gilbert CJ, Schroeder V, Ritchie RO. Metallurgical and Materials Transactions a-Physical Metallurgy and Materials Science 1999;30:1739.
[41] Yokoyama Y, Liaw PK, Nishijima M, Hiraga K, Buchanan RA, Inoue A. Materials Transactions 2006;47:1286.
[42] Nakai Y, Hosomi S. Materials Transactions 2007;48:1770.
[43] Nakai Y, Sakai K, Nakagawa K. Advanced Engineering Materials 2008;10:1026.
[44] Launey ME, Busch R, Kruzic JJ. Scripta Materialia 2006;54:483.
[45] Wang GY, Liaw PK, Peter WH, Yang B, Yokoyama Y, Benson ML, Green BA, Kirkham MJ, White SA, Saleh TA, McDaniels RL, Steward RV, Buchanan RA, Liu CT, Brooks CR. Intermetallics 2004;12:885.
[46] Wang GY, Liaw PK, Yokoyama Y, Inoue A. J. Appl. Phys. 2011;110:113507.
[47] Wang GY, Liaw PK, Morrison ML. Intermetallics 2009;17:579.
[48] Flores KM, Suh D, Howell R, Asoka-Kumar P, Sterne PA, Dauskardt RH. Materials Transactions 2001;42:619.
[49] Hess PA, Menzel BC, Dauskardt RH. Scripta Materialia 2006;54:355.
[50] Qiao DC, Wang GY, Jiang WH, Yokoyama Y, Liaw PK, Choo H. Materials Transactions 2007;48:1828.
[51] Wright WJ, Hufnagel TC, Nix WD. Journal of Applied Physics 2003;93:1432.
[52] McDowell DL. International Journal of Damage Mechanics 1999;8:376.
[53] McDowell DL. International Journal of Fracture 1996;80:103.
[54] Miller KJ. Materials Science and Technology 1993;9:453.
[55] Dunne FPE, Wilkinson AJ, Allen R. International Journal of Plasticity 2007;23:273.
[56] Manonukul A, Dunne FPE. Proceedings of the Royal Society of London Series a-Mathematical Physical and Engineering Sciences 2004;460:1881.
[57] Bairstow L. Philosophical Transactions of the Royal Society of London Series a-Containing Papers of a Mathematical or Physical Character 1911;210:35.
[58] Miller KJ. Proceedings of the Institution of Mechanical Engineers Part C-Journal of Mechanical Engineering Science 1991;205:291.

[59] Gough HJ, Sopwith DG. Journal of the Institute of Metals 1932;49:93.
[60] Thompson N, Wadsworth N, Louat N. Philosophical Magazine 1956;1:113.
[61] Hyzak JM, Bernstein IM. Metallurgical Transactions a-Physical Metallurgy and Materials Science 1982;13:33.
[62] Lin XH, Johnson WL, Rhim WK. Materials Transactions Jim 1997;38:473.
[63] Wall JJ, Fan C, Liaw PK, Liu CT, Choo H. Review of Scientific Instruments 2006;77:4.
[64] Jiang WH, Fan GJ, Choo H, Liaw PK. Materials Letters 2006;60:3537.
[65] Patterson AL. Physical Review 1934;46:0372.
[66] Wagner CNJ. J. Non-Cryst. Solids 1978;31:1.
[67] Suzuki Y, Egami T. J. Non-Cryst. Solids 1985;75:361.
[68] Suzuki Y, Haimovich J, Egami T. Physical Review B 1987;35:2162.
[69] Zhang Z, Keppens V, Liaw PK, Yokoyama Y, Inoue A. Journal of Materials Research 2007;22:364.
[70] Dmowski W, Iwashita T, Chuang CP, Almer J, Egami T. Physical Review Letters 2010;105.
[71] DeWit R. Journal of Applied Crystallography 1997;30:510.
[72] Matthies S, Priesmeyer HG, Daymond MR. Journal of Applied Crystallography 2001;34:585.
[73] Howard CJ, Kisi EH. Journal of Applied Crystallography 1999;32:624.
[74] Pollock TM, Argon AS. Acta Metallurgica Et Materialia 1992;40:1.
[75] Ichitsubo T, Koumoto D, Hirao M, Tanaka K, Osawa M, Yokokawa T, Harada H. Acta Materialia 2003;51:4863.
[76] Hutchings MT. Introduction to the characterization of residual stress by neutron diffraction. Boca Raton, FL: Taylor & Francis, 2005.
[77] Egami T, Poon SJ, Zhang Z, Keppens V. Physical Review B 2007;76.
[78] Weaire D, Ashby MF, Logan J, Weins MJ. Acta Metallurgica 1971;19:779.
[79] Freels M, Wang GY, Zhang W, Liaw PK, Inoue A. Intermetallics 2011;19:1174.
[80] Wang GY, Demetriou MD, Schramm JP, Liaw PK, Johnson WL. Journal of Applied Physics 2010;108.
[81] Weibull W. Journal of Applied Mechanics-Transactions of the Asme 1951;18:293.
[82] Wisnom MR. Composites Science and Technology 1999;59:1937.
[83] Bigley RF, Gibeling JC, Stover SM, Hazelwood SJ, Fyhrie DP, Martin RB. Journal of Biomechanics 2007;40:3548.
[84] Dempster AP, Laird NM, Rubin DB. Journal of the Royal Statistical Society Series B-Methodological 1977;39:1.
[85] Shi YF, Louca D, Wang GY, Liaw PK. Journal of Applied Physics 2011;110.
[86] Jang D, Greer JR. Nature Materials 2010;9:215.
[87] Jang D, Gross CT, Greer JR. International Journal of Plasticity 2011;27:858.
[88] Greer JR. Unpublised results 2011.
[89] Schroeder V, Gilbert CJ, Ritchie RO. Materials Science and Engineering a-Structural Materials Properties Microstructure and Processing 2001;317:145.
[90] Schroeder V, Gilbert CJ, Ritchie RO. Scripta Materialia 1999;40:1057.
[91] Gilbert CJ, Ritchie RO, Johnson WL. Applied Physics Letters 1997;71:476.

Vita

Chih-Pin, Andrew, Chuang was born in Ping-Tung, Taiwan. He obtained his Bachelor of Science degree from the Department of Engineering and System Science at National Tsing-Hua University in June 1998, and subsequently received the Master of Science degree from the same institute in July 2000. He joined the Army in August 2000, and was proudly serving his country for two years. He was honorably discharged from the Army Airborne Special Operations Forces in 2002. After working for few years in industry, he attended the doctoral program in Materials Science and Engineering at the University of Tennessee in the summer of 2008. He received the Doctor of Philosophy degree in December 2013